Response from authors

Re: Review of WRF-GC (v2.0): online two-way coupling of WRF (v3.9.1.1) and GEOS-Chem (v12.7.2)

for modeling regional atmospheric chemistry-meteorology interactions

May 10, 2021

We thank the three Reviewers for their helpful comments. In response, we made the following major changes: (1) expanded the analyses on the impacts of ARI and ACI on regional meteorology and air quality; (2) added sensitivity simulations to inspect the impacts of ARI and ACI on the simulated Chinese surface $PM_{2.5}$ concentrations in winter; and (3) compared the computational performance of one-way and two-way coupled simulations using WRF-GC v2.0. We also revised the writing to improve clarity throughout and to keep the manuscript within reasonable length.

We respond to each specific comment in detail below. The referee comments are shown in red italics. Our replies are shown in black and modified text is shown in blue. The annotated page and line numbers refer to the revised copy of the manuscript.

1 Reviewer #1

General Comments

The authors developed and presented the WRF-GC model v2.0, an online two-way coupling of the Weather Research and Forecasting (WRF) meteorological model (v3.9.1.1) and the GEOS-Chem chemical model (v12.7.2). The main feature of the WRF-GC v2.0 includes aerosol-radiation Interactions (ARI) and aerosol-cloud interactions (ACI). The authors evaluated the sensitivity simulations with different combinations of ARI and ACI over

Thanks for your suggestions. We added three new sensitivity experiments for January 2015 with different combinations of chemical feedbacks (Cases ARIw, ACIw, NO_ACRw). We compared and discussed the impacts of ARI and ACI to simulated regional meteorology and surface air quality in Section 4 and Section 5. We also added Tables 5 and 6 to summarize the performance of the different sensitivity experiments.

Table 4: Configurations of WRF-GC v2.0 experiments in this study

Experiment	Case ACRs (Case Summer)	Case ARIs	Case ACIs	Case NO_ACRs
Simulation time (UTC)	2016-06-27 00Z to 2016-07-31 00Z			
Microphysics	Morrison two-moment (Morrison et al., 2009)			
Shortwave radiation	RRTMG (Iacono et al., 2008)			
Longwave radiation	RRTMG (Iacono et al., 2008)			
Planetary boundary Layer	MYNN2 (Nakanishi and Niino, 2006)			
Land surface	Noah (Chen and Dudhia, 2001a,b)			
Surface layer	MM5 Monin-Obukhov (Jimenez et al., 2012)			
Cumulus parameterization	New Tiedtke (Tiedtke, 1989; Zhang et al., 2011; Zhang and Wang, 2017)			
Aerosol-radiation interaction	On	On	Off	Off
Aerosol-cloud interaction	On	Off	On	Off
Experiment	Case ACRw (Case Winter)	Case ARIw	Case ACIw	Case NO_ACRw
Simulation time (UTC)	2015-01-04 00Z to 2015-01-29 00Z			
Microphysics	Morrison two-moment (Morrison et al., 2009)			
Shortwave radiation	RRTMG (Iacono et al., 2008)			
Longwave radiation	RRTMG (Iacono et al., 2008)			
Planetary boundary Layer	YSU (Hong et al., 2006)			
Land surface	Noah (Chen and Dudhia, 2001a,b)			
Surface layer	MM5 Monin-Obukhov (Jimenez et al., 2012)			
Cumulus parameterization	New Tiedtke (Tiedtke, 1989; Zhang et al., 2011; Zhang and Wang, 2017)			
Aerosol-radiation interaction	On	On	Off	Off
Aerosol-cloud interaction	On	Off	On	Off

P13-14, L368-370, L378-383, Section 4.1

We next evaluate WRF-GC's performance in simulating regional meteorology and surface pollutant concentrations. We conduct two control simulations with full aerosol-cloud-radiation interactions using WRF-GC v2.0, one during January 2015 (Case ACRw) and one during July 2016 (Case ACRs). Table 4 summarizes the setup of our simulations.

We further conduct sensitivity simulations over China for January 2015 and July 2016 with different combinations of ARI and ACI to investigate the impacts of chemical feedbacks on simulated meteorology and air quality (Table 4). The setup of these sensitivity simulations are identical to the control cases, except ARI and ACI are configured differently in each sensitivity simulation (Table 4). In Cases NO_ACRs and NO_ACRw, both ARI and ACI are turned off, i.e., one-way WRF-GC simulations with no chemical feedbacks to meteorology. The Cases ARIs/ARIw and the Cases ACIs/ACIw simulations include either ARI or ACI, respectively.

P16, L473-476, Section 4.4

Figures 6a and 6b show the observed and simulated (Case ACRw) average LCODs during January 8 to 28, 2015. The model reproduces the spatial distribution of LCODs observed by VIIRS over China, including in particular the high LCODs over Southern China. However, the simulated LCOD is considerably lower than the VIIRS LCOD observations elsewhere in the domain.

P17, L486-496, Section 4.5

Figures 9a and 9b compare the mean SWDOWN observed by CERES and that simulated by WRF-GC (Case ACRw) during January 8 to 28, 2015. The spatial distribution of the simulated wintertime SWDOWN also agrees well with the satellite observations, with a spatial correlation coefficient of 0.93 over the domain. The domain-average observed and simulated SWDOWN are 111 ± 45 W m^{-2} and 140 ± 55 W m^{-2}, respectively (model NMB = 25.9%). The overestimation of wintertime SWDOWN is over the Sichuan Basin, the Tibetan Plateau and the
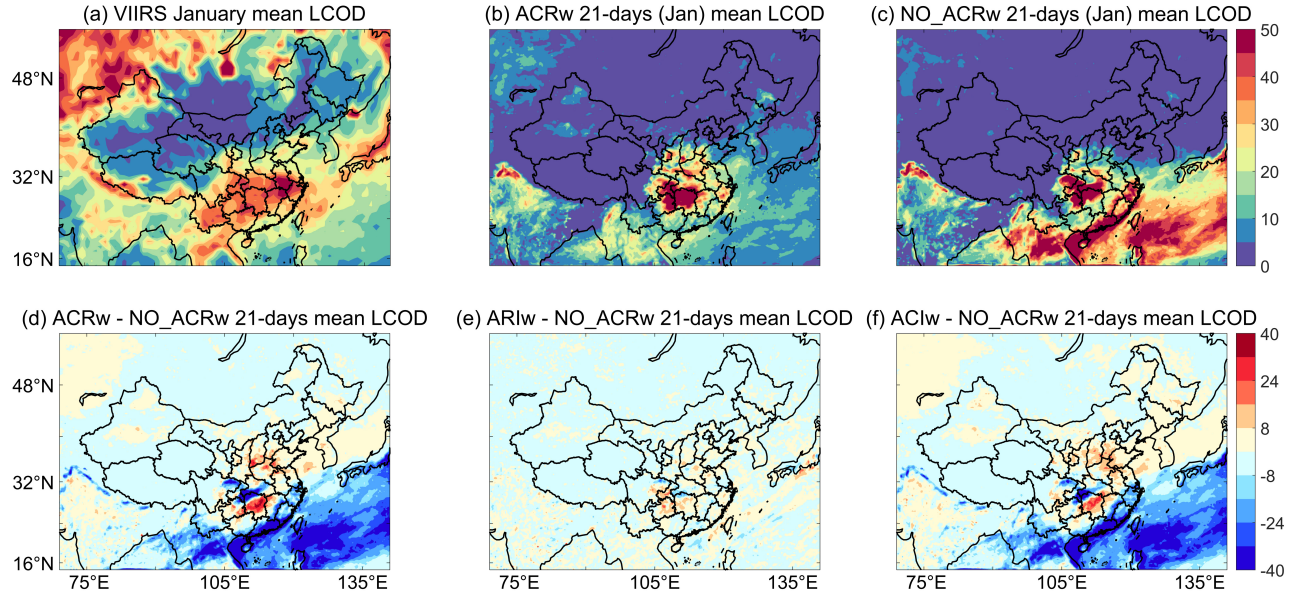
Figure 6: Mean LCOD from (a) VIIRS observations (monthly mean in during January 2015), (b) the Case ACRw simulation, and (c) the Case NO_ACRs simulation during January 8 to 28, 2015. Also shown are the differences in simulated LCOD between (d) Case ACRw and Case NO_ACRw, (e) Case ARIw and Case NO_ACRw, and (f) Case ACIw and Case NO_ACRw during January 8 to 28, 2015.
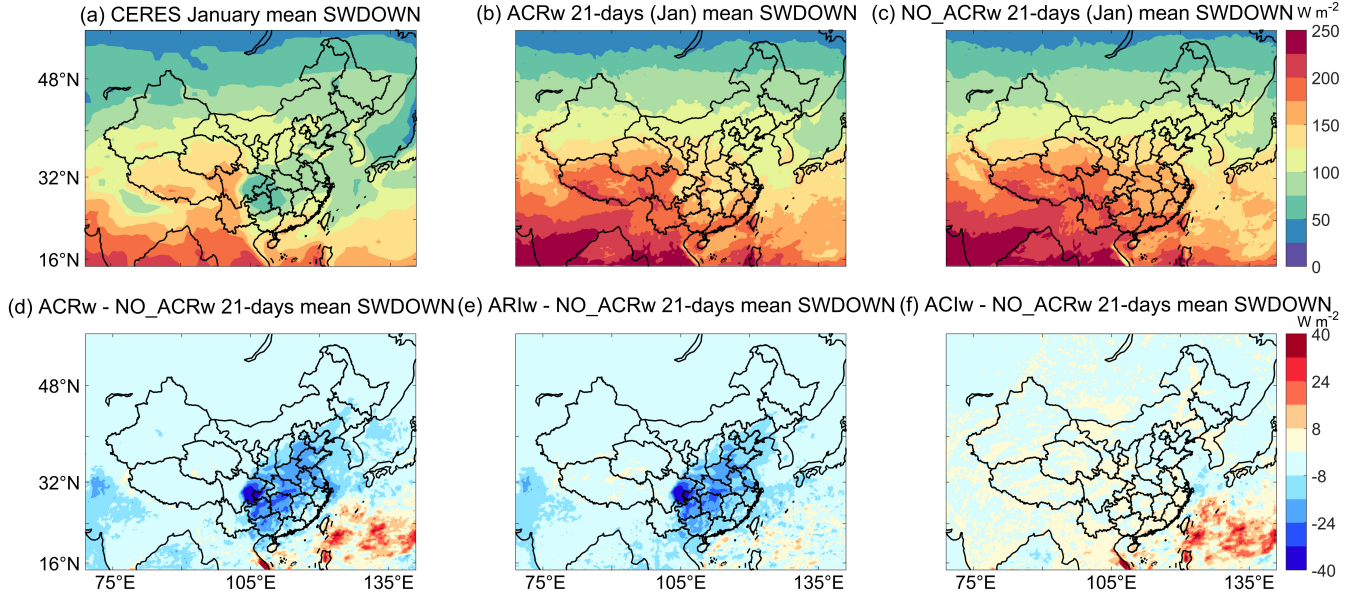
4

Figure 9: Mean surface downward shortwave radiation (SWDOWN) from (a) CERES observations (monthly mean in January), (b) the Case ACRw simulation, and (c) the Case NO_ACRw simulation during January 8 to 28, 2015. Also shown are the differences in simulated mean SWDOWN between (d) Case ACRw and Case NO_ACRw, (e) Case ARIw and Case NO_ACRw, and (f) Case ACIw and Case NO_ACRw during January 8 to 28, 2015.

P17, L497-502, Section 4.5

Figure 10a and Figure 11a show the good agreement between the simulated and observed surface air temperature over China during July 2016 (Case ACRs) and during January 8 to 28, 2015 (Case ACRw), respectively. The spatial correlation coefficients between the observed and simulated surface air temperature are 0.92 (Case ACRs) and 0.93 (Case ACRw), respectively. During July 2016, the simulated and observed surface air temperature averaged over all sites are 23.7 ± 5.9 °C and 24.6 ± 5.0 °C, respectively (NMB of -3.7%). During January 8 to 28, 2015, the simulated surface air temperature averaged over all sites is 7.2 ± 6.7 °C, with a model NMB of -13.3 % relative to the observations.
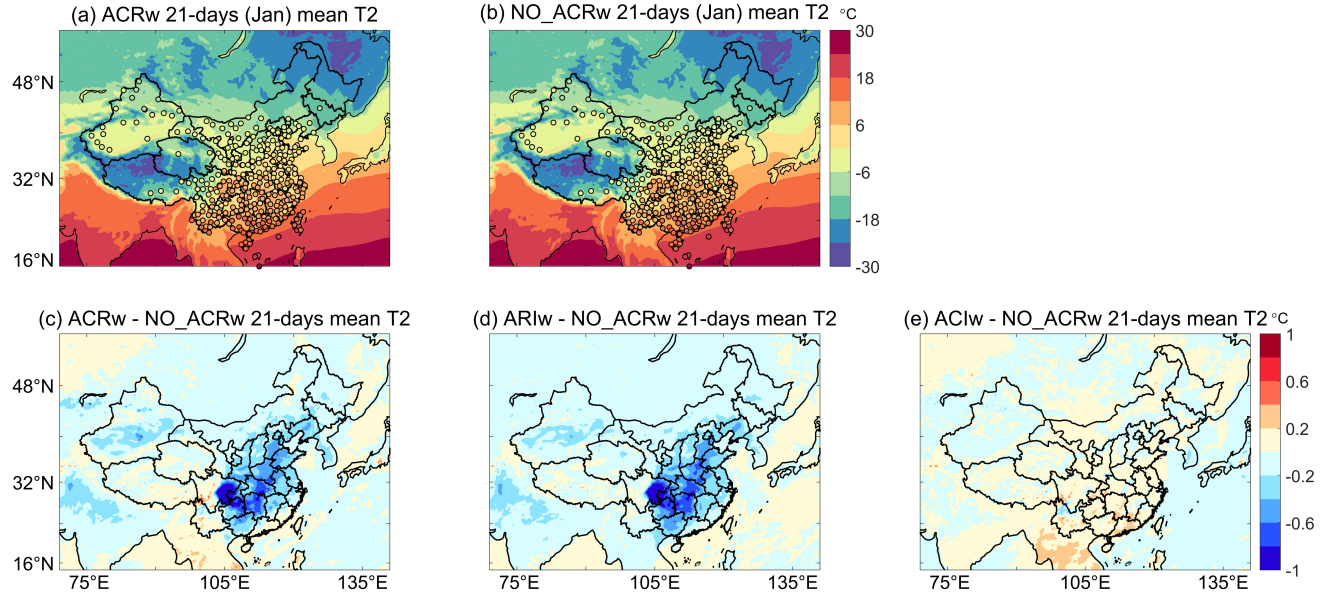
Figure 11: Comparison of the observed (filled symbols) and simulated (filled contours) mean surface air temperature from (a) Case ACRw and (b) Case NO_ACRw during January 8 to 28, 2015. Also shown are the differences in simulated mean surface air temperature between (c) Case ACRw and Case NO_ACRw, (d) Case ARIw and Case NO_ACRw, and (e) Case ACIw and Case NO_ACRw during January 8 to 28, 2015.

P18, L536-537, Section 5.1

Figures 5 and 6 show the impacts of ARI and ACI on the simulated LCOD in July 2016 and in January 2015, respectively.

P18, L539-544, Section 5.1

In particular, we find that the inclusion of ACI greatly reduces the simulated LCOD in both seasons; the inclusion of ACI corrects the high-biased LCODs simulated by Cases NO_ACRs and NO_ACRw, particularly over Central and Southern China, around Japan and Korea, and along the southern slopes of the Himalayas. In Cases ACRs and ACRw, the simulated monthly mean CCN concentrations (at 0.1 % supersaturation) averaged from the cloud bottom to cloud top are 150 cm^{-3} and 58 cm^{-3}, respectively. However, when ACI is turned off, WRF-GC uses a constant, high CCN activation rate (250 cm^{-3} per time step), leading to overestimation of cloud droplet numbers (effectively around 250 cm^{-3}) and thus LCOD.

P18, L545, Section 5.1

Figure 8 and 9 show the impacts of ARI and ACI on the simulated SWDOWN in July 2016 and January 2015, respectively.

P18, L552-561, Section 5.1

In January, the inclusion of ARI reduces the simulated SWDOWN over Eastern China by 8 to 40 W m^{-2}, while the inclusion of ACI does not significantly affect the simulated SWDOWN.

Figures 10 and 11 compare the simulated mean surface air temperature from the sensitivity experiments during July 2016 and January 2015, respectively.

In January, the impacts of ARI on surface air temperature are much stronger than the impacts of ACI. Upon closer inspection, we find that the simulated responses of surface air temperature to ARI and ACI are spatially similar to the simulated responses of SWDOWN, but with some exception.

P19, L574-579, Section 5.2

Figures 14d,e,f shows the combined and individual impacts of ARI and ACI on the simulated surface PM$_{2.5}$ concentrations during January 8 to 28, 2015, relative to the simulation when both ARI and ACI are turned off. Table 6 summarizes the assessment of the simulated surface PM$_{2.5}$ concentrations against surface measurements. The inclusion of ARI significantly increases the simulated surface PM$_{2.5}$ concentrations by 6 μg m^{-3} to 15 μg m^{-3} over parts of Northern and Southern China, and the Sichuan Basin, thereby improving the agreement with surface observations (Table 6, model versus observation slope = 0.97 in Case ACRw and 0.9 in Case NO_ACRw, respectively).

Table 6: Comparison between the PM$_{2.5}$ and afternoon ozone concentrations simulated by sensitivity experiments against the surface observations during July 2016 and January 2015

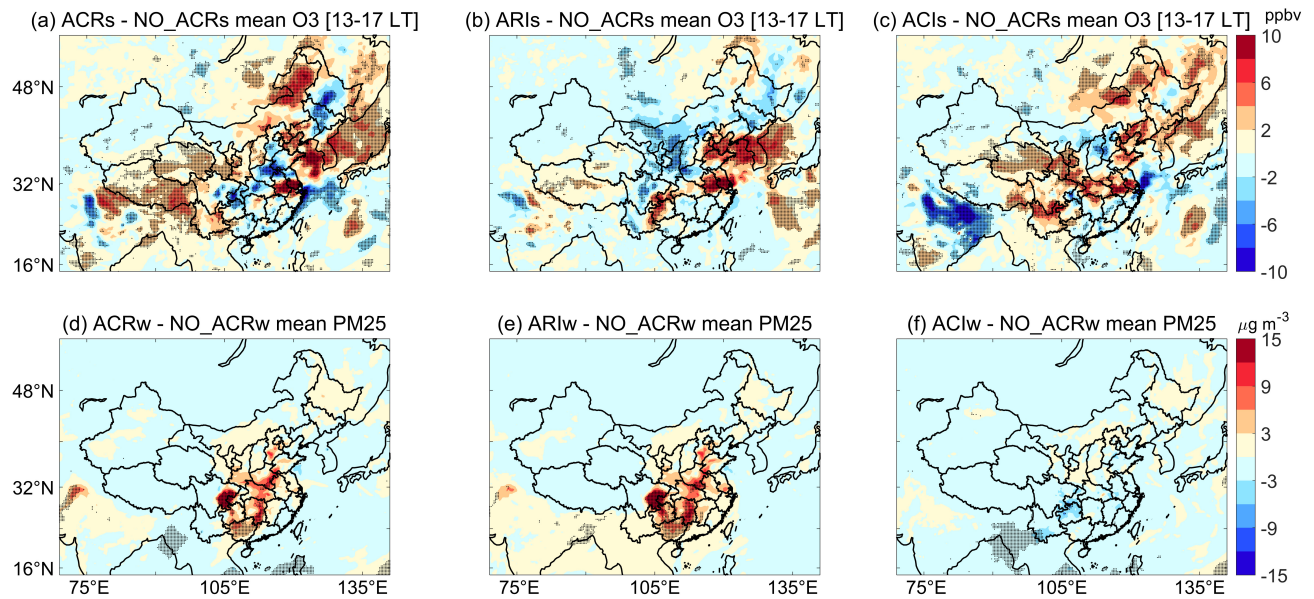| PM$_{2.5}$: 388 sites over Eastern China [μg m^{-2}]			
	Mean ± stdev	R	Slope
Case ACRw	80.8 ± 32.6	0.77	0.97
Case ARIw	81.6 ± 32.6	0.77	0.97
Case ACIw	77.9 ± 30.4	0.78	0.9
Case NO_ACRw	78.8 ± 30.4	0.78	0.9
Afternoon ozone: 426 sites over Eastern China [ppbv]			
	Mean ± stdev	R	Slope
Case ACRs	64.2 ± 16.9	0.56	1.33
Case ARIs	64.7 ± 17.1	0.57	1.34
Case ACIs	65.0 ± 17.6	0.54	1.38
Case NO_ACRs	63.6 ± 17.6	0.52	1.38

Figure 14: Differences in simulated monthly mean afternoon (13:00 to 17:00 local sun time) surface ozone concentrations during July 2016 (a) between Case ACRs and Case NO_ACRs, (b) between Case ARIs and Case NO_ACRs, and (c) between Case ACIs and Case NO_ACRs. Differences of simulated mean $PM_{2.5}$ concentrations during January 8 to 28, 2015 (d) between Case ACRw and Case NO_ACRw, (e) between Case ARIw and Case NO_ACRw , and (f) between Case ACIw and Case NO_ACRw. Stippled grids represent significant differences (two-tail t-test at 5% significance level).

R1.2 Chapter 4.3, 4.4, 4.5, 4.6 (Validation of the simulated AOD, LCOD, surface downward shortwave radiation, and air temperature). Among the sensitivity simulations with different combinations of ARI and ACI, the Case ACR (ARI and ACI are both turned on) had the best consistency with the best observed values? Author should show the model performance evaluation (MPE) in depth prior to the sensitivity experiments. I believe model sensitivity itself dose not tell many things.

Thanks you for pointing out this lack of clarity. We added Table 5 to validate the control experiments (Cases ACRs and ACRw) against observations, as well as to compare the performance of each sensitivity experiments in simulating regional meteorology. We also revised the text to describe the validation of the control experiments against observations. For all regional meteorological or air quality parameters examined in this paper, the simulations with

9

both ARI and ACI consistently showed best agreement with the observations.

P18, L534-544, Section 5.1

Table 5 summarized the comparison between the monthly mean meteorological variables simulated by the sensitivity experiments and the observations.

In both seasons, the simulated LCODs over Eastern China agree best with the VIIRS observations when ARI and ACI are both turned on (Cases ACRs and ACRw), compared to the sensitivity simulations when ARI or ACI, or both, are turned off (Table 5).

In Cases ACRs and ACRw, the simulated monthly mean CCN concentrations (at 0.1 % supersaturation) averaged from the cloud bottom to cloud top are $150\,\mathrm{cm}^{-3}$ and $58\,\mathrm{cm}^{-3}$, respectively. However, when ACI is turned off, WRF-GC uses a constant, high CCN activation rate ($250\,\mathrm{cm}^{-3}$ per time step), leading to overestimation of cloud droplet numbers (effectively around $250\,\mathrm{cm}^{-3}$) and thus LCOD.

P18, L546-547, Section 5.1

Again, the simulated SWDOWN over China are most consistent with EPIC-derived and CERES observations, in terms of magnitudes and spatial correlations, when both ARI and ACI are turned on (Table 5).

P19, L552-554, Section 5.1

In January, the inclusion of ARI reduces the simulated SWDOWN over Eastern China by 8 to $40\,\mathrm{W\,m}^{-2}$, while the inclusion of ACI does not significantly affect the simulated SWDOWN.

P19, L556-558, Section 5.1

Again, the inclusion of both ARI and ACI leads to best agreement between the observed and simulated surface air temperature in both seasons (Table 5).

Table 5: Comparison of the simulated liquid cloud optical depth (LCOD), surface downward shortwave radiation (SWDOWN), and surface temperature (T2) from sensitivity experiments against satellite and surface observations during July 2016 and January 2015

	Case ACRs	Case ARIs	Case ACIs	Case NO_ACRs	Case ACRw	Case ARIw	Case ACIw	Case NO_ACRw
LCOD over Eastern China (eastward of 100 °E) against VIIRS observations								
Mean ± stdev	13.0 ± 8.6	22.1 ± 13.0	12.5 ± 8.1	21.8 ± 12.4	9.8 ± 10.4	17.3 ± 18.7	9.6 ± 10.4	17.1 ± 18.6
R	0.64	0.65	0.60	0.62	0.48	0.34	0.46	0.33
RMSE	8.4	10.9	8.7	10.7	15.2	18.4	15.4	18.5
SWDOWN [W m^{-2}] over China against EPIC-derived observations (July) and CERES observations (January)								
Mean ± stdev	281 ± 48	274 ± 49	287 ± 49	278 ± 51	140 ± 55	139 ± 55	144 ± 57	143 ± 56
R	0.73	0.65	0.65	0.57	0.93	0.92	0.91	0.9
RMSE	33.7	40.4	37.5	43.5	36.3	35.4	41.2	40.4
T2 [°C] over China against surface measurements (215 sites in July, 150 sites in January)								
Mean ± stdev	23.7 ± 5.9	23.7 ± 6.1	23.8 ± 6.0	23.8 ± 6.0	7.2 ± 6.7	7.1 ± 6.7	7.4 ± 6.7	7.3 ± 6.6
R	0.92	0.93	0.92	0.92	0.93	0.93	0.93	0.93
RMSE	2.52	2.57	2.56	2.57	2.7	2.8	2.6	2.7

R1.3 Overall, this manuscript is missing interpretations of key physical/chemical processes related to ARI and ACI in the WRF-GC model v2.0. In chapter 5, there is no explanation on the impacts of ARI and ACI on the meteorological factors and air pollutants.

Thank you for pointing out this omission. We added diagnostic figures of the impacts of ARI and ACI, either individually or combined, on surface downward shortwave radiation (Figures 8 and 9), surface air temperature (Figures 10 and 11), wintertime boundary layer height (Figure 12), wintertime surface PM$_{2.5}$ and summertime afternoon surface ozone (Figure 14), and the summertime net chemical tendency of boundary-layer ozone (Figure 15). We also significantly expanded the discussion (Section 5) of the mechanisms by which ARI and ACI modulated air temperature and surface radiation, and subsequently affected the boundary layer height in winter and the ozone chemical production in summer.

P19-20, L580-587, Section 5.2

Figures 12c,d,e show the combined and individual impacts of ARI and ACI on the simulated PBLH during January 8 to 28, 2015, relative to the simulation when both ARI and ACI are turned off. We find that the simulated response of surface $PM_{2.5}$ to ARI is spatially consistent with the simulated responses of SWDOWN, surface air temperature, and PBLH to ARI. Over the Sichuan Basin and parts of Northern and Central China, the strong aerosol extinction decrease the SWDOWN and surface air temperature, resulting in lower PBLH and a possibly more stable conditions within the PBL. The shallower and more stable PBL suppresses the dispersion of air pollutants, thus increasing surface $PM_{2.5}$ concentrations. These findings are consistent with previous studies (Wang et al., 2014; Li et al., 2017; Zhang et al., 2018), although other feedback mechanisms may also play a role.

P20, L589-596, Section 5.3

Figures 14a,b,c show the combined and individual effects of the ARI and ACI on the simulated mean surface afternoon ozone concentrations in July 2016, relative to the Case NO_ACRs experiment. Overall, the inclusion of ARI and ACI in WRF-GC slightly reduces the model's positive bias in simulated surface ozone concentration (Table 6; model versus observation slope is 1.33 in Case ACRs and 1.38 in Case NO_ACRs, respectively). By including both ARI and ACI, the simulated July afternoon surface ozone concentration decrease by 2 to 10 ppbv over Henan Province, the Sichuan Basin, and parts of Northeastern China. Over the YRD area and Eastern Inner Mongolia, turning on ARI and ACI leads to increased afternoon surface ozone concentrations by up to 10 ppbv. These results are due to the spatially-varied responses of surface ozone to ARI and ACI, respectively (Figure 14).

P20, L597-612, Section 5.3

We further diagnose the net chemical mass tendency of the simulated ozone in the boundary layer over China during July 2016, to elucidate the mechanisms by which ARI and ACI affect boundary-layer ozone. The net chemical mass tendency (unit: $kg\ s^{-1}$) is the net rate of change of boundary-layer ozone mass due to chemical production and loss processes over each model grid, and its responses to ARI and ACI are shown in Figure 15. We find that the spatial responses of the net chemical mass tendency of ozone to ARI and ACI are very similar to the simulated responses of surface afternoon ozone, SWDOWN, and surface air temperature to these chemical feedbacks (Figures

8, 10, and 14). This indicates that ARI and ACI affect surface ozone mainly by modulating SWDOWN and surface air temperature, which in turn affect the emissions of biogenic isoprene and the subsequent chemical production of ozone in the boundary layer. For example, ARI lead to increased surface air temperature over the YRD area, while both ARI and ACI lead to increased SWDOWN over that area. These meteorological responses lead to enhanced local biogenic isoprene emissions and increased surface ozone. Over the Beijing-Tianjin-Hebei (BTH) area of China, where summertime ozone pollution is most severe (Lu et al., 2018), the effects of ARI and ACI are complex. ARI and ACI both reduce the local SWDOWN (Figures 8e,f), while ARI increases surface air temperature over southern BTH and ACI suppresses surface air temperature over the entire BTH (Figures 10d,e). The combined effect of chemical feedbacks is to increase surface ozone over northern BTH, while decreasing surface ozone over southern BTH. ARI and ACI may also modulate other meteorological variable to affect surface ozone, and such possibilities warrants further investigation.
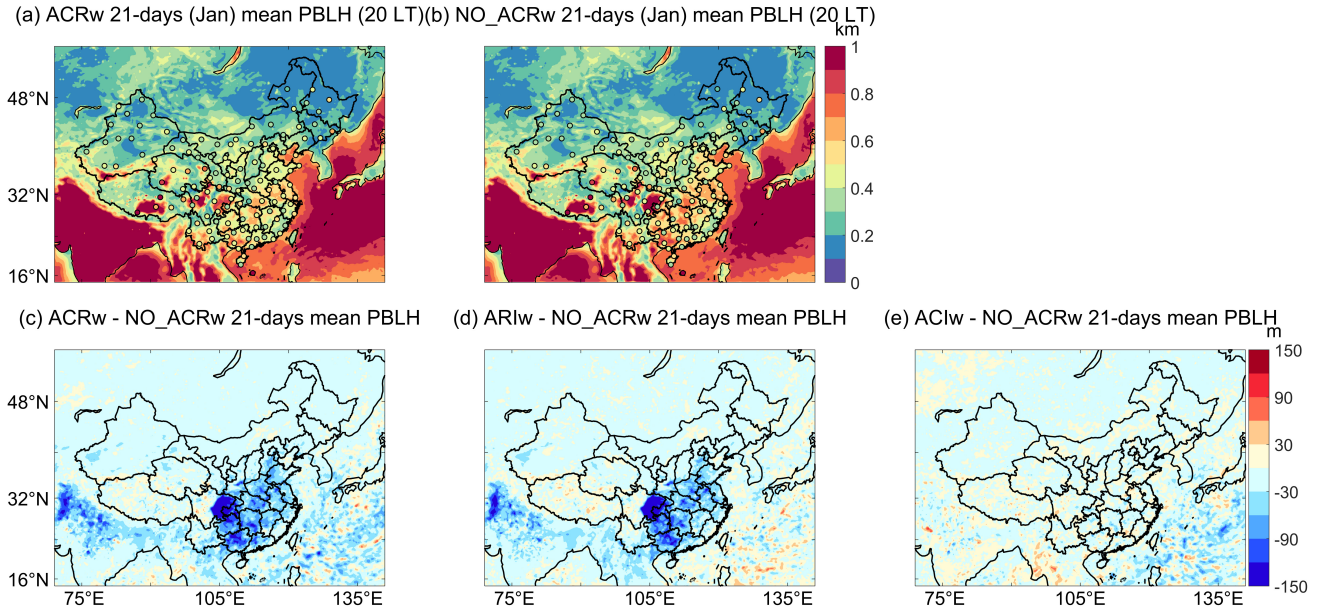
Figure 12: Comparison of the observed (filled symbols) and simulated (filled contours) mean planetary boundary layer heights (PBLH) at 20:00 local time (12:00 UTC) from (a) Case ACRw and (b) Case NO_ACRw during January 8 to 28, 2015. Also shown are the differences in simulated PBLH at 20:00 local time (12:00 UTC) between (c) Case ACRw and Case NO_ACRw, (d) Case ARIw and Case NO_ACRw, and (e) Case ACIw and Case NO_ACRw during January 8 to 28, 2015.
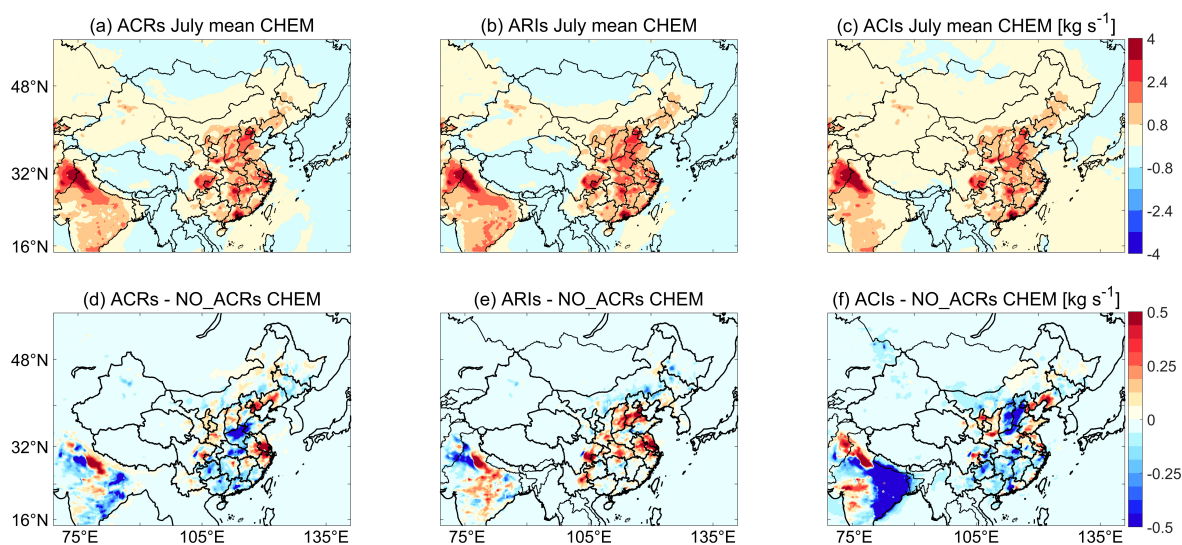
Figure 15: Mean simulated chemical mass tendency (unit: $kg\,s^{-1}$) for afternoon boundary-layer ozone from (a) Case ACRs, (b) Case ARIs, and (c) Case ACIs during July 2016. Also shown are the differences in simulated chemical mass tendencies for afternoon boundary-layer ozone between (d) Case ACRs and Case NO_ACRs, (e) Case ARIs and Case NO_ACRs, and (f) Case ACIs and Case the NO_ACRs in July 2016.

R1.4 Considerations of ARI and ACI in the WRF-GC v2.0 can alter a variety of meteorological factors in addition to the surface temperature and shortwave radiation as mentioned in the manuscript. Authors should add the analysis for the impacts of ARI and ACI on other meteorological factors, such as planetary boundary layer, relative humidity, and so on.

Thanks for your suggestions. We diagnosed the response of wintertime surface $PM_{2.5}$ to ARI through modulation of surface air temperature and PBLH (Section 5.2), as well as the response of summertime surface afternoon ozone to through modulation of radiation and temperature (Section 5.3). We also pointed out that ARI and ACI may also affect other meteorological variables to alter air quality, and that such possibilities may be further investigated using WRF-GC.

P19, L566-572, Section 5.1

The simulated PBLH are also chemically-sensitive, especially in winter. Figure 12 compare the simulated mean

15

PBLH at 20:00 local time (12:00 UTC) from the sensitivity experiments during January 8 to 28, 2015. The simulated PBLH from Case ACRw (462 ± 176 m) better agrees with the observations (448 ± 129 m), compared to the simulated PBLH from Case NO_ACRw (491 ± 195 m). We find that the inclusion of ARI reduces the simulated PBLH throughout Eastern China, particularly over the Sichuan Basin. This response is consistent with previous studies that showed the strong aerosol extinction in winter has a positive feedback to surface $PM_{2.5}$ concentration via the compression of PBLH (Li et al., 2017; Zhang et al., 2018; Miao and Liu, 2019).

P20, L580-587, Section 5.2

Figures 12c,d,e show the combined and individual impacts of ARI and ACI on the simulated PBLH during January 8 to 28, 2015, relative to the simulation when both ARI and ACI are turned off. We find that the simulated response of surface $PM_{2.5}$ to ARI is spatially consistent with the simulated responses of SWDOWN, surface air temperature, and PBLH to ARI. Over the Sichuan Basin and parts of Northern and Central China, the strong aerosol extinction decrease the SWDOWN and surface air temperature, resulting in lower PBLH and a possibly more stable conditions within the PBL. The shallower and more stable PBL suppresses the dispersion of air pollutants, thus increasing surface $PM_{2.5}$ concentrations. These findings are consistent with previous studies (Wang et al., 2014; Li et al., 2017; Zhang et al., 2018), although other feedback mechanisms may also play a role.

R1.5 The results and discussion are too general. What would be benefits of the on-line model applications? If the purpose of the model update or development is to simulate the regional-scale interaction between meteorology and air pollutants, the modeling capability should be thoroughly validated as if other regional photochemical models conventionally do. Model performance evaluations against the surface measurements of the criteria air pollutants including PM2.5 and O3 are recommended. After that, model sensitivities with or without the ARI and ACI can show the results of the interactions.

Thanks for your suggestions. We added Tables 5 and 6 (shown in R1.1) to validate the control experiments (Cases

ACRs and ACRw) against observations, as well as to compare the performance of each sensitivity experiments in simulating regional meteorology and chemistry. We also revised the text to describe the validation of the control experiments against observations. We compared and discussed the impacts of ARI and ACI to simulated regional meteorology and surface air quality in Section 5. We also added Tables 5 and 6 to summarize the performance of the different sensitivity experiments. The validation for meteorological variables is shown in R1.2.

P19, L575-579, Section 5.2

Table 6 summarizes the assessment of the simulated surface $PM_{2.5}$ concentrations against surface measurements. The inclusion of ARI significantly increases the simulated surface $PM_{2.5}$ concentrations by 6 μg m^{-3} to 15 μg m^{-3} over parts of Northern and Southern China, and the Sichuan Basin, thereby improving the agreement with surface observations (Table 6, model versus observation slope = 0.97 in Case ACRw and 0.9 in Case NO_ACRw, respectively).

P20, L590-594, Section 5.3

Overall, the inclusion of ARI and ACI in WRF-GC slightly reduces the model's positive bias in simulated surface ozone concentration (Table 6; model versus observation slope is 1.33 in Case ACRs and 1.38 in Case NO_ACRs, respectively). By including both ARI and ACI, the simulated July afternoon surface ozone concentration decrease by 2 to 10 ppbv over Henan Province, the Sichuan Basin, and parts of Northeastern China.

R1.6 Specific comments and typos:

Line 407: Add a comma before the "2015" in 'during January 8 to 28, 2015'.

Line 414 : at 550 nm in July

Line 474 : Please revise the subscripts. (for example, PM$_{2.5}$ à PM2.5)

Corrected. Thank you for pointing out the mistakes.

P15, L430, Section 4.3

Figure 3a and 3c compare the AOD at 550 nm wavelength over East Asia as observed by VIIRS and as simulated by WRF-GC (Case ACRw) during January 8 to 28, 2015.

Figures 3b and 3d compare the observed and simulated (Case ACRs) mean AOD at 550 nm during July 2016.

P18, L518-519, Section 4.6

WRF-GC successfully captures the high $PM_{2.5}$ in Central China and over the Sichuan Basin but underestimates the $PM_{2.5}$ concentrations over the NCP.

2   Reviewer #2

This is a well-organized and written manuscript. Built on their previous work published on GMD, the authors further developed WRF-GC to enable feedbacks of aerosol-cloud and aerosol-radiation interactions. The latest model edition also supports the nest-domain capability. Both GEOS-Chem and WRF models are actively developed and embrace a large user base worldwide. Coupling them together is a great contribution to the modeling community. This reviewer recommends publication after minor revisions listed below.

R2.1 In the text, spell out all the acronyms, e.g., WRF-GC, CMAQ, COSMO, SSA, and many more, when they first appear.

Thank you for pointing out the omissions. We now spell out all acronyms when they first appear. For example:

P2, L39-44, Introduction

A number of two-way models are coupled using the online-access approach, including for example the online WRF-Community Multiscale Air Quality model (WRF-CMAQ) (Byun and Schere, 2006; Wong et al., 2012; Yu et al., 2014), the Global Environmental Multiscale-Air Quality model (GEM-AQ) (Kaminski et al., 2008), the Consortium for Small-Scale Modelling-Multiscale Chemistry Aerosol Transport model (COSMO-MUSCAT) (Wolke et al., 2004; Renner and Wolke, 2010), and the Integrated Forecast System-Model for Ozone And Related Tracers model (IFS-MOZART) (Flemming et al., 2009).

P7, L181-182, Section 2.2.2

In WRF, two shortwave radiation schemes are coupled to prognostic aerosol information: the Rapid Radiative Transfer Model for Global Circulation Model (RRTMG) shortwave radiation scheme (Iacono et al., 2008) and the Goddard shortwave radiation scheme (Chou and Suarez, 1994).

P7, L193, Section 2.2.2

The AOD is interpolated or extrapolated using the Ångström exponent method (Eck et al., 1999), while the single scattering albedo (SSA) and the asymmetry factor are linearly interpolated.

P12, L331-332, Section 3.5

The emission module of GEOS-Chem, the Harmonized Emissions Component (HEMCO), has also been updated to fully objectify its memory space (Keller et al., 2014; Lin et al., 2021).

R2.2 Line 45, replace "advances" with "advancement".

Changed as suggested. Thank you.

P2, L45-47, Introduction

As such, these stand-alone CTMs may be independently developed by a wider atmospheric chemistry community, and the resulting CTM advancement may be quickly incorporated into the coupled model via the online-access structure (Yu et al., 2014).

R2.3 Table 1, DST4 should be "dust bin 4".

Corrected as suggested. Thank you.

P46, Table 1

Table 1: Aerosol types in WRF-GC and their prescribed properties and size distributions

Name	Species	Molecular weight $(g \cdot mol^{-1})$	Density $(g \cdot cm^{-3})$	Hygroscopicity (unitless)	Log-normal distribution (Geometric mean dry diameter, μm)	Log-normal distribution (Geometric standard deviation, unitless)
SO4	sulfate	96	1.7	0.5	0.14	1.6
NIT	nitrate	62	1.8	0.5	0.14	1.6
NH4	ammonium	18	1.8	0.5	0.14	1.6
OCPI	hydrophilic primary OC	12	1.3	0.2	0.14	1.6
OCPO	hydrophobic primary OC	12	1.3	0.2	0.14	1.6
BCPI	hydrophilic BC	12	1.8	1.00E-06	0.04	1.6
BCPO	hydrophobic BC	12	1.8	1.00E-06	0.04	1.6
SALA	accumulation-mode sea salt (radius 0.1 - 0.5 μm)	31.4	2.2	1.16	0.18	1.5
SALC	coarse-mode sea salt (radius 0.5 - 4.0 μm)	31.4	2.2	1.16	0.8	1.8
DST1	dust bin 1 (radius 0.1 - 1.0 μm)	29	2.5	0.14	–	–
DST2	dust bin 2 (radius 1.0 - 1.8 μm)	29	2.65	0.14	–	–
DST3	dust bin 3 (radius 1.8 - 3.0 μm)	29	2.65	0.14	–	–
DST4	dust bin 4 (radius 3.0 - 6.0 μm)	29	2.65	0.14	–	–
SOAS	SOA (simple)	150	1.5	0.14	0.14	1.6

R2.4 Line 389, change "over than 440 nm" to "over 440 nm".

Corrected as suggested. Thank you.

P14, L410-412, Section 4.2.2

Holben et al. (1998) showed that the uncertainty of AERONET AOD under cloud-free condition was less than $\pm$ 0.01 for wavelengths over 440 nm.

R2.5 Line 400, why not include all the monitoring sites within a grid cell for model evaluation?

Thank you for the suggestion. We now calculate the averaged concentrations of $PM_{2.5}$ and ozone of all sites within a model grid cell for comparison with model simulations.We update the Figure 13 and validations as follows:

P15, L419-421, Section 4.2.3

For comparison between observations and model results, we calculate the average $PM_{2.5}$ and ozone measurements in a WRF-GC grid. In all, we compare model results to summertime ozone observations at 562 sites and wintertime $PM_{2.5}$ at 513 sites, respectively.

P18, L515-529, Section 4.6

WRF-GC reproduces the observed spatial distributions of $PM_{2.5}$ over Eastern China (eastward of 108° E); the spatial correlation between the observed and simulated $PM_{2.5}$ concentrations is 0.77. The simulated mean $PM_{2.5}$ concentration over Eastern China ($80.8 \pm 32.6 \ \mu g \ m^{-3}$) is 9.3% lower than the observations ($89.1 \pm 31 \ \mu g \ m^{-3}$).

WRF-GC also underestimates $PM_{2.5}$ over Western China, likely reflecting a low-bias in the model dust, also seen in the simulated AODs. WRF-GC also reproduces the temporal variation of hourly $PM_{2.5}$ during January 8 to 28, 2015. The temporal correlation coefficient between the observed and simulated hourly $PM_{2.5}$ averaged over all Chinese sites is 0.77.

WRF-GC reproduces the higher surface ozone concentrations over Northern and Central China, the relatively lower ozone concentrations near the South China coast, and the ozone hotspots over the megacity clusters (Beijing-Tianjin-Hebin, Yantze River Delta, and the Pearl River Delta). However, the surface afternoon ozone concentrations simulated by WRF-GC (64 ± 17 ppbv) is high-biased compared to the observations (51 ± 13 ppbv). The normalized mean bias of the simulation is 25.6%. The overestimation of surface ozone concentrations is most severe over Henan and Shanxi provinces in Northern China. The temporal correlation coefficient between the observed and simulated hourly afternoon ozone concentrations averaged over all sites is 0.67.
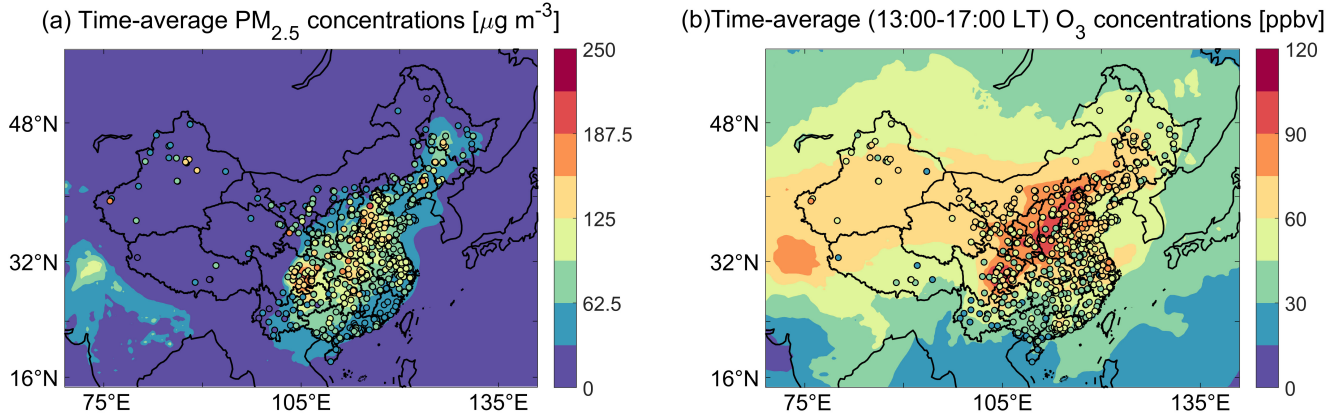
(a) Time-average PM$_{2.5}$ concentrations [μg m^{-3}]

(b) Time-average (13:00-17:00 LT) O$_3$ concentrations [ppbv]

Figure 13: (a) Mean observed (symbols) and simulated (Case ACRw, filled contours) PM$_{2.5}$ concentrations during January 8 to 28, 2015; (b) mean observed (symbols) and simulated (Case ACRs, filled contours) afternoon surface ozone concentrations (13:00 to 17:00 local time) during July 2016.

R2.6 Figure 3: it appears that WRF-GC severely underestimates monthly AOD across most of the domain in comparison with the VIIRS observations. What are the possible reasons? Is it mainly due to emissions, or meteorology (e.g., humidity)? A little in-depth analysis may provide useful information for both model improvement and satellite retrieval.

Thanks for pointing out this issue. Underestimation of satellite-based AOD observations by regional models is not uncommon (Gao et al., 2014; Gan et al., 2015; Xing et al., 2015; Zhang et al., 2016). Detailed investigation and remediation of the cause are certainly important but beyond the scope of the current manuscript. We expanded the text to raise three possible reasons based on previous studies: (1) incorrect assumption about the mixing state of aerosols in the model, (2) underestimation of aerosols in the model, and (3) high-bias in the satellite AOD products. We will explore the causes for the biases of AOD in a future work. We revised the manuscript as follows:

P16, L453-463, Section 4.3

Previous comparisons of AODs simulated by regional models against satellite observations also often found spatial consistency but significant low biases in the models (Gao et al., 2014; Gan et al., 2015; Xing et al., 2015;

23

Zhang et al., 2016). Curci et al. (2015) showed that the uncertainties for the model AODs are associated with the assumed mixing state, refractive indices, and hygroscopicity of aerosols. In particular, assumptions of the aerosol mixing state can lead to 30% to 35% uncertainty on the simulated AOD (Fassi-Fihri et al., 1997; Curci et al., 2015). In addition, the WRF-GC model may have underestimated the abundance of aerosols over China, as indicated by the slight underestimation of surface $PM_{2.5}$ concentrations shown below (Section 4.6). On the other hand, several studies showed that the regional distributions of AOD observed by VIIRS and MODIS are consistent with the AERONET measurements, but both VIIRS and MODIS observations are high-biased compared to AERONET observations over Asia (Wang et al., 2020). This high-bias in the satellite-observed AOD may partially account for the discrepancy between the simulated and satellite AODs. The cause of the discrepancy between observed and simulated AOD should be further investigated in future studies.

R2.7 Figure 4: why not converting the modeled AOD to the one at the observed wavelength for an apple-to-apple comparison?

Thank you for the suggestion. We now interpolate the simulated spectral AODs at 400 nm, 600 nm, and 999 nm to the observed spectral AODs at 500 nm, 675 nm, and 1020 nm based on the Ångström exponent method (Eck et al., 1999). This revision does not have a large impact on the temporal correlation coefficients between the simulated and observed spectral AODs. We updated the Figure 4 and revised the text as follows:

P15, L445-450, Section 4.3

At each site, we interpolate the simulated spectral AODs at 400 nm, 600 nm, and 999 nm to the AERONET observation wavelengths of 500 nm, 675 nm, and 1020 nm, respectively, using the Ångström exponent method (Eck et al., 1999).

The temporal correlation coefficients between the observed and simulated AODs at all sites and wavelengths range between 0.55 and 0.86, except for the correlation coefficient between the observed and simulated 500 nm
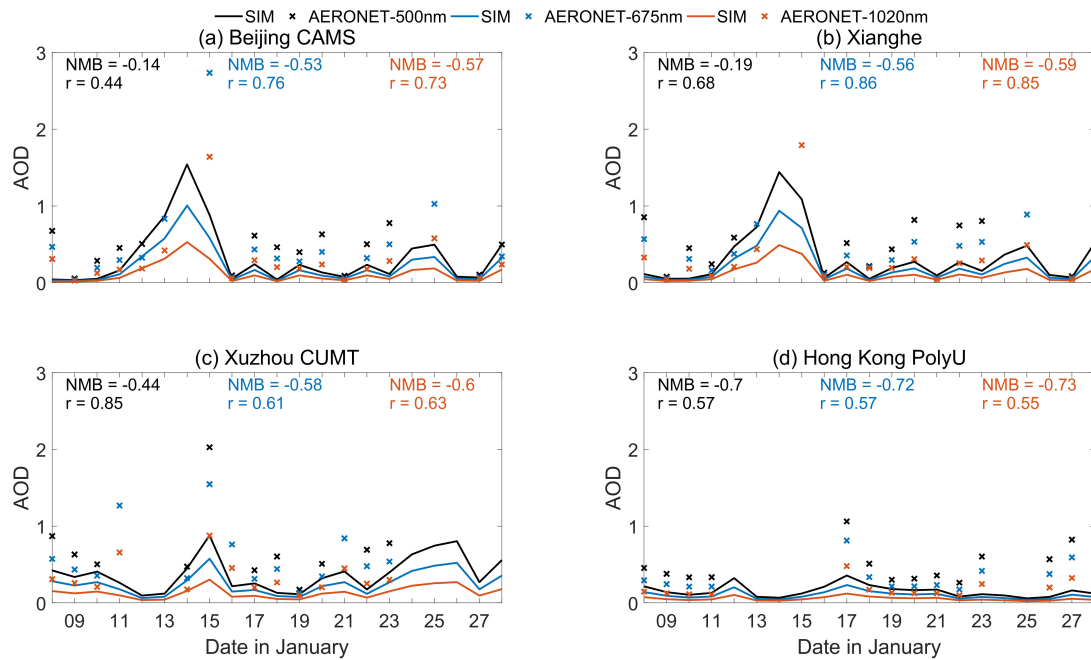
AOD in Beijing (0.44).

Figure 4: Comparison of simulated daily AOD (Case ACRw) against the AERONET daily AOD observations at 500 nm, 675 nm and 1020 nm at 4 sites during January 08 to January 28, 2015: (a) Beijing, (b) Xianghe, (c) Xuzhou, and (d) Hong Kong. Also shown are the normalized mean biases (NMBs) and the temporal correlation coefficients (r) between the simulated and observed spectral AODs.

R2.8 Line 451, add "cloud" after "stratocumulus or stratus".

R2.9 Line 474, change "2.5" in PM2.5 from superscript to subscript.

R2.10 Line 550, change "WRF-GC'se" to "WRF-GC's".

Corrected. Thank you for pointing out these mistakes.

P16, L477-479, Section 4.4

Satellite retrievals of cloud effective radii often show large biases, except over areas dominated by liquid stratocumulus or stratus cloud (Yan et al., 2015; Witte et al., 2018).

P18, L517-519, Section 4.6

WRF-GC successfully captures the high PM$_{2.5}$ in Central China and over the Sichuan Basin but underestimates the PM$_{2.5}$ concentrations over the NCP.

P21, L624-626, Section 6

We develop WRF-GC's nested-domain capability by improving the State Management Module and the memory-management in GEOS-Chem (implemented as of GEOS-Chem version 12.4.0).

R2.11 27 km resolution has been applied in the study for model evaluation. This resolution is too coarse to resolve cloud processes to which the ACI is important. Some discussion may be necessary to clarify this.

Thanks for pointing out the issue. Our simulations are conducted at a typical meso-scale resolution (27 km), with the cumulus parameterization (new Tiedtke) and the cloud microphysical scheme (Morrison two-moment) both turned on. Most meso-scale simulations of ACI are configure this way and thus consider only the feedback of aerosols to large-scale microphysics but do not explicity simulate the impacts of aerosol of sub-grid convective clouds (e.g., Wu et al. (2011); Zhao et al. (2017)). Wu et al. (2011) previously compared model simulations at 36-km resolution (with aerosol-sensitive large-scale microphysics and aerosol-insensitive cumulus parameterization) and at 4-km resolution (with only aerosol-sensitive large-scale microphysics). They found that the simulated sensitivity of clouds and precipitation to aerosols are similar in the meso-scale (36-km) and cloud-resolving (4-km) simulations. We revised the manuscript to clarify this.

P6, L175-180, Section 2.2.2

Most meso-scale simulations of ACI consider only the feedback of aerosols to large-scale microphysics but do not explicitly simulate the impacts of aerosol on sub-grid convective clouds (e.g., Wu et al. (2011); Zhao et al. (2017)). Also, most of the cumulus parameterization schemes in the standard WRF model (v3.9.1.1) do not respond explicitly to prognostic aerosol information. The only exception is the Grell-Freitas Ensemble scheme (Grell and Freitas, 2014), which parameterizes the conversion of cloud water to rain water as a function of prognostic cloud

condensation nuclei (CCN) number. The Grell-Freitas Ensemble scheme will be supported in a future version of WRF-GC.

R2.12 The ARI and ACI have been specifically linked to RRTMG scheme and Morrison two-moment microphysics scheme, respectively, in the application. Have the authors considered a more generalized method so that they can easily link to other radiation and microphysics schemes available to WRF?

Thanks for pointing out the lack of clarity. Our treatment of prognostic aerosol information in the WRF-GC Coupler for ARI and ACI calculations are already abstracted and generalized. These treatments in the WRF-GC Coupler can be easily applied to any other radiative and microphysical schemes that consider prognostic aerosol information. However, currently in the WRF model, only a few radiative and microphysical schemes can ingest prognostic aerosol information. All of these schemes (RRTMG shortwave and longwave, Goddard shortwave, Morrison two-moment microphysics, and Lin et al. microphysics) are supported by WRF-GC. We revised the text to clarify.

P6, L172-175, Section 2.2.2

Only a few radiative transfer and microphysics schemes in WRF are currently coupled to prognostic aerosol information, and WRF-GC v2.0 supports these existing schemes. However, our treatments of aerosol information in the two-way WRF-GC Coupler are abstracted and generalized, such that the Coupler may be extended to support other radiative and microphysical schemes in WRF in the future.

R2.13 Has WRF-GC already been included in the community WRF release? Or will it be included in the standard WRF release in the near future?

Thank you for pointing out the lack of clarity. WRF-GC, including its parent models and the Coupler (v2.0), is open-source and freely accessible from GitHub. WRF-GC has not been included in the standard WRF release, mainly

because the GEOS-Chem model is independent of WRF and is separately released. We revise the *Code availability* section to more clearly describe how to access the WRF-GC (v2.0) code.

P21, L641, Code availability

WRF-GC is free and open-source (`http://wrf.geos-chem.org`). The WRF-GC v2.0 Coupler can be downloaded from Github (`https://github.com/jimmielin/wrf-gc-release`, last accessed: May 9, 2021). The two parent models, WRF and GEOS-Chem, are also open-source and can be obtained from their developers at `https://github.com/wrf-model/WRF` (last accessed: May 9, 2021) and `http://www.geos-chem.org` (last accessed: May 9, 2021), respectively. The version of WRF-GC (v2.0) described in this paper supports WRF v3.9.1.1 and GEOS-Chem v12.7.2 and is permanently archived at `https://github.com/jimmielin/wrf-gc-pt2-paper-code-nested` (last accessed: December 27, 2020) (DOI: 10.5281/zenodo.4395258). The WRF-GC code used for the simulations described in Sections 4 and 5 is permanently archived at `https://github.com/jimmielin/wrf-gc-pt2-paper-code` (last accessed: December 19, 2020) (DOI: 10.5281/zenodo.4362624).

3   Reviewer #3

The paper presents a new online two-way coupled model WRF-GC v2.0 based on WRF meteorological model coupled with the GEOS-Chem chemical model including aerosol-radiation interactions (ARI) and aerosol-cloud interactions (ACI) based on bulk aerosol mass and composition, and nesting capability for high-resolution simulations. The authors also analyze chemical feedbacks to meteorology considering ARI and ACI mechanisms.

The paper is interesting and can be suitable for publication, but several comments need to be improved and clarified.

R3.1 The coupling structure modular, which allows the two parent models to be run off-line or online. This is definitely an advantage. However, it is difficult to classify this model as online-integrated coupled model. According to the definitions (Baklanov et al., 2014) it is still online-access coupling model, like WFR-CMAQ, because the equations of the meteo and chemical transport parts are solved separately, not on the same grid, not simultaneously in each grid-cell and not on each time step (at least it is not clear from the model description). So, in such way of coupling it is difficult to guarantee the consistency and mass-conservation. Besides, most probably the convection numerical schemes are different and not consistent in WRF and GEOS-Chem models.

Thank you for pointing out the lack of clarity in our original text. Actually, in the WRF-GC model, grid-scale advections of meteorological variables and chemical constituents are calculated with the same transport scheme; they are both performed by WRF model, on the same grid and at the same time. This is because the GEOS-Chem model is structured into modular units of atmospheric columns (Long et al., 2015; Eastham et al., 2018; Lin et al., 2020), which separates the calculation of grid-scale advection of chemical species from other chemical processes. When coupled to the dynamical models, such as the case in WRF-GC, the GEOS-Chem column model only performs convective transport, dry deposition, wet scavenging, emission, boundary layer mixing, and chemistry calculations within the vertical column. These processes are grid-independent in horizontal direction. In addition, in WRF-GC the horizontal resolution and location of GEOS-Chem vertical columns are managed by WRF, such that the meteorological and

chemical processes are solved on the same horizontal grid through operator-splitting (Baklanov et al., 2014). This treatment is exactly the same as that in the WRF-Chem model (Lin et al., 2020). Therefore, the WRF-GC model maintains mass-conservation and consistency for advection of meteorological variables and chemical species.

It is true that the convective mixing and PBL mixing schemes are not consistent in WRF and GEOS-Chem. The sub-grid vertical transports of chemical species, including convective transport (Allen et al., 1996; Wu et al., 2007) and boundary layer mixing (Lin and McElroy, 2010) are performed by GEOS-Chem and driven by WRF-simulated meteorological variables. More research is needed to investigate the impacts of this discrepancy on the two-way coupled WRF-GC model.

We revised the manuscript to more precisely describe the model framework of WRF-GC:

P4, L89-98, Section 2.1

A WRF-GC simulation is initialized and managed by WRF, which sets the global clock, dynamical and chemical time steps, domain, horizontal resolution, vertical coordinates, as well as initial/boundary conditions. In particular, the 3-D grid system is determined by WRF and is fully adopted by the GEOS-Chem chemical module in units of atmospheric columns. At each dynamical time step, WRF performs dynamical and physical calculations. WRF calculates the grid-scale advection of meteorological variables and chemical species using the same transport scheme (Wicker and Skamarock, 2002), on the same grid system, and at the same time steps, ensuring mass-conservation of the chemical species. At each chemical time step, the meteorological and chemical information is passed from WRF to GEOS-Chem through the WRF-GC Coupler. Then, the GEOS-Chem column model is called to perform convective mixing, dry deposition, emissions, planetary boundary-layer mixing, gas and aerosol chemistry, and wet scavenging (except advection), in this order, within each atmospheric column at WRF-specified horizontal locations (Lin et al., 2020).

R3.2 From other side, the model uses a coupler for data transfer from one model to other. Transfer of 3D data on each time step for each grid-cell will take a lot of time, that makes the modelling system substantially slower

in comparison with the fully online integrating approach. For example, ECMWF demonstrated that when they switched from the online-access version IFS-MOZART to the online integrated C-IFS (Huijnen et al., 2010), the modeling system became much faster.

So, it would be important to demonstrate the consistency tests and the effectiveness of the suggested way of the coupling.

Thank you for pointing this out. We added Section 3.6 to diagnose the computational performance of WRF-GC v2.0. We found that the increase in walll time in the two-way simulations relative to the one-way simulation is only slight (< 12%):

P13, L346-354, Section 3.6

We conduct two-day (June 27 to 29, 2019) simulations using the WRF-GC (v2.0) model and the GEOS-Chem Classic nested-grid model (v12.7.2), to compare their computational performance. Simulations with both models are configured with 245×181 atmospheric columns over China. The WRF-GC simulations have 50 vertical levels, while the GEOS-Chem Classic nested-grid simulation has 47 vertical levels. The WRF-GC model simulates meteorology online (2-min dynamical time step), while the GEOS-Chem Classic nested-grid simulation reads archived GEOS-FP assimilated meteorological dataset (`https://gmao.gsfc.nasa.gov/GMAO_products/`) and calculates advection at 5-min time step. All simulations use the same emissions, the same chemical module (GEOS-Chem column model), and identical chemical time steps. All simulations are performed on the same single-node hardware with 24 Intel Cascade Lake physical cores, 100 GB of RAM, and a networked Lustre high-performance file system. WRF-GC uses MPI parallelization, while GEOS-Chem Classic uses OpenMP parallelization.

Table 3 compares the simulation wall times for the WRF-GC v2.0 model (with various chemical feedback options) and for the GEOS-Chem Classic nested-grid model. Similar to our previous diagnosis (Lin et al., 2020), a one-way WRF-GC simulation (15282 s) is 53% faster than a similarly-configured GEOS-Chem Classic nested-grid simulation (33601 s). The better computational performance of WRF-GC is due to its faster dynamic calculations and its more

efficient parallelization of the chemical processes (Lin et al., 2020). The wall times for the two-way WRF-GC simulations with various combinations of chemical feedbacks (ARI only, ACI only, and both ARI and ACI) are all less than 11 % higher than the wall time for the one-way simulation. As expected, the slightly longer wall times in simulations with chemical feedbacks are mostly associated with the the extra calculations within the WRF-GC Coupler. The ARI calculations incur more wall time increases than the ACI calculations do. For reasons yet unclear, the wall time for the simulation with ARI only (17002 s) is slightly longer than that for the simulation with both ARI and ACI (16153 s). Nevertheless, in all WRF-GC simulations the coupling calculations are computationally economical and consume less than 9 % of the total wall times.

Table 3: Wall times of simulations conducted with the WRF-GC v2.0 model and the GEOS-Chem Classic nested-grid model (unit: s).

Model	WRF-GC v2.0				GEOS-Chem Classic nested grid
Experiment	One-way	ARI only	ACI only	ARI and ACI	v12.7.2
Total wall time	15378	17002	15283	16153	33601
Breakdown: WRF	7766	8374	7274	7511	-
Breakdown: GEOS-Chem	7242	7242	7591	7206	-
Breakdown: WRF-GC Coupler	370	1391	417	1436	-

References

Allen, D. J., Rood, R. B., Thompson, A. M., and Hudson, R. D.: Three-dimensional radon 222 calculations using assimilated meteorological data and a convective mixing algorithm, J. Geophys. Res. Atmos., 101, 6871–6881, https://doi.org/10.1029/95JD03408, 1996.

Baklanov, A., Schluenzen, K., Suppan, P., Baldasano, J., Brunner, D., Aksoyoglu, S., Carmichael, G., Douros, J., Flemming, J., Forkel, R., Galmarini, S., Gauss, M., Grell, G., Hirtl, M., Joffre, S., Jorba, O., Kaas, E., Kaasik, M., Kallos, G., Kong, X., Korsholm, U., Kurganskiy, A., Kushta, J., Lohmann, U., Mahura, A., Manders-Groot,

A., Maurizi, A., Moussiopoulos, N., Rao, S. T., Savage, N., Seigneur, C., Sokhi, R. S., Solazzo, E., Solomos, S., Sorensen, B., Tsegas, G., Vignati, E., Vogel, B., and Zhang, Y.: Online coupled regional meteorology chemistry models in Europe: current status and prospects, Atmos. Chem. Phys., 14, 317–398, https://doi.org/10.5194/acp-14-317-2014, 2014.

Byun, D. and Schere, K. L.: Review of the governing equations, computational algorithms, and other components of the Models-3 Community Multiscale Air Quality (CMAQ) modeling system, Appl. Mech. Rev., 59, 51–77, https://doi.org/10.1115/1.2128636, 2006.

Chen, F. and Dudhia, J.: Coupling an advanced land surface-hydrology model with the Penn State-NCAR MM5 modeling system. Part I: Model implementation and sensitivity, Mon. Weather Rev., 129, 569–585, https://doi.org/10.1175/1520-0493(2001)129<0569:CAALSH>2.0.CO;2, 2001a.

Chen, F. and Dudhia, J.: Coupling an advanced land surface-hydrology model with the Penn State-NCAR MM5 modeling system. Part II: Preliminary model validation, Mon. Weather Rev., 129, 587–604, https://doi.org/10.1175/1520-0493(2001)129<0587:CAALSH>2.0.CO;2, 2001b.

Chou, M. D. and Suarez, M. J.: An efficient thermal infrared radiation parameterization for use in general circulation models, NASA Tech. Memo., 104506, 3, 85pp, 1994.

Curci, G., Hogrefe, C., Bianconi, R., Im, U., Balzarini, A., Baró, R., Brunner, D., Forkel, R., Giordano, L., Hirtl, M., Honzak, L., Jiménez-Guerrero, P., Knote, C., Langer, M., Makar, P., Pirovano, G., Pérez, J., San José, R., Syrakov, D., Tuccella, P., Werhahn, J., Wolke, R., Žabkar, R., Zhang, J., and Galmarini, S.: Uncertainties of simulated aerosol optical properties induced by assumptions on aerosol physical and chemical properties: An AQMEII-2 perspective, Atmos. Environ., 115, 541 – 552, https://doi.org/10.1016/j.atmosenv.2014.09.009, 2015.

Eastham, S. D., Long, M. S., Keller, C. A., Lundgren, E., Yantosca, R. M., Zhuang, J., Li, C., Lee, C. J., Yannetti, M., Auer, B. M., Clune, T. L., Kouatchou, J., Putman, W. M., Thompson, M. A., Trayanov, A. L., Molod, A. M., Martin,

R. V., and Jacob, D. J.: GEOS-Chem High Performance (GCHP v11-02c): a next-generation implementation of the GEOS-Chem chemical transport model for massively parallel applications, Geosci. Model. Dev., 11, 2941–2953, https://doi.org/10.5194/gmd-11-2941-2018, 2018.

Eck, T., Holben, B., Reid, J., Dubovik, O., Smirnov, A., O'Neill, N., Slutsker, I., and Kinne, S.: Wavelength dependence of the optical depth of biomass burning, urban, and desert dust aerosols, J. Geophys. Res. Atmos., 104, 31 333–31 349, https://doi.org/10.1029/1999JD900923, 1999.

Fassi-Fihri, A., Suhre, K., and Rosset, R.: Internal and external mixing in atmospheric aerosols by coagulation: Impact on the optical and hygroscopic properties of the sulphate-soot system, Atmos. Environ., 31, 1393 – 1402, https://doi.org/10.1016/S1352-2310(96)00341-X, 1997.

Flemming, J., Inness, A., Flentje, H., Huijnen, V., Moinat, P., Schultz, M. G., and Stein, O.: Coupling global chemistry transport models to ECMWF's integrated forecast system, Geosci. Model. Dev., 2, 253–265, https://doi.org/10.5194/gmd-2-253-2009, 2009.

Gan, C. M., Pleim, J., Mathur, R., Hogrefe, C., Long, C. N., Xing, J., Wong, D., Gilliam, R., and Wei, C.: Assessment of long-term WRF–CMAQ simulations for understanding direct aerosol effects on radiation "brightening" in the United States, Atmos. Chem. Phys., 15, 12 193–12 209, https://doi.org/10.5194/acp-15-12193-2015, 2015.

Gao, Y., Zhao, C., Liu, X., Zhang, M., and Leung, L. R.: WRF-Chem simulations of aerosols and anthropogenic aerosol radiative forcing in East Asia, Atmos. Environ., 92, 250–266, https://doi.org/10.1016/j.atmosenv.2014.04.038, 2014.

Grell, G. A. and Freitas, S. R.: A scale and aerosol aware stochastic convective parameterization for weather and air quality modeling, Atmos. Chem. Phys., 14, 5233–5250, https://doi.org/10.5194/acp-14-5233-2014, 2014.

Holben, B., Eck, T., Slutsker, I., Tanre, D., Buis, J., Setzer, A., Vermote, E., Reagan, J., Kaufman, Y., Nakajima, T., Lavenu, F., Jankowiak, I., and Smirnov, A.: AERONET - A federated instrument network and data archive

for aerosol characterization, Remote Sens. Environ., 66, 1–16, https://doi.org/10.1016/S0034-4257(98)00031-5, 1998.

Hong, S.-Y., Noh, Y., and Dudhia, J.: A New Vertical Diffusion Package with an Explicit Treatment of Entrainment Processes, Mon. Weather Rev., 134, 2318–2341, https://doi.org/10.1175/MWR3199.1, 2006.

Iacono, M. J., Delamere, J. S., Mlawer, E. J., Shephard, M. W., Clough, S. A., and Collins, W. D.: Radiative forcing by long-lived greenhouse gases: Calculations with the AER radiative transfer models, J. Geophys. Res. Atmos., 113, https://doi.org/10.1029/2008JD009944, 2008.

Jimenez, P. A., Dudhia, J., Gonzalez-Rouco, J. F., Navarro, J., Montavez, J. P., and Garcia-Bustamante, E.: A Revised Scheme for the WRF Surface Layer Formulation, Mon. Weather Rev., 140, 898–918, https://doi.org/10.1175/MWR-D-11-00056.1, 2012.

Kaminski, J. W., Neary, L., Struzewska, J., McConnell, J. C., Lupu, A., Jarosz, J., Toyota, K., Gong, S. L., Côté, J., Liu, X., Chance, K., and Richter, A.: GEM-AQ, an on-line global multiscale chemical weather modelling system: model description and evaluation of gas phase chemistry processes, Atmos. Chem. Phys., 8, 3255–3281, https://doi.org/10.5194/acp-8-3255-2008, 2008.

Keller, C. A., Long, M. S., Yantosca, R. M., Da Silva, A. M., Pawson, S., and Jacob, D. J.: HEMCO v1.0: a versatile, ESMF-compliant component for calculating emissions in atmospheric models, Geosci. Model Dev., 7, 1409–1417, https://doi.org/10.5194/gmd-7-1409-2014, 2014.

Li, Z., Guo, J., Ding, A., Liao, H., Liu, J., Sun, Y., Wang, T., Xue, H., Zhang, H., and Zhu, B.: Aerosol and boundary-layer interactions and impact on air quality, Natl. Sci. Rev., 4, 810–833, https://doi.org/10.1093/nsr/nwx117, 2017.

Lin, H., Feng, X., Fu, T.-M., Tian, H., Ma, Y., Zhang, L., Jacob, D. J., Yantosca, R. M., Sulprizio, M. P., Lundgren, E. W., Zhuang, J., Zhang, Q., Lu, X., Zhang, L., Shen, L., Guo, J., Eastham, S. D., and Keller, C. A.: WRF-GC (v1.0): online coupling of WRF (v3.9.1.1) and GEOS-Chem (v12.2.1) for regional atmospheric chemistry

modeling – Part 1: Description of the one-way model, Geosci. Model Dev., 13, 3241–3265, https://doi.org/10. 5194/gmd-13-3241-2020, 2020.

Lin, H., Jacob, D. J., Lundgren, E. W., Sulprizio, M. P., Keller, C. A., Fritz, T. M., Eastham, S. D., Emmons, L. K., Campbell, P. C., Baker, B., Saylor, R. D., and Montuoro, R.: Harmonized Emissions Component (HEMCO) 3.0 as a versatile emissions component for atmospheric models: application in the GEOS-Chem, NASA GEOS, WRF-GC, CESM2, NOAA GEFS-Aerosol, and NOAA UFS models, Geosci. Model Dev. Discuss., 2021, 1–26, https://doi.org/10.5194/gmd-2021-130, URL `https://gmd.copernicus.org/preprints/gmd-2021-130/`, 2021.

Lin, J.-T. and McElroy, M. B.: Impacts of boundary layer mixing on pollutant vertical profiles in the lower troposphere: Implications to satellite remote sensing, Atmos. Environ., 44, 1726–1739, 2010.

Long, M. S., Yantosca, R., Nielsen, J. E., Keller, C. A., da Silva, A., Sulprizio, M. P., Pawson, S., and Jacob, D. J.: Development of a grid-independent GEOS-Chem chemical transport model (v9-02) as an atmospheric chemistry module for Earth system models, Geosci. Model Dev., 8, 595–602, https://doi.org/10.5194/gmd-8-595-2015, 2015.

Lu, X., Hong, J., Zhang, L., Cooper, O. R., Schultz, M. G., Xu, X., Wang, T., Gao, M., Zhao, Y., and Zhang, Y.: Severe Surface Ozone Pollution in China: A Global Perspective, Environ. Sci. Technol. Lett., 5, 487–494, https://doi.org/10.1021/acs.estlett.8b00366, 2018.

Miao, Y. and Liu, S.: Linkages between aerosol pollution and planetary boundary layer structure in China, Sci. Total. Environ., 650, 288–296, https://doi.org/10.1016/j.scitotenv.2018.09.032, 2019.

Morrison, H., Thompson, G., and Tatarskii, V.: Impact of Cloud Microphysics on the Development of Trailing Stratiform Precipitation in a Simulated Squall Line: Comparison of One- and Two-Moment Schemes, Mon. Weather Rev., 137, 991–1007, https://doi.org/10.1175/2008MWR2556.1, 2009.

Nakanishi, M. and Niino, H.: An improved mellor-yamada level-3 model: Its numerical stability and application to a regional prediction of advection fog, Bound.-Lay. Meteorol., 119, 397–407, https://doi.org/10.1007/s10546-005-9030-8, 2006.

Renner, E. and Wolke, R.: Modelling the formation and atmospheric transport of secondary inorganic aerosols with special attention to regions with high ammonia emissions, Atmos. Environ., 44, 1904 – 1912, https://doi.org/10.1016/j.atmosenv.2010.02.018, 2010.

Tiedtke, M.: A comprehensive mass flux scheme for cumulus parameterization in large-scale models, Mon. Weather. Rev., 117, 1779–1800, https://doi.org/10.1175/1520-0493(1989)117<1779:ACMFSF>2.0.CO;2, 1989.

Wang, J., Wang, S., Jiang, J., Ding, A., Zheng, M., Zhao, B., Wong, D. C., Zhou, W., Zheng, G., Wang, L., Pleim, J. E., and Hao, J.: Impact of aerosol-meteorology interactions on fine particle pollution during China's severe haze episode in January 2013, Environ. Res. Lett., 9, https://doi.org/10.1088/1748-9326/9/9/094002, 2014.

Wang, Y., Yuan, Q., Shen, H., Zheng, L., and Zhang, L.: Investigating multiple aerosol optical depth products from MODIS and VIIRS over Asia: Evaluation, comparison, and merging, Atmos. Environ., 230, 117 548, https://doi.org/10.1016/j.atmosenv.2020.117548, 2020.

Wicker, L. J. and Skamarock, W. C.: Time-Splitting Methods for Elastic Models Using Forward Time Schemes, Mon. Weather Rev., 130, 2088–2097, https://doi.org/10.1175/1520-0493(2002)130<2088:TSMFEM>2.0.CO;2, 2002.

Witte, M. K., Yuan, T., Chuang, P. Y., Platnick, S., Meyer, K. G., Wind, G., and Jonsson, H. H.: MODIS Retrievals of Cloud Effective Radius in Marine Stratocumulus Exhibit No Significant Bias, Geophys. Res. Lett., 45, 10,656–10,664, https://doi.org/10.1029/2018GL079325, 2018.

Wolke, R., Knoth, O., Hellmuth, O., Schröder, W., and Renner, E.: The parallel model system LM-MUSCAT for

chemistry-transport simulations: Coupling scheme, parallelization and applications, Adv. Par. Com., 13, 363–369, https://doi.org/10.1016/S0927-5452(04)80048-0, 2004.

Wong, D. C., Pleim, J., Mathur, R., Binkowski, F., Otte, T., Gilliam, R., Pouliot, G., Xiu, A., Young, J. O., and Kang, D.: WRF-CMAQ two-way coupled system with aerosol feedback: software development and preliminary results, Geosci. Model. Dev., 5, 299–312, https://doi.org/10.5194/gmd-5-299-2012, 2012.

Wu, L., Su, H., and Jiang, J. H.: Regional simulations of deep convection and biomass burning over South America: 2. Biomass burning aerosol effects on clouds and precipitation, J. Geophys. Res. Atmos., 116, https://doi.org/10.1029/2011JD016106, 2011.

Wu, S., Mickley, L. J., Jacob, D. J., Logan, J. A., Yantosca, R. M., and Rind, D.: Why are there large differences between models in global budgets of tropospheric ozone?, J. Geophys. Res. Atmos., 112, https://doi.org/10.1029/2006JD007801, 2007.

Xing, J., Mathur, R., Pleim, J., Hogrefe, C., Gan, C.-M., Wong, D. C., Wei, C., and Wang, J.: Air pollution and climate response to aerosol direct radiative effects: A modeling study of decadal trends across the northern hemisphere, J. Geophys. Res. Atmos., 120, 12,221–12,236, https://doi.org/10.1002/2015JD023933, 2015.

Yan, H., Huang, J., Minnis, P., Yi, Y., Sun-Mack, S., Wang, T., and Nakajima, T. Y.: Comparison of CERES-MODIS cloud microphysical properties with surface observations over Loess Plateau, J. Quant. Spectrosc. Ra., 153, 65–76, https://doi.org/10.1016/j.jqsrt.2014.09.009, 2015.

Yu, S., Mathur, R., Pleim, J., Wong, D., Gilliam, R., Alapaty, K., Zhao, C., and Liu, X.: Aerosol indirect effect on the grid-scale clouds in the two-way coupled WRF-CMAQ: model description, development, evaluation and regional analysis, Atmos. Chem. Phys., 14, 11 247–11 285, https://doi.org/10.5194/acp-14-11247-2014, 2014.

Zhang, C. and Wang, Y.: Projected future changes of tropical cyclone activity over the western North and

South Pacific in a 20-km-Mesh regional climate model, J. Climate, 30, 5923–5941, https://doi.org/10.1175/JCLI-D-16-0597.1, 2017.

Zhang, C., Wang, Y., and Hamilton, K.: Improved representation of boundary layer clouds over the southeast Pacific in ARW-WRF using a modified Tiedtke cumulus parameterization scheme, Mon. Weather Rev., 139, 3489–3513, https://doi.org/10.1175/MWR-D-10-05091.1, 2011.

Zhang, X., Zhang, Q., Hong, C., Zheng, Y., Geng, G., Tong, D., Zhang, Y., and Zhang, X.: Enhancement of PM2.5 Concentrations by Aerosol-Meteorology Interactions Over China, J. Geophys. Res. Atmos., 123, 1179–1194, https://doi.org/10.1002/2017JD027524, 2018.

Zhang, Y., Zhang, X., Wang, L., Zhang, Q., Duan, F., and He, K.: Application of WRF/Chem over East Asia: Part I. Model evaluation and intercomparison with MM5/CMAQ, Atmos. Environ., 124, 285–300, https://doi.org/10.1016/j.atmosenv.2015.07.022, 2016.

Zhao, B., Liou, K.-N., Gu, Y., Li, Q., Jiang, J. H., Su, H., He, C., Tseng, H.-L. R., Wang, S., Liu, R., Qi, L., Lee, W.-L., and Hao, J.: Enhanced PM2.5 pollution in China due to aerosol-cloud interactions, Sci. Rep., 7, https://doi.org/10.1038/s41598-017-04096-8, 2017.

WRF-GC (v2.0): online two-way coupling of WRF (v3.9.1.1) and GEOS-Chem (v12.7.2) for modeling regional atmospheric chemistry-meteorology interactions

Xu Feng[1], Haipeng Lin[2], Tzung-May Fu[3,4*], Melissa P. Sulprizio[2], Jiawei Zhuang[2], Daniel J. Jacob[2], Heng Tian[1], Yaping Ma[5], Lijuan Zhang[6], Xiaolin Wang[1], Qi Chen[7], and Zhiwei Han[8]

[1]Department of Atmospheric and Oceanic Sciences, School of Physics, Peking University, Beijing, China
[2]John A. Paulson School of Engineering and Applied Sciences, Harvard University, Cambridge, Massachusetts, USA
[3]State Environmental Protection Key Laboratory of Integrated Surface Water-Groundwater Pollution Control, School of Environmental Science and Engineering, Southern University of Science and Technology, Shenzhen, Guangdong, China
[4]Shenzhen Institute of Sustainable Development, Southern University of Science and Technology, Shenzhen, Guangdong, China
[5]National Meteorological Information Center, China Meteorological Administration, Beijing, China
[6]Shanghai Central Meteorological Observatory, Shanghai, China
[7]State Key Joint Laboratory of Environmental Simulation and Pollution Control, College of Environmental Sciences and Engineering, Peking University, Beijing, China
[8]Key Laboratory of Regional Climate-Environment for Temperate East Asia, Institute of Atmospheric Physics, Chinese Academy of Sciences, Beijing, China

Correspondence: Tzung-May Fu (fuzm@sustech.edu.cn)

Abstract. We present the WRF-GC model v2.0, an online two-way coupling of the Weather Research and Forecasting (WRF) meteorological model (v3.9.1.1) and the GEOS-Chem chemical model (v12.7.2). WRF-GC v2.0 is built on the modular framework of WRF-GC v1.0 and further includes aerosol-radiation interactions (ARI) and aerosol-cloud interactions (ACI) based on bulk aerosol mass and composition, as well as the capability to nest multiple domains for high-resolution simulations. WRF-GC v2.0 is the first implementation of the GEOS-Chem model in an open-source dynamic model with chemical feedbacks to meteorology. ~~We apply prescribed size distributions to the 10~~ In WRF-GC, meteorological and chemical calculations are performed on the exact same 3-D grid system; grid-scale advection of meteorological variables and chemical species uses the same transport scheme and time steps to ensure mass-conservation. Prescribed size distributions are applied to the aerosol types simulated by GEOS-Chem to diagnose aerosol optical properties and activated cloud droplet numbers; the results are passed to the WRF model for radiative and cloud microphysics calculations. WRF-GC is computationally efficient and scalable to massively-parallel architectures. We use WRF-GC v2.0 to conduct sensitivity simulations with different combinations of ARI and ACI over China during January 2015 and July ~~2016, with the goal of evaluating the simulated aerosol and cloud properties and the impacts of~~ 2016. Our sensitivity simulations show that including ARI and ACI ~~on~~ improves the model's performance in simulating regional meteorology and air quality. WRF-GC ~~reproduces the day-to-day variability of the aerosol optical depth (AOD) observed by the Aerosol Robotic Network (AERONET) project at four representative Chinese sites in January 2015, with temporal correlation coefficients of 0.56 to 0.85. The~~ generally reproduces the magnitudes and spatial ~~distributions of the simulated liquid cloud effective radii, liquid cloud optical depths, surface downward shortwave radiation,~~

and surface temperature over China for variability of observed aerosol and cloud properties and surface meteorological variables over East Asia during January 2015 and July 2016 are in good agreement with aircraft, satellite, and surface observations,

20 although WRF-GC consistently shows a low-bias against observed aerosol optical depths over China. WRF-GC simulations including both ARI and ACI reproduce the observed surface concentrations and spatial distributions of $PM_{2.5}$ in January 2015 (normalized mean bias = -6.6 -9.3 %, spatial correlation r = 0.74 0.77) and afternoon ozone in July 2016 (normalized mean bias = 19 25.6 %, spatial correlation r = 0.56) over Eastern China, respectively. Our sensitivity simulations show that including the ARI and ACI improved the model's performance in simulating ozone concentrations over China in July, 2016. . WRF-GC v2.0

25 is open source open-source and freely available from http://wrf.geos-chem.org.

1 Introduction

Interactions between atmospheric constituents and meteorological processes greatly impact regional weather and atmospheric chemistry (Zhang, 2008; Baklanov et al., 2014). Meteorological conditions affect the emissions of chemical constituents into the atmosphere from natural and anthropogenic sources, as well as the subsequent chemical reactions, transport, and removal of

30 those atmospheric constituents (Zhang et al., 2013; Zheng et al., 2015; Abel et al., 2017; Ma et al., 2020). In turn, atmospheric aerosols can exert radiative forcings either directly by scattering or absorption of solar and terrestrial radiation (i.e., aerosol-radiation interactions, ARI), or indirectly by altering the microphysical properties of clouds (i.e., aerosol-cloud interactions, ACI) (Hansen et al., 1997; Haywood and Boucher, 2000; Johnson et al., 2004; Lohmann and Feichter, 2005). Many studies have demonstrated that in areas with high aerosol concentrations, ARI and ACI can induce complex feedbacks to significantly

35 affect both regional meteorology and air quality (Li et al., 2007; Forkel et al., 2012; Ding et al., 2013; Wang et al., 2014a; Gong et al., 2015; Tao et al., 2015; Petaja et al., 2016; Li et al., 2017b; Zhao et al., 2017). We previously developed WRF-GC v1.0 (Lin et al., 2020), an one-way online coupling of the WRF (Skamarock et al., 2008, 2019) meteorological model meteorological model (Skamarock et al., 2008, 2019) and the GEOS-Chem (Bey et al., 2001) chemical model chemical model (Bey et al., 2001) for simulating regional air quality without aerosol feedbacks. Here, we present the development of WRF-

40 GC v2.0, which further includes ARI, ACI, and nested-domain capabilities to better simulate interactions between regional meteorology and air quality at high resolution.

The coupling between meteorological and chemical processes in regional models is typically achieved by one of two methodologies: *online-access coupling* or *online-integrated coupling* (Baklanov et al., 2014). Under the online-access coupling framework, a meteorological model and a chemical transport model (CTM) separately simulate regional meteorology

45 and atmospheric chemistry. At regular time intervals during run-time, they exchange meteorological and chemical data interpolated to the other model's grids and time to drive subsequent calculations. The meteorological model and the CTM may work with different map projections and 3-D grids, and they may use different transport schemes for meteorological and chemical variables. A number of two-way models are coupled using the online-access approach, including for example the online WRF-CMAQ model WRF-Community Multiscale Air Quality model (WRF-CMAQ) (Byun and Schere, 2006; Wong et al.,

50 2012; Yu et al., 2014), the GEM-AQ model Global Environmental Multiscale-Air Quality model (GEM-AQ) (Kaminski et al.,

2008), the ~~COSMO-MUSCAT model~~ Consortium for Small-Scale Modelling-Multiscale Chemistry Aerosol Transport model (COSMO-MUSCAT) (Wolke et al., 2004; Renner and Wolke, 2010), and the ~~IFS-MOZART model (Flemming et al., 2009). In many~~ Integrated Forecast System-Model for Ozone And Related Tracers model (IFS-MOZART) (Flemming et al., 2009). Often, the CTM in online-access ~~models, the CTMs can also~~ models can also stand-alone and be driven by offline mete-

orological data~~to stand alone~~. As such, these stand-alone CTMs may be independently developed by a wider atmospheric chemistry community, and the resulting CTM ~~advances~~ advancement may be quickly incorporated into the coupled model via the online-access structure (Yu et al., 2014).

Alternatively, regional coupled models may adopt an online-integrated structure, where the chemical module is an internal component of the coupled model. This structure entails meteorological and chemical calculations be performed on the same grids with the same time-stepping system. A major advantage of the online-integrated models is that meteorological and chemical data do not need to be interpolated in time or space for the coupling. Also, the transport schemes for meteorological and chemical quantities are generally consistent in online-integrated models, which better ensures mass-conservation (Zhang, 2008). An example of the online-integrated coupled structure is the WRF-Chem model (Grell et al., 2005; Fast et al., 2006), which consists of the WRF model and a chemical module; that chemical module is called by WRF at each chemical time step. ~~The~~ WRF-Chem ~~model~~ includes options to turn on ARI and ACI, either individually and combined. WRF-Chem has been widely used to study regional air quality, meteorology, and their interactions (Zhang et al., 2010; Huang et al., 2016; Archer-Nicholls et al., 2016; Zhang et al., 2018). However, the chemical module in WRF-Chem cannot stand alone as a CTM.

The WRF-GC model ~~was~~ is developed using the online-integrated structure, with WRF calling the GEOS-Chem column model as an internal chemical module (Lin et al., 2020). ~~At the same time,~~ The exact same GEOS-Chem column model is also used by the GEOS-Chem ~~model can stand alone as an offline CTMand~~ Classic model to form a stand-alone, offline CTM, which has been actively developed by the atmospheric chemistry community (Bey et al., 2001; Eastham et al., 2018). This architecture of the WRF-GC model ~~was~~ is made possible by the recent "modularization" of the GEOS-Chem model. GEOS-Chem was previously (before v11.01) an offline CTM, driven by archived meteorological data at several static sets of global or regional 3-D grids, with prescribed horizontal and vertical resolutions (Bey et al., 2001). Long et al. (2015) and Eastham et al. (2018) modularized the core chemical processes in GEOS-Chem, including emissions, chemistry, convective mixing, planetary boundary layer mixing, and deposition processes, to work in modular units of 1-D atmospheric vertical columns. Information about the horizontal and vertical grids, formerly fixed at compile-time, are now passed to the GEOS-Chem ~~chemical module~~ column model at run-time (Long et al., 2015; Eastham et al., 2018; Lin et al., 2020). This modularization allows the same GEOS-Chem chemical code to be either driven by offline meteorological data (i.e., as a CTM) or be coupled online to dynamical models (Long et al., 2015; Eastham et al., 2018). To date, GEOS-Chem has been coupled to the NASA GEOS-5 earth system model (Hu et al., 2018), to the Beijing Climate Center atmospheric general circulation model (Lu et al., 2020), and to the WRF regional meteorological model (Lin et al., 2020) in distributed-memory frameworks for parallel computation.

WRF-GC v2.0 is the first implementation of the GEOS-Chem column model in an open-source dynamic model with chemical feedbacks to meteorology.

In this paper, we describe the development of WRF-GC v2.0 , which includes the implementation of ARI, ACI, and the nested-domain capability. WRF-GC v2.0 allows GEOS-Chem users to investigate meteorology-atmospheric chemistry interactions at a wide range of resolutions. WRF-GC also offers other regional modellers access to the GEOS-Chem chemical core, which is actively developed by a large user community and consistent with that in the GEOS-Chem Classic offline CTM. WRF-GC v2.0 follows the modular coupling architecture of WRF-GC v1.0 (Section 2). In Section 3, we describe the representation of ARIand ACIin WRF-GC, which are implemented in the development of ARI, ACI, and the nested-domain capability in WRF-GC Coupler and abstracted from the parent modelsv2.0. In Section 4, we conduct a series of model experiments to evaluate the model performance at simulating meteorological fields and surface air pollutants over China, as well as to assess the performance of WRF-GC in simulating regional meteorology and air quality against satellite and surface measurements. Finally, we assess the impacts of ARI and ACI on regional meteorology and chemistry in Section 5.

2 Overview of the WRF-GC two-way coupled model architecture and its parent models

2.1 Architecture of the WRF-GC two-way coupled model

Figure 1 shows the architecture of the WRF-GC model, which consists of the two parent models (WRF and GEOS-Chem), and a WRF-GC coupler Coupler that is completely independent of both parent models. This architecture allows WRF-GC to use native, unmodified versions of the parent models, either one of which can be independently updated (Lin et al., 2020). In WRF-GC v1.0, the Coupler consists of a state conversion module, a state management module, and the GEOS-Chem column interface (Long et al., 2015; Eastham et al., 2018; Lin et al., 2020). These modules manage the meteorological and chemical information in distributed memory and perform state conversions between the two models at runtime.

A WRF-GC simulation is initialized and managed by WRF, which sets the global clock, grids, and dynamical and chemical time steps, domain, horizontal resolution, vertical coordinates, as well as initial/boundary conditions. WRF In particular, the 3-D grid system is determined by WRF and is fully adopted by the GEOS-Chem chemical module in units of atmospheric columns. At each dynamical time step, WRF performs dynamical and physical calculations, including the advection of chemical species, at each dynamical time step. WRF calculates the grid-scale advection of meteorological variables and chemical species using the same transport scheme (Wicker and Skamarock, 2002), on the same grid system, and at the same time steps, ensuring mass-conservation of the chemical species. At each chemical time step, the meteorological and chemical information is passed from WRF to GEOS-Chem through the WRF-GC Coupler. Then, the GEOS-Chem then performs column model is called to perform convective mixing, dry deposition, emissions, planetary boundary-layer mixing, gas and aerosol chemistry, and wet scavenging (except advection), in this order, within each atmospheric column at WRF-specified horizontal locations (Lin et al., 2020). Chemical information is then passed back to WRF for the next time step. At the end of the simulation, WRF finalizes the simulation and output outputs the meteorological and chemical outcomes. In WRF-GC v1.0, the only chemistry-relevant operation performed by WRF is the grid-scale advection of chemical species; the chemical species do not otherwise interact with the WRF model.

In ~~this work, we have implemented the ARI and the ACI into~~ WRF-GC v2.0, we implement ARI and ACI in the two-way WRF-GC Coupler. Figure 1a shows the two-way WRF-GC Coupler, which extends the capabilities of the one-way Coupler by the addition of three modules: (1) the `Diag_Aero_Size_Info_Module`, (2) the `optical_driver`, and (3) the
120 `mixactivate_driver`. These three modules diagnose the aerosol information from GEOS-Chem for the radiative transfer and cloud microphysics calculations in WRF. Figure 1b shows the workflow of the three new modules in WRF-GC v2.0. Users can switch on ARI or ACI by specifying `aer_ra_feedback=1` or `aer_cu_feedback=1`, respectively, in the WRF-GC configuration file (`namelist.input`). If ARI and ACI are both turned off, WRF-GC v2.0 will default to the one-way coupled simulation ~~(Lin et al., 2020)~~.

125 When users turn on the ARI, ACI, or both, the three new modules are called by the WRF-to-Chemistry Interface (`chem_driver`) at the end of each chemical time step. The `Diag_Aero_Size_Info_Module` diagnoses the bulk aerosol mass information from GEOS-Chem (Section 2.2.1) and converts them into the sectional aerosol mass and number concentrations in specified size bins using prescribed size distributions (~~described in detail in~~ Section 3.1). The sectional aerosol information is then used by the `optical_driver` (Section 3.3) and by the `mixactivate_driver` (Section 3.4) to calculate the aerosol
130 and cloud optical properties and the activated cloud droplet number concentrations, respectively. The prognostic aerosol and cloud information is then passed to the WRF model to be used by the radiative transfer (`module_radiation_driver`) and cloud microphysics (`module_microphysics_driver`) calculations at the next time step.

The diagnostic variables of aerosol mass and number concentrations are added into the WRF-GC registry file (`registry.chem`). Users can specify which variables to output in the registry file~~. When WRF-GC is compiled,~~, and WRF will build ~~all~~ the output
135 arrays ~~based on the information in the registry file~~ when WRF-GC is compiled. Below we describe the details of the WRF and GEOS-Chem models pertinent to the two-way coupling. Further details on the two-way WRF-GC Coupler calculations are given in Section 3.

2.2 Parent models

2.2.1 The GEOS-Chem model

140 WRF-GC v2.0 currently uses GEOS-Chem v12.7.2 (doi: 10.5281/zenodo.3701669) as its chemical module, but users ~~can also subsequently update the chemical module~~ are also able to update to the latest standard version of GEOS-Chem through the existing WRF-GC architecture. The ~~treatments for emissions, convective transport, boundary-layer mixing, gas and aerosol chemistry, dry deposition, and wet scavenging of chemical species~~ chemical processes in GEOS-Chem v12.7.2 are mostly the same as those in GEOS-Chem v12.2.1, which is used in WRF-GC v1.0 and described in detail in Lin et al. (2020). The
145 standard chemical mechanism in GEOS-Chem v12.7.2 includes a comprehensive O_x-NO_x-VOC-halogen-aerosol chemical mechanism in the troposphere and uses the Unified tropospheric-stratospheric chemistry extension (UCX) for stratospheric chemistry (Eastham et al., 2014). One of the critical updates in GEOS-Chem v12.7.2 is ~~that the~~ the reduced sensitivity of surface resistance to temperature ~~is reduced~~ (Jaeglé et al., 2018). Also, the bulk surface resistance of nitric acid is updated to $1 \, \mathrm{s \cdot cm^{-1}}$ to reflect its high affinity for natural surfaces. These updates increase the dry deposition velocities of the nitric acid

150 and nitrate, thereby correcting ~~the~~ previous overestimation of surface nitrate concentrations, especially in winter (Jaeglé et al., 2018).

Aerosol species in the standard GEOS-Chem chemical mechanism include primary dust, sea salt, primary organic carbon aerosol (POC), primary black carbon aerosol (BC), secondary inorganic aerosols (sulfate, nitrate, ammonium), and secondary organic aerosols (SOA) (Table 1). Sea salt aerosol masses in GEOS-Chem are simulated in two size ranges: the accumulation

155 mode (dry radii between 0.1 and 0.5 μm) and the coarse mode (dry radii between 0.5 and 4 μm) (Jaeglé et al., 2011). Dust aerosol masses are simulated in 4 size ranges, with effective radii of 0.7 μm, 1.4 μm, 2.4 μm, and 4.5 μm, respectively (Fairlie et al., 2007). All other aerosol species are simulated by their individual bulk masses, assuming static log-normal dry size distributions for each species (Martin et al., 2003; Drury et al., 2010; Jaeglé et al., 2011). Secondary inorganic aerosols are simulated with the ISORROPIA II algorithm (Fountoukis and Nenes, 2007). Freshly emitted POC and BC aerosols are assumed

160 to be 50% hydrophobic and 50% hydrophilic, with a 1.2-day conversion timescale from hydrophobic to hydrophilic (Wang et al., 2014b). Primary organic aerosol masses are estimated from POC mass using either a default global organic aerosol to organic carbon (OA/OC) mass ratio of 2.1 or spatiotemporally-varying OA/OC ratios (Philip et al., 2014). GEOS-Chem ~~model~~ provides two options for simulating the formation of SOA. By default, GEOS-Chem uses the "simple SOA" scheme: biogenic isoprene and monoterpene, as well as CO emitted from anthropogenic and biomass burning ~~activities~~sources, are

165 taken as ~~SOA precursors , which form SOA irreversibly~~ proxy precursors to irreversibly form SOA at specified mass yields on a ~~timescale of 1 day~~ 1-day timescale (Kim et al., 2015; Pai et al., 2020). This scheme simulates relatively accurate amounts of SOA without detailed chemical calculations (Miao et al., 2020). Alternatively, GEOS-Chem can ~~calculate complex SOA formation based on the~~ also use a volatility basis set (VBS) scheme (Robinson et al., 2007; Pye et al., 2010) ~~. Oxidation of monoterpene and sesquiterpene form semivolatile products, while oxidation of light aromatics form intermediate volatility~~

170 ~~products (Pye et al., 2010)~~to calculate complex SOA formation from the oxidation of monoterpenes, sesquiterpenes, and light aromatics. The complex SOA scheme also includes SOA formed via the aqueous-phase reactions of oxidation products from isoprene (Marais et al., 2016).

GEOS-Chem assumes static, log-normal dry size distributions for its simulated bulk aerosol species (except dust)~~for photolysis and heterogeneous chemistry calculations (Martin et al., 2003; Drury et al., 2010; Jaeglé et al., 2011). In addition, GEOS-Chem~~

175 ~~uses~~, as well as prescribed aerosol hygroscopicity and optical properties at multiple wavelengths under different relative humidity~~from the Global Aerosol Data Set (GADS) (Köpke et al., 1997; Martin et al., 2003) and updates from Latimer and Martin (2019)~~, for photolysis and heterogeneous chemistry calculations

(Köpke et al., 1997; Martin et al., 2003; Drury et al., 2010; Jaeglé et al., 2011; Latimer and Martin, 2019).

In ~~addition to the standard representation of aerosols described above,~~ this work, we developed the two-way WRF-GC

180 Coupler based on the standard bulk-mass representation of aerosol and the simple SOA scheme, involving the 14 aerosol types shown in Table 1. The goal is to include the ARI and ACI in WRF-GC while maintaining high computational efficiency. GEOS-Chem offers two optional schemes for ~~sectional aerosol size-bin~~ size-resolved aerosol simulations: the Advanced Particle Microphysics ~~scheme~~ (APM) (Yu and Luo, 2009) and the TwO-Moment Aerosol Sectional microphysics packages (TOMAS) ~~microphysics packages~~ (Kodros and Pierce, 2017). These ~~options~~ schemes more accurately simulate size-dependent aerosol

chemistry and microphysics, albeit at higher computational costs~~. However, these two size-resolved aerosol schemes~~, but they are not yet supported by the ~~WRF-GC Coupler.~~

~~In this work, we developed the two-way WRF-GC Coupler based on the standard bulk-mass representation of aerosol and the simple SOA scheme, involving the 10 aerosol species shown in Table 1. The goal is to include the ARI and ACI in WRF-GC while maintaining high computational efficiency.~~ GEOS-Chem column interface. Our developed WRF-GC Coupler with ARI and ACI can be extended to the APM and TOMAS schemes in the future, once those two schemes become compatible with the GEOS-Chem column interface.

2.2.2 The WRF model

WRF-GC v2.0 currently uses the WRF model (v3.9.1.1) to perform online calculations of meteorological processes, advection of chemical species, cloud microphysics, and radiative transfer with aerosol effects. WRF is a mesoscale numerical weather model for research and operational applications (Skamarock et al., 2008, 2019). WRF simulates atmospheric dynamics by solving fully compressible, Eulerian non-hydrostatic equations on either hybrid sigma-eta (default) or terrain-following vertical coordinates. WRF uses the staggered Arakawa C-horizontal grids at resolutions of 100 km to 1 km and supports Lambert-conformal, Mercator, latitude-longitude, and polar stereographic projections. WRF offers multiple parameterization options for cloud microphysics, cumulus parameterization, planetary boundary layer physics, shortwave/longwave radiative transfer, and land surface physics (Skamarock et al., 2019). The options currently supported in WRF-GC are listed in Lin et al. (2020). ~~To develop the ARI and ACI capabilities in~~

Only a few radiative transfer and microphysics schemes in WRF are currently coupled to prognostic aerosol information, and WRF-GC v2.0 ~~, we use the radiative transfer and microphysics~~ supports these existing schemes. However, our treatments of aerosol information in the two-way WRF-GC Coupler are abstracted and generalized, such that the Coupler may be extended to support other radiative and microphysical schemes in WRF ~~that have been already coupled to the WRF-Chem model (Grell et al., 2005; Fast et al., 2006; Chapman et al., 2009), as described below.~~ in the future. Most meso-scale simulations of ACI consider only the feedback of aerosols to large-scale microphysics but do not explicitly simulate the impacts of aerosol on sub-grid convective clouds (e.g., Wu et al. (2011); Zhao et al. (2017)). Also, most of the cumulus parameterization schemes in the standard WRF model (v3.9.1.1) do not respond explicitly to prognostic aerosol information. The only exception is the Grell-Freitas Ensemble scheme (Grell and Freitas, 2014), which parameterizes the conversion of cloud water to rain water as a function of prognostic cloud condensation nuclei (CCN) number. The Grell-Freitas Ensemble scheme will be supported in a future version of WRF-GC.

In WRF, two shortwave radiation schemes ~~have already been coupled to the~~ are coupled to prognostic aerosol information~~from WRF-Chem: the RRTMG~~: the Rapid Radiative Transfer Model for Global Circulation Model (RRTMG) shortwave radiation scheme (Iacono et al., 2008) and the Goddard shortwave radiation scheme (Chou and Suarez, 1994). The RRTMG shortwave radiation scheme includes atmospheric Rayleigh scattering, molecular absorption by water vapor, ozone, oxygen, carbon dioxide, and methane, as well as the radiative extinction by clouds and aerosols in 14 spectral bands between 0.2 and 12.2 μm. The Goddard shortwave radiation scheme includes 11 spectral bands between 0.175 and 10 μm. It calculates atmo-

spheric Rayleigh scattering, absorption by water vapor, ozone, oxygen, and carbon dioxide, as well as scattering and absorption
by clouds and aerosols. For longwave radiation, only the RRTMG scheme (Iacono et al., 2008) has been coupled to prognostic
aerosol information. The RRTMG longwave radiation scheme accounts for the absorption by water vapor, carbon dioxide,
ozone, methane, oxygen, nitrous oxide, nitrogen, several halocarbons, as well as cloud and aerosols.

When ARI is turned on (`aer_ra_feedback=1` in `namelist.input`), ~~the WRF model~~ WRF will ingest prognostic
bulk aerosol optical information from the interface with the chemistry module. WRF further interpolates the aerosol optical
properties to the specific wavelengths compatible with the shortwave radiation schemes. The AOD is interpolated or extrap-
olated using the Ångström exponent method (Eck et al., 1999), while the ~~SSA~~ single scattering albedo (SSA) and the asym-
metry factor are linearly interpolated. If ARI is turned off (`aer_ra_feedback=0` in `namelist.input`), the ~~RRTMG
scheme ignores~~ radiative schemes ignore the aerosol effects on radiation (`aer_opt=0` in `namelist.input`), or ~~uses~~ use
climatological aerosol data from Tegen et al. (1997) (`aer_opt=1`), or ~~uses~~ use the user-defined aerosol optical properties
(`aer_opt=2`) specified in the WRF-GC configuration file (`namelist.input`).

For ACI, only two cloud microphysical schemes in the WRF model ~~have been~~ are coupled to prognostic aerosol information:
the Lin et al. scheme (Lin et al., 1983; Chen and Sun, 2002) and the Morrison two-moment scheme (Morrison et al., 2009). WRF
uses an aerosol activation scheme developed by Abdul-Razzak and Ghan (2000, 2002). When ACI is turned on (`progn=1`
and `naer=ignored` in `namelist.input`), the interface to the chemical module will call the aerosol activation scheme to
diagnose the activated cloud droplet number in a time step. This calculation is based on a maximum supersaturation determined
by the mass concentrations, number densities, and hygroscopic properties of aerosols, as well as the local air temperature and
updraft velocity. Also, the radiation module in WRF uses the prognostic liquid cloud effective radii to compute the liquid cloud
optical depths (LCODs). If ACI is turned off, WRF either diagnoses the activated cloud droplet number using a prescribed
aerosol number and size distribution (`progn=1` and `naer=specified`) or uses a constant source of activated cloud droplets
($100\,\mathrm{cm}^{-3}$ per time step in the Lin et al. scheme and $250\,\mathrm{cm}^{-3}$ per time step in the Morrison two-moment scheme) (`progn=0`).
~~Also, WRF uses constant values of liquid cloud effective radii to calculate LCODs~~ In the event where WRF do use a constant
source of activated cloud droplets, the predicted cloud droplet number will effectively be around that prescribed number. Also,
if ACI is turned off~~. The Goddard shortwave radiation scheme assumes a constant effective radius of 10 for liquid cloud
droplets. The RRTMG scheme assumes the effective radius of liquid cloud droplets to be 8 over land and 14 over the ocean~~,
WRF uses prescribed constant values of liquid cloud effective radii to calculate LCODs.

3 New developments in WRF-GC v2.0

~~In Section 2, we describe the overall architecture of WRF-GC v2.0.~~ Here, we describe the detailed diagnostics performed
in the two-way WRF-GC Coupler to communicate aerosol and cloud information between GEOS-Chem and WRF. Some of
our diagnostics are developed by imitating the connections between WRF and the chemical module in the WRF-Chem model
(Grell et al., 2005; Fast et al., 2006; Chapman et al., 2009). We also describe the software engineering developments that enable
nested-domain simulations in WRF-GC v2.0.

3.1 Diagnosing the size and number of dry aerosols

The size distribution of aerosol is a critical property that affects its optical effects and its ability to be activated into CCN. We ~~developed the (~~develop the `Diag_Aero_Size_Info_Module` ~~)~~ to diagnose the sectional size distribution of aerosol mass and number concentrations from the bulk aerosol masses simulated by GEOS-Chem. For each of the aerosol types (except dust) in GEOS-Chem, we distribute the aerosol dry masses into 4 effective dry diameter bins used by WRF-GC. We assume the aerosol within each size bin to be internally mixed. The lower and upper dry diameter bounds of the 4 bins (Table 2) are from the Model for Simulating Aerosol Interactions and Chemistry (MOSAIC) 4-bins sectional parameterization (Zaveri et al., 2008). With the exception of dust, we ~~assumes~~ assume that the number density of aerosol type i ~~followed~~ follows a log-normal distribution (Eq. 1):

$$n_i(\ln D_i) = \frac{dN}{d\ln D_i} = \frac{N}{\sqrt{2\pi}\ln\sigma_i}\exp[-\frac{(\ln D_i - \ln D_{g,i})^2}{2\ln^2\sigma_i}] \tag{1}$$

where D_i is the particle dry diameter, and N is the total number concentration of the internally-mixed particles. $n_i(\ln D_i)$ is the number concentration density as a function of $\ln D_i$. $D_{g,i}$ and σ_i are the effective geometric mean dry diameter and the effective geometric standard deviation of the log-normal distribution, respectively ~~, which are prescribed for each aerosol type~~ (Table 1). Thus, the mass concentration density of the ith aerosol type ($m_i(\ln D_i)$) can be expressed using D_i, $n_i(\ln D_i)$, and the density of aerosol type i (ρ_i), as shown in Eq. 2:

$$m_i(\ln D_i) = \rho_i \cdot \frac{\pi D_i^3}{6} \cdot n_i(\ln D_i) = \rho_i \cdot \frac{\pi D_i^3}{6} \cdot \frac{N}{\sqrt{2\pi}\ln\sigma_i}\exp[-\frac{(\ln D_i - \ln D_{g,i})^2}{2\ln^2\sigma_i}] \tag{2}$$

Table 1 summarizes the prescribed values of $D_{g,i}$, σ_i, and ρ_i for ~~the aerosol types~~ each aerosol type used in our two-way WRF-GC Coupler. The $D_{g,i}$ and σ_i for secondary inorganic aerosols, BC, POC, and sea salt in accumulation and coarse modes are identical to the values used in the GEOS-Chem model for photolysis and heterogeneous chemistry calculations (Martin et al., 2003; Drury et al., 2010; Jaeglé et al., 2011). We assume that the log-normal distribution of SOA is identical to that of POC. The dry mass of aerosol type i (except dust) in each of WRF-GC's 4 size bins can be calculated as Eq. 3:

$$M_{i,j} = M_i \cdot \frac{\int_{l_{W,j}}^{h_{W,j}} m_i(\ln D_i)\, d\ln D_i}{\int_0^\infty m_i(\ln D_i)\, d\ln D_i} \tag{3}$$

where $l_{W,j}$ and $h_{W,j}$ are the lower and upper dry diameter bounds of the jth size bin. $M_{i,j}$ is the mass of aerosol type i in the jth bin, and M_i is the total mass of aerosol type i. The total number concentration of the internally-mixed aerosol population (N) cancels out in Eq. 3.

GEOS-Chem simulates dust mass concentrations in 4 internal size bins, which need to be redistributed into the 4 size bins used by WRF and WRF-GC (shown in Table 2). To achieve this, we ~~mimicked~~ mimick the redistribution scheme of dust aerosols in the Goddard Chemistry Aerosol Radiation Transport model (GOCART, Chin et al. (2002)), in which the first four

internal size bins are identical to those used in GEOS-Chem. In Eq. 4 and Eq. 5, the l and h with the subscripts W and G represent the lower and upper dry diameter bounds of each size bin used in WRF-GC and GEOS-Chem, respectively. The indices j and k refer to the size bins used by WRF-GC and GEOS-Chem, respectively ($j, k \in [1, 4]$). Eq. 4 calculates the fraction of dust mass within the GEOS-Chem size bin k that is mapped to the WRF-GC size bin j. The mass is distributed by the logarithmic of particle diameter. $diag\_dst(j)$, the total dust mass concentrations within the WRF-GC size bin j, is the sum of the dust mass mapped into that bin from the 4 GEOS-Chem dust size bins (Eq. 5).

$$dstfrac(j,k) = \frac{\max[\, 0, \, \min[\ln h_W(j), \ln h_G(k)] - \max[\ln l_W(j), \ln l_G(k)]\,]}{\ln h_G(k) - \ln l_G(k)} \tag{4}$$

$$diag\_dst(j) = \sum_{k=1}^{4} dst(k) \cdot dstfrac(j,k) \quad j, k \in [1, 4] \tag{5}$$

Eq. 6 diagnoses the number concentrations of the internally-mixed aerosols in each size bin. The total dry aerosol volume in the jth size bin ($\sum_{i=1}^{10} V_{d,i,j}$) is calculated by summing the dry aerosol volume of the 10 aerosol types. The aerosol number concentrations in the jth size bin, N_j, can then be diagnosed by dividing the total dry aerosol volume in that size bin by the mean particle size(Eq. 6). :

$$N_j = \frac{6}{\pi \left[\frac{1}{2}(l_W(j) + h_W(j))\right]^3} \cdot \sum_{i=1}^{10} V_{d,i,j} \tag{6}$$

3.2 Diagnosing water uptake of aerosols

The hygroscopic growth of aerosols at ambient relative humidity impacts their wet radii and optical properties. We follow the method developed by Petters and Kreidenweis (2007, 2013) to diagnose the uptake of water by aerosols and the resulting wet radii. According to the Zandovskii, Stoles, and Zdanovskii-Stokes-Robinson (ZSR) assumption (Stokes and Robinson, 1966), the total aerosol liquid water is equal to the sum of the water uptaken by each aerosol constituent, as shown in Eq. 7:

$$V_{w,j} = \frac{a_w}{1 - a_w} \sum_{i=1}^{10} \kappa_i V_{d,i,j} \tag{7}$$

where $V_{w,j}$ is the total volume of aerosol liquid water in the size bin j j^{th} size bin. a_w is the water activity, equal to the fractional relative humidity. κ_i is the hygroscopicity of the aerosol type i (Table 1). The wet radii radius of the internal-mixed aerosols in the jth size bin, $R_{w,j}$, are is required for the calculation of aerosol optical properties and are calculated by Eq. 8:

$$R_{w,j} = \frac{1}{2}\left(\frac{6}{\pi} \cdot \frac{V_{w,j} + \sum_{i=1}^{10} V_{d,i,j}}{N_j}\right)^{\frac{1}{3}} \tag{8}$$

3.3 Aerosol-radiation interactions

When ARI is turned on in WRF-GC v2.0, the new `optical_driver` module calls the `module_optical_averaging` to diagnose the bulk optical properties of the internally-mixed aerosols at each model grid and pass them to WRF for radiative transfer calculations. The diagnosed bulk optical properties include the AOD, the SSA, and the asymmetry factor at 4 specific wavelengths (300, 400, 600, 999 nm) for shortwave radiative transfer, and the AOD at 16 specific wavelengths for longwave radiative transfer. Our `module_optical_averaging` is developed by modifying a similar module from WRF-Chem (Fast et al., 2006). The `module_optical_averaging` module ingests the wet ~~radii~~ radius ($R_{w,j}$) and the number ~~concentrations~~ concentration (N_j) of aerosol particles in the jth size bin. The bulk refractive indices for the internally-mixed aerosols in each size bin are calculated by volume-weighting the refractive indices for individual aerosol species using a look-up table (Barnard et al., 2010). The tabulated refractive indices for water, sulfate, dust, sea salt, and primary and secondary OC are wavelength-dependent, while the refractive indices for other aerosol species do not vary with wavelength. The module then uses the bulk refractive indices to calculate the bulk extinction efficiency (Q_e), the bulk scattering efficiency (Q_s), and the intermediate asymmetry factor (g') for the internally-mixed aerosols as a function of the size parameter α_j ($= \frac{2\pi R_{w,j}}{\lambda}$) based on Mie theory (Wiscombe, 1979). We use a Chebyshev economization (Press et al., 1992) to avoid the full Mie calculation at each time step following Fast et al. (2006). A full Mie calculation is only performed at the first chemical time step to obtain the Chebyshev expansion coefficients for each complex refractive indices.

The bulk total extinction coefficient (b_{ext}) at wavelength λ is calculated as the sum of extinction by aerosols in all 4 size bins (Eq. 9):

$$b_{ext}(\lambda) = \sum_{j=1}^{4} Q_e(\alpha_j) \cdot \pi R_{w,j}^2 \cdot N_j \tag{9}$$

The bulk AOD in a layer of atmosphere of dz thickness is (Eq. 10):

$$\tau(\lambda) = b_{ext}(\lambda) \cdot dz \tag{10}$$

The single scattering albedo (ϖ_0), which represents the scattered percentage in the total light extinction of aerosol particles, is calculated as (Eq. 11):

$$\varpi_0(\lambda) = \frac{b_s(\lambda)}{b_{ext}(\lambda)} \tag{11}$$

where b_s is the scattering coefficient of aerosols, given by (Eq. 12):

$$b_s(\lambda) = \sum_{j=1}^{4} Q_s(\alpha_j) \cdot \pi R_{w,j}^2 \cdot N_j \tag{12}$$

The bulk asymmetry factor, g, represents the asymmetry between the forward scattering and backward scattering of aerosol particles:

$$g(\lambda) = \frac{\sum\limits_{j=1}^{4} Q_s(\alpha_j) \cdot \pi R_{w,j}^2 \cdot N_j \cdot g'(\alpha_j)}{b_s(\lambda)} \tag{13}$$

where g' is the intermediate asymmetry factor related to the size parameter α_j.

3.4 Aerosol-cloud interactions

We couple the activation of aerosol particles to the Morrison two-moment scheme (Morrison et al., 2009) and the Lin et al.
scheme (Lin et al., 1983; Chen and Sun, 2002) in WRF-GC. To achieve this, we develop an interface routine `wrfgc_mixactivate`
(contained in `module_mixactivate_wrappers` in the Coupler) by mimicking a similar routine in WRF-Chem. Eq. 14
shows the rate of change of the cloud droplet number concentration (N_c) within a WRF model grid in the two cloud micro-
physical schemes. The rate of change of N_c is determined by the advection of cloud droplet number ($-\mathbf{V} \bullet \nabla N_c$), the vertical
transport of cloud droplet number (D), the loss rate of cloud droplet number due to collision, coalescence, and collection (C),
the evaporation of cloud droplets (E), as well as the rate of cloud droplet activation (S).

$$\frac{\partial N_c}{\partial t} = -(\mathbf{V} \bullet \nabla N_c) + D - C - E + S \tag{14}$$

When ACI is turned on (`aer_cu_feedback=1` and `progn=1`) in WRF-GC, the `mixactivate_driver` module in
the WRF-GC Coupler calls the existing WRF subroutine `mixactivate` through an interface routine (`wrfgc_mixactivate`)
to calculate the number of aerosol particles activated into cloud droplets (S) and pass it to WRF. `wrfgc_mixactivate` first
calculates the volume-weighted bulk hygroscopocity using the diagnostic aerosol mass and number within each aerosol size
bin and then calls the subroutine `mixactivate`. The subroutine `mixactivate` uses the Köhler theory to calculate the acti-
vated aerosol mass and number when the ambient supersaturation is over the critical supersaturation of aerosols (Abdul-Razzak
and Ghan, 2000, 2002). The total aerosol mass and number concentrations are treated as two explicit population: interstitial
and cloud-borne. The prognostic aerosol mass and number concentrations are initialized as interstitial before passing to the
`mixactivate_driver` module. The activated aerosols will be then considered cloud-borne, while the unactivated aerosols
remain interstitial. The `mixactivate` subroutine also calculates CCN at six specified supersaturation ratios (0.02 %, 0.05
%, 0.1 %, 0.2 %, 0.5 %, and 1 %) as output diagnostics.

3.5 Development of nested-grid functionality and online lightning NO$_x$ emissions

We implement the nested-domain functionality into WRF-GC v2.0 to enable meteorology-chemistry simulations at higher
resolution. In WRF-GC v1.0 (Lin et al., 2020), the coupling between WRF and GEOS-Chem was limited to a single domain of
arbitrary dimension and resolution; the nesting of multiple model domains was not supported. This was because the modules
in the previous GEOS-Chem model versions (prior to v12.4.0) used a single memory space for the entire simulation, such that
the domain dimensions in GEOS-Chem were fixed once the simulation was initialized.

We improve the State Management Module in WRF-GC v2.0 to better control the memory space of GEOS-Chem. Figure 2
illustrates the operation of the state management module when running WRF-GC v2.0 in a nested-domain configuration. When
running a nested-domain simulation, WRF designates separate memory space for each domain, and at each time step WRF
alternately accesses the memory spaces for each domain. To achieve the same functionality in GEOS-Chem, we modify the

12

GEOS-Chem model (implemented in the standard code for v12.4.0 and after) so that all of its internal variables are saved into state objects (meteorology, chemistry, and diagnostic state variables), which are labeled for the specific simulation domain. We

365 then modify the State Management Module, such that at each time step during run-time, the State Management Module will determine the GEOS-Chem domain being processed, access the corresponding state objects, and provide them to GEOS-Chem. ~~In addition, the~~ The emission module of GEOS-Chem, ~~HEMCO, is recently updated (Keller et al., 2014; Lin et al., 2021), such that~~ the Harmonized Emissions Component (HEMCO), has also been updated to fully objectify its memory space ~~is also fully objectified~~ (Keller et al., 2014; Lin et al., 2021). This allows WRF-GC v2.0 to execute separate copies of HEMCO for each of

370 the nested domains.

WRF-GC v2.0 ~~also supports~~ allows both one-way and two-way information exchange between the nested domains, ~~as provided~~ supported by the WRF framework. In a nested-domain simulation, the outer (coarser) domain will always provide lateral boundary conditions to its immediate inner (finer) domain (one-way information exchange). ~~In addition, users can turn on~~ Users may also turn on the two-way information exchange option (`feedback=1` in the WRF-GC namelist), which further

375 allows information ~~from the inner domain~~ at the boundaries of the inner domain to be averaged and fed back to ~~to~~ the immediate outer domain at every time step.

In addition to the ~~existing~~ meteorology-dependent emissions ~~, we further implement online lightning NO_x emissions~~ in WRF-GC v1.0 (Lin et al., 2020), in WRF-GC v2.0 ~~by coupling~~ we further couple WRF meteorology to the online lightning NO_x emission scheme in the HEMCO module (Murray et al., 2012). Intra-cloud and cloud-to-ground flash densities are functions

380 of the cloud-top height and are calculated by the lightning parameterization in WRF (Price and Rind, 1992; Wong et al., 2013). HEMCO then calculates lightning NO_x emissions using the prescribed NO_x production rates (500 moles per flash for latitudes northward of $35°N$; 260 moles per flash elsewhere) (Murray et al., 2012) and vertically distributed them from the surface to the local convective cloud top level (Ott et al., 2010).

3.6 Computational performance of WRF-GC v2.0

385 We conduct two-day (June 27 to 29, 2019) simulations using the WRF-GC (v2.0) model and the GEOS-Chem Classic nested-grid model (v12.7.2), to compare their computational performance. Simulations with both models are configured with 245×181 atmospheric columns over China. The WRF-GC simulations have 50 vertical levels, while the GEOS-Chem Classic nested-grid simulation has 47 vertical levels. The WRF-GC model simulates meteorology online (2-min dynamical time step), while the GEOS-Chem Classic nested-grid simulation reads archived GEOS-FP assimilated meteorological dataset (https://gmao.gsfc.

390 nasa.gov/GMAO_products/) and calculates advection at 5-min time step. All simulations use the same emissions, the same chemical module (GEOS-Chem column model), and identical chemical time steps. All simulations are performed on the same single-node hardware with 24 Intel Cascade Lake physical cores, 100 GB of RAM, and a networked Lustre high-performance file system. WRF-GC uses MPI parallelization, while GEOS-Chem Classic uses OpenMP parallelization.

Table 3 compares the simulation wall times for the WRF-GC v2.0 model (with various chemical feedback options) and

395 for the GEOS-Chem Classic nested-grid model. Similar to our previous diagnosis (Lin et al., 2020), a one-way WRF-GC simulation (15282 s) is 53% faster than a similarly-configured GEOS-Chem Classic nested-grid simulation (33601 s). The

13

better computational performance of WRF-GC is due to its faster dynamic calculations and its more efficient parallelization of the chemical processes (Lin et al., 2020). The wall times for the two-way WRF-GC simulations with various combinations of chemical feedbacks (ARI only, ACI only, and both ARI and ACI) are all less than 11 % higher than the wall time for the one-way simulation. As expected, the slightly longer wall times in simulations with chemical feedbacks are mostly associated with the the extra calculations within the WRF-GC Coupler. The ARI calculations incur more wall time increases than the ACI calculations do. For reasons yet unclear, the wall time for the simulation with ARI only (17002 s) is slightly longer than that for the simulation with both ARI and ACI (16153 s). Nevertheless, in all WRF-GC simulations the coupling calculations are computationally economical and consume less than 9 % of the total wall times.

4   Validation of WRF-GC simulations of regional meteorology and surface pollutant concentrations over China

4.1   Setup of model experiments

We next evaluate WRF-GC's performance in simulating regional meteorology and surface pollutant concentrations. We conduct two control simulations with full aerosol-cloud-radiation interactions using WRF-GC v2.0, one during January 2015 (Case ~~Winter~~ACRw) and one during July 2016 (Case ~~Summer), to evaluate the model's performance in simulating surface PM~~$_{2.5}$ ~~and ozone concentrations, AOD, and cloud optical properties~~ACRs). Table 4 summarizes the setup of our simulations. Figure 3 ~~e~~ shows our simulation domain over East Asia, set by a Mercator projection at 27 km × 27 km spatial resolution. ~~The simulations are discretized vertically at~~ There are 50 ~~layers,~~ vertical layers extending from the surface to 10 hPa. ~~The Case Winter simulation was for~~ Case ACRw simulates January 4 to 29, ~~2015. The Case Summer simulation was for~~ 2015; Case ACRs simulates June 27 to July 31, 2016. The first four days of each simulation initialize the model. Meteorological initial conditions and boundary conditions (IC/BCs) are taken from the ~~NCEP~~ National Centers for Environmental Prediction (NCEP) FNL dataset (doi:10.5065/D6M043C6) at 1° resolution. Chemical IC/BCs are from a GEOS-Chem global simulation at 2.5° longitude × 2° latitude, interpolated to WRF-GC horizontal and vertical grids. ~~Both meteorological~~ Meteorological and chemical BCs are updated every 6 hours ~~in~~ at the WRF-GC ~~.~~ domain boundary. The WRF-GC simulations are not nudged with meteorological observations.

We further ~~design four~~ conduct sensitivity simulations over China for January 2015 and July 2016 with different combinations of ARI and ACI to investigate the impacts of chemical feedbacks on simulated meteorology and air quality (Table 4). The setup of these ~~four sensitivity simulations is identical to that of Case Summer~~ sensitivity simulations are identical to the control cases, except ARI and ACI are configured differently in each ~~of the sensitivity simulations~~ sensitivity simulation (Table 4). In ~~Case ACR, both ARI and ACI are turned on; this is identical to the Case Summer control simulation. In Case NO_ACR~~ Cases NO_ACRs and NO_ACRw, both ARI and ACI are turned off, i.e., ~~identical to a~~ one-way WRF-GC ~~simulation~~ simulations with no chemical feedbacks to meteorology. The ~~Case ARI and Case ACI sensitivity~~ Cases ARIs/ARIw and the Cases ACIs/ACIw simulations include either ~~only ARI or only~~ ARI or ACI, respectively. Our simulations are conducted at a typical meso-scale resolution (27 km), with the cumulus parameterization (new Tiedtke) and the cloud microphysical scheme (Morrison two-moment) both turned on. Thus, the sub-grid convective clouds do not explicitly respond to prognostic aerosol

14

information. This setup is typical of meso-scale simulations and have been shown to produce similar aerosol sensitivities as those simulated at cloud-resolving resolutions (Wu et al., 2011).

Chinese monthly mean anthropogenic emissions are from the Multi-resolution Emission Inventory for China (MEIC; Li et al. (2014)) ~~, which include emissions from power generation, industry, transportation, residential activities, and agriculture sectors at~~ with a resolution of $0.25°$ for the years 2015 and 2016. Anthropogenic emissions from the rest of Asia are from Li et al. (2017a), developed for the year 2010. Monthly mean biomass burning emissions are from the Global Emissions Database version 4 (GFED4; Randerson et al. (2018)). ~~Biogenic emissions are calculated online using the Model of Emissions of Gases and Aerosols from Nature (MEGAN; Guenther et al. (2012)), implemented in the HEMCO module (Keller et al., 2014) in GEOS-Chem. Other meteorology-dependent emissions,~~ Meteorology-dependent emissions, including the emissions of biogenic volatile organic compounds (Guenther et al., 2012), sea salt (Gong, 2003), dust (Zender et al., 2003), soil NO_x (Hudman et al., 2012), and lightning NO_x (Murray et al., 2012), are ~~also~~ calculated online in the HEMCO module (Keller et al., 2014) in GEOS-Chem.

4.2 Observation datasets

4.2.1 Satellite retrievals of AOD, cloud optical properties and surface downward shortwave radiation

We use satellite observations to evaluate WRF-GC's performance in simulating aerosol and cloud optical properties, and surface downward shortwave radiation. Monthly mean AOD observations are from the Deep Blue Level-3 monthly ~~and daily~~ aerosol products (AERDB_D3/M3_VIIRS_SNPP, version 1) from the Visible Infrared Imaging Radiometer Suite (VIIRS) instruments at ~~a spatial resolution of 1° (Sayer et al., 2018). Briefly, VIIRS is on board the Suomi National Polar-orbiting Partnership (SNPP) satellite, launched in 2011 with an Equator-overpassing time at 13:30 local time. VIIRS records data in 22 spectral bands at visible and thermal infrared wavebands. The monthly gridded products aggregate the 6-minute Level 2 swath data. Missing values of monthly mean AOD may be due to the obstruction by clouds, high reflectance by snow and ice, or sun glint.~~ $1°$ spatial resolution (Sayer et al., 2018). Monthly liquid cloud optical depth (LCOD) observations are from the VIIRS ~~/SNPP~~ Cloud Properties Level-3 monthly $1°$ grid products (CLDPROP_D3/M3_VIIRS_SNPP, version 1.1) (Platnick et al., 2019). ~~LCOD is retrieved from the non-absorbing visible, near-infrared or shortwave infrared channels of VIIRS using the bi-spectral solar reflectance algorithm (Nakajima et al., 1991). The Level-3 gridded products are also derived from the 6-minute Level-2 data.~~

~~We validate the~~ Monthly surface downward shortwave radiation ~~simulated by WRF-GC using the latest~~ observations for July 2016 are from the Earth Polychromatic Imaging Camera (EPIC)-derived products over land at $0.1°$ ~~spatial~~ resolution (Hao et al. (2020), https://doi.org/10.25584/1595069). ~~The EPIC instrument is on-board the Deep Space Climate Observatory (DSCOVR) satellite, launched in February 2015 to the Sun-Earth first Lagrange point (Burt and Smith, 2012). EPIC observes the sunlit part of the Earth at 10 spectral bands from the ultraviolet to near-infrared wavelengths every 1 to 2 hours; thus it is able to estimate the global downward shortwave radiation with high spatiotemporal resolution. The~~ The EPIC-derived total downward shortwave radiation is consistent with the ground-based observations with a low global bias of -0.71 Wm^{-2} over

land. ~~The spatiotemporal variations in the~~ For January 2015, due to the lack of EPIC-derived ~~surface downward shortwave radiation agrees well with the~~ products, we use the monthly gridded product from the Clouds and the Earth's Radiant Energy System ~~Synoptic~~ (CERES) ~~data~~ Edition 4.1 at 1° resolution (Rutan et al., 2015). The spatiotemporal variations of the surface downward shortwave radiation observed by the EPIC and CERES instruments are generally consistent (Hao et al., 2020).

4.2.2 Ground-based AOD ~~from Aerosol Robotic Network (AERONET) project~~ measurements

We evaluate the spectral AOD simulated by WRF-GC for January 2015 against the ground-based observations from the Aerosol Robotic Network ~~(AERONET). AERONET observes aerosol optical properties using the CIMEL Electronique multiband sun photometer~~ project (AERONET, https://aeronet.gsfc.nasa.gov/) (Version 3, Level 2.0 quality-assured dataset (Giles et al., 2019)). Holben et al. (1998) showed that the uncertainty of AERONET AOD under cloud-free condition was less than $\pm$ 0.01 for wavelengths over ~~than~~ 440 nm. We ~~use the Version 3, Level 2.0 quality-assured dataset (Giles et al., 2019), where the cloud-contaminated points and instrumental anomalies are removed. We~~ select four representative sites in Eastern China, where there are more than 50% of valid observations of spectral AOD at three wavelengths (500 nm, 675 nm, and 1020 nm) during January 2015. These four sites are: (1) Chinese Academy of Meteorological Sciences ~~(CAMS)~~ in Beijing (116.32°E, 39.93°N), (2) Xianghe (116.96°E, 39.75°N), (3) China University of Mining and Technology in Xuzhou (117.14°E, 34.22°N), and (4) Hong Kong Polytechnic University in Hong Kong (114.18°E, 22.30°N). ~~At each site, We calculate the daily mean of observed spectral AOD at each of the three wavelengths (500 , 675 , and 1020) in January 2015.~~

4.2.3 Surface measurements of air pollutants~~and~~ , air temperature, and planetary boundary layer height

Hourly surface measurements of $PM_{2.5}$ and ozone are managed by the Ministry of Ecology and Environment ~~(MEE)~~ of China (http://www.cnemc.cn). Our protocol for data quality control follows Jiang et al. (2020). We ~~remove~~ exclude sites with less than 90% valid hourly data during January 2015 and July 2016. ~~In model grids containing multiple sites, we select the site closest to the center of the~~ For comparison between observations and model results, we calculate the average $PM_{2.5}$ and ozone measurements in a WRF-GC grid. In all, we compare model results to summertime ozone observations at ~~581 sites and~~ 562 sites and to wintertime $PM_{2.5}$ ~~at 512~~ observations at 513 sites, respectively. Surface air temperature measurements ~~at 371 sites~~ over China are downloaded from the U.S. National Climate Data Center (https://gis.ncdc.noaa.gov/maps/ncei/cdo/hourly)~~. We remove the~~ , and we exclude sites with less than 90% valid data~~during July 2016.~~ . In all, surface air temperature measurements at 150 and 215 sites are used to evaluate our simulations during January 2015 and July 2016, respectively. Finally, Guo et al. (2016) analyzed the rawinsonde observations over China to determine the daily planetary boundary layer heights (PBLH) during January 2011 to July 2015. We use the ~~surface measurements at 215 sites to evaluate the simulated surface air temperature in July 2016.~~ observed PBLH at 120 sites at 08:00 and 20:00 local time (00:00 and 12:00 UTC, respectively) to validate the simulated PBLH in January 2015.

4.3 Validation of the simulated AOD over East Asia

Figure Figures 3a and 3c compare the AOD at 550 nm wavelength over East Asia as observed by VIIRS and as simulated by WRF-GC (Case WinterACRw) during January 8 to 28, 2015. For comparison against VIIRS observations, we use the simulated AODs at 300 nm and 999 nm to calculate the Ångström exponent of the internally-mixed bulk aerosol and then scale the interpolated the simulated AOD at 400 nm to obtain the simulated AOD at 550 nm. WRF-GC is generally able to reproduce the spatial distribution of AOD observed by VIIRS over Eastern China (105°E to 130°E, 20°N to 40°N) with a spatial correlation coefficient of r = 0.64. WRF-GC reproduces the high AOD values over the Sichuan Basin but underestimates the AOD over other parts of Eastern China. The observed and simulated AODs at 550 nm over Eastern China in January 2015 are 0.37 and 0.21, respectively. WRF-GC also underestimates the AOD over XinjiangProvince, , Qinghai, and Gansu provinces in Western China, likely reflecting an underestimation of dust.

Figure Figures 3b and 3d compare the observed and simulated (Case Summer) mean ACRs) AOD at 550 nm in during July 2016. VIIRS observes AOD values exceeding 0.6 over the NCP North China Plain (NCP) area, reflecting the large amounts of aerosols and their hygroscopic growth over that area. The simulated spatial distribution of AOD is generally consistent with that from VIIRS, but the peak values over the NCP are lower than the observations by 50%over the NCP. We also compare model results to the AOD observations from the MODIS instrument (Platnick et al., 2017) and similarly find that the simulated AODs are spatially consistent but lower than the MODIS observations over Eastern China.

Figure 4 compares the time series of the simulated daily spectral AOD against the AERONET observations at the four representative Chinese sites (Beijing, Xianghe, Xuzhou, and Hong Kong) during January 8 to 28, 2015. At each site, we compare interpolate the simulated spectral AODs at 550 400 nm, 600 nm, and 999 nm to the observed spectral AODs at wavelengths AERONET observation wavelengths of 500 nm, 675 nm, and 1020 nm, respectively, using the Ångström exponent method (Eck et al., 1999). WRF-GC reproduces the observed day-to-day variation of AOD at these four sites during January 2015. The temporal correlation coefficients between the observed and simulated AODs at all sites and wavelengths range between 0.55 and 0.87 (significant at 5 % significance level)0.86, except for the correlation coefficient between the observed and simulated AOD at 550 500 nm AOD in Beijing (0.44). However, the simulated AODs are consistently lower than the AERONET AODs, especially during high AOD events.

Our analyses above show that AODs simulated by WRF-GC reproduce the spatiotemporal variability of the AODs observed by satellite and ground-based networks. However, the simulated AOD are consistently lower than these observations. Previous comparisons of AODs simulated by regional models against satellite observations also often found spatial consistency but significant low biases in the model (Gao et al., 2014; Gan et al., 2015; Xing et al., 2015; Zhang et al., 2016). The reasons for this are yet unclear (Curci et al., 2015). The models (Gao et al., 2014; Gan et al., 2015; Xing et al., 2015; Zhang et al., 2016) . Curci et al. (2015) showed that the uncertainties for the model AODs are associated with the assumed mixing state, refractive indices, and hygroscopicity of aerosols. In particular, assumptions of the aerosol mixing state can lead to 30% to 35% uncertainty on the simulated AOD (Fassi-Fihri et al., 1997; Curci et al., 2015). In addition, the WRF-GC model may have underestimated the abundance of aerosols in the regional atmosphereover China, as indicated by the slight underestimation of surface PM$_{2.5}$ concentrations shown below (Figure 13). It is also possible that the model's internal mixing assumption leads to a large uncertainty of the AODs (Fassi-Fihri et al., 1997; Curci et al., 2015). Several Section 4.6). On the other hand, several

studies showed that the regional distributions of AOD observed by VIIRS and MODIS ~~were~~ are consistent with the AERONET measurements~~. However, ~~, but both VIIRS and MODIS observations ~~were generally biased-high~~ are high-biased compared to AERONET observations over Asia (Wang et al., 2020). This high-bias in the satellite-observed AOD may partially account for the discrepancy between the simulated and satellite AODs. The cause of the discrepancy between observed and simulated AOD should be further investigated in future studies.

4.4 Validation of the simulated LCOD and liquid cloud droplet effective radii

~~Figure~~ Figures 5a and 5b compare the July mean LCODs retrieved by VIIRS and ~~those~~ results from the Case ~~Summer (identical to Case ACR) simulation in~~ ACRs simulation for July 2016. The spatial distributions of observed and simulated LCOD are generally consistent ~~, with higher LCOD over land than over the ocean. Over land, the~~ over East Asia. The observed and simulated LCODs are both high over Northeastern China, ~~over~~ central-western China, and along the southern slopes of the Himalayas. ~~In contrast, the~~ The observed and simulated LCODs are relatively low over the Tibetan Plateau. The simulated domain-average LCOD from Case ~~Summer is 11.8~~ ACRs is 12.0 ± ~~8.5, in good agreement with~~ 8.1, lower than the domain-averaged LCOD retrieved by VIIRS (~~18.4~~ 18.2 ± ~~7.2~~ 7.5). The underestimation of simulated LCOD is mostly over Western China and the South China Sea~~and the Tibetan Plateau~~. Over Eastern China (eastward of 100 °E), the simulated magnitude and spatiotemporal patterns of LCOD are in good agreement with the observations (spatial correlation coefficient r = ~~0.61~~ 0.64, normalized mean bias = ~~-19.6~~ -25.3%). Figures 6a and 6b show the observed and simulated (Case ACRw) average LCODs during January 8 to 28, 2015. The model reproduces the spatial distribution of LCODs observed by VIIRS over China, including in particular the high LCODs over Southern China. However, the simulated LCOD is considerably lower than the VIIRS LCOD observations elsewhere in the domain.

Figure 7 shows the monthly mean liquid cloud effective radii at cloud top from the Case ~~Summer simulation(i. e., the Case ACR simulation).~~ ACRs simulation. Satellite retrievals of cloud effective radii often show large biases, except over areas dominated by liquid stratocumulus or stratus cloud (Yan et al., 2015; Witte et al., 2018). We instead compare the simulated liquid cloud effective radii to the reported values from aircraft observations over China. The observed effective radii of liquid cloud droplets over the NCP area in summer are in the range of 5.1 µm (± 2.2 µm) to 6.3 µm (± 2.3 µm) (Deng et al., 2009; Zhang et al., 2011b; Zhao et al., 2018). Over Southern China, the observed effective radii of liquid cloud droplets in summer vary from 7.3 ± 1.7 µm to 7.9 ± 3.0 µm (Hao et al., 2017; Yang et al., 2020). Our simulated effective radii of liquid cloud droplets are consistent with these observed sizes of liquid cloud droplets and reflect the spatial difference between Northern and Southern China. The simulated mean effective radii are 8.4 ± 1.3 µm and 10.7 ± 0.9 µm over the NCP and Southern China in July 2016, respectively.

4.5 Validation of simulated regional surface ~~downward shortwave radiation and surface air temperature over China~~ meteorology

~~Figure~~ Figures 8a and 8b compare the ~~July mean~~ surface downward shortwave radiation (SWDOWN) over East Asia from the EPIC-derived ~~data and those from the Case Summer simulation in~~ observations and those simulated by WRF-GC (Case ACRs)

in July 2016. The simulated spatial distribution of July mean SWDOWN is in good agreement with ~~that observed by EPIC over China~~the EPIC-derived observations over East Asia, with a spatial correlation coefficient r = 0.73. The ~~simulated monthly mean SWDOWN exceeded 300 over the Tibetan Plateau and Northwestern China but are approximately 200 over Southeastern China. The~~ observed and simulated July mean SWDOWN over China are ~~288.1 (288 $\pm$ 36.1) and 272.4 (~~36 W m^{-2} and 281 $\pm$ ~~47.6)~~48 W m^{-2}, respectively, with a slight low bias of ~~-5.4~~-2.4% in the model. Figures 9a and 9b compare the mean SWDOWN observed by CERES and that simulated by WRF-GC (Case ACRw) during January 8 to 28, 2015. The spatial distribution of the simulated wintertime SWDOWN also agrees well with the satellite observations, with a spatial correlation coefficient of 0.93 over the domain. The domain-average observed and simulated SWDOWN are 111 $\pm$ 45 W m^{-2} and 140 $\pm$ 55 W m^{-2}, respectively (model NMB = 25.9%). The overestimation of wintertime SWDOWN is over the Sichuan Basin, the Tibetan Plateau and the Southern China, possibly related to the model's underestimation of AOD and LCOD over these areas in winter.

~~Figure 10a shows~~ Figures 10a and Figure 11a show the good agreement between the simulated and observed surface air temperature ~~(Case Summer simulation) and the surface measurements over China in July 2016.~~ over China during July 2016 (Case ACRs) and during January 8 to 28, 2015 (Case ACRw), respectively. The spatial correlation ~~coefficient~~ coefficients between the observed and simulated surface air temperature ~~is~~are 0.92 (Case ACRs) and 0.93 (Case ACRw), respectively. During July 2016, the simulated and observed surface air temperature averaged over all sites are 23.7 $\pm$ 5.9 °C and 24.6 $\pm$ 5.0 °C, respectively (NMB of -3.7%). During January 8 to 28, ~~with a small~~ 2015, the simulated surface air temperature averaged over all sites is 7.2 $\pm$ 6.7 °C, with a model NMB of ~~-3.7% .~~-13.3 % relative to the observations.

Figure 12 compares the simulated (Case ACRw) mean PBLH at 20:00 local time to the rawinsonde observations over China during January 8 to 28, 2015. Lin et al. (2020) previously showed that, compared to the PBLH from the archived GEOS-FP reanalysis meteorology dataset, the wintertime PBLH simulated by WRF-GC better agreed with observations. This agreement is critical for the simulation of surface air quality, especially in winter (Wang et al., 2014a; Li et al., 2017b). The WRF-GC simulated PBLH at 20:00 local time over China during January 8 to 28, 2015 is 462 $\pm$ 176 m, in good agreement with the observed 448 $\pm$ 129 m. At 08:00 local time (not shown), the model underestimates the observed PBLH by 34% (simulated 281 $\pm$ 113 m versus observed 429 $\pm$ 94 m). Our validations above demonstrate the capability of the two-way coupled WRF-GC model (with ARI and ACI) in reproducing the regional meteorology.

4.6 Validation of simulated surface concentrations of PM$_{2.5}$ and ozone over China

We next assess WRF-GC's performance in simulating surface air pollutant concentrations over China in January 2015 and July 2016. We focus on wintertime PM$_{2.5}$ and summertime ozone, as they are the principle surface pollutants in China in winter and in summer, respectively. Figure 13a shows the observed and simulated (Case ~~Winter~~ACRw) PM$_{2.5}$ concentrations during January 8 to ~~January~~ 28, 2015. WRF-GC reproduces the observed spatial distributions of PM$_{2.5}$ over Eastern China (eastward of 108°E)~~in January 2015~~; the spatial correlation between the observed and simulated PM$_{2.5}$ concentrations is ~~0.74.~~ 0.77. The simulated mean PM$_{2.5}$ concentration over Eastern China (80.8 $\pm$ 32.6 μg m^{-3}) is 9.3 % lower than the observations (89.1 $\pm$ 31 μg m^{-3}). WRF-GC successfully captures the high PM$_{2.5}$ in Central China and over the Sichuan Basin ~~, but the model~~ but

19

underestimates the PM~~$^{2.5}$ concentrations in the North China Plain (NCP) and Northwestern China~~$_{2.5}$ concentrations over the NCP. ~~The simulated mean PM$_{2.5}$ concentration over Eastern China (87.5 ± 37.2) is 6.6% lower than the observations (93.7 ± 33)~~WRF-GC also underestimates PM$_{2.5}$ over Western China, likely reflecting a low-bias in the model dust, also seen in the simulated AODs. WRF-GC reproduces the temporal variation of hourly PM$_{2.5}$ during January 8 to 28, 2015. The temporal correlation coefficient between the observed and simulated hourly PM$_{2.5}$ averaged over all Chinese sites is 0.77.

Figure 13b compares the observed and simulated (Case ~~Summer~~ACRs) afternoon (13:00 to 17:00 local sun time) surface ozone concentrations over China during July 2016. ~~The simulated afternoon ozone concentrations are in good agreement with the surface measurements over China. The spatial correlation coefficient between the observed and simulated July surface ozone concentrations is 0.56 over Eastern China . The average observed and simulated ozone concentrations over Eastern China are 54 ± 13 and~~ WRF-GC reproduces the higher surface ozone concentrations over Northern and Central China, the relatively lower ozone concentrations near the South China coast, and the ozone hotspots over the megacity clusters (the Beijing-Tianjin-Hebin area, the Yantze River Delta area, and the Pearl River Delta area). However, the surface afternoon ozone concentrations simulated by WRF-GC (64 ± 17 ppbv~~, respectively~~) is high-biased compared to the observations (51 ± 13 ppbv). The normalized mean bias of the simulation is ~~19~~25.6 %. The overestimation of surface ozone concentrations is ~~mostly in the~~ most severe over Henan and Shanxi ~~Provinces over the NCP~~provinces in Northern China. The temporal correlation coefficient between the observed and simulated hourly afternoon ozone concentrations averaged over all sites is 0.67. Our analysis demonstrates WRF-GC's general capability in reproducing the spatial patterns and temporal variations of Chinese surface PM$_{2.5}$ and ozone in winter and in summer, respectively, particularly over the heavily polluted Eastern China.

5 Impacts of ARI and ACI on simulated meteorology and ~~surface ozone concentration~~ air quality in China~~in summer~~

5.1 Impacts of the ARI and ACI on ~~summertime~~ chemistry-sensitive meteorology

We examine the individual and combined impacts of ARI and ACI on the simulated ~~monthly mean LCOD, surface downward shortwave radiation, and surface air temperature in July 2016, respectively. Figure 5 d shows~~ regional meteorological conditions. Table 5 summarized the comparison of the monthly mean meteorological variables simulated by the sensitivity experiments and the observations. Figures 5 and 6 show the impacts of ARI and ACI on the simulated LCOD in July ~~2016. Without~~ 2016 and in January 2015, respectively. In both seasons, the simulated LCODs over Eastern China agree best with the VIIRS observations when ARI and ACI are both turned on (Cases ACRs and ACRw), compared to the sensitivity simulations when ARI or ACI, or both, are turned off (Table 5). In particular, we find that the inclusion of ACI greatly reduces the simulated LCOD in both seasons; the inclusion of ACI corrects the high-biased LCODs simulated by Cases NO_ACRs and NO_ACRw, ~~the model severely overestimates the VIIRS-observed LCOD over East Asia,~~ particularly over Central and Southern China, around Japan and Korea, and along the southern slopes of the Himalayas~~(Figure 5c). By turning on both ARI and ACI~~. In Cases ACRs and ACRw, the simulated ~~July mean LCOD decrease significantly over these areas and are in better agreement with the VIIRS observations. We further find that these improvements are mainly due to the inclusion of ACI (Figure 5e and 5f). By turning on the ACI , the simulated cloud water content and the simulated liquid cloud effective radii both decrease relative~~

~~to those in the NO_ACR simulation~~monthly mean CCN concentrations (at 0.1 % supersaturation) averaged from the cloud bottom to cloud top are 150 cm^{-3} and 58 cm^{-3}, respectively. However, when ACI is turned off, WRF-GC uses a constant, high CCN activation rate (250 cm^{-3} per time step), leading to overestimation of cloud droplet numbers (effectively around 250 cm^{-3}) and thus LCOD.

~~The shortwave extinction by aerosol and clouds affect the transfer of shortwave radiation to the surface. Figure 8d compares the simulated July mean SWDOWN from the cases ACR and NO_ACR. The combined impacts of ARI and ACI lead to increased simulated SWDOWN by 20 to 50 over Southwestern China and the Yangtze River Delta (YRD)area, while reducing the~~ Figures 8 and 9 show the impacts of ARI and ACI on the simulated SWDOWN ~~by~~ in July 2016 and January 2015, respectively. Again, the simulated SWDOWN over China are most consistent with EPIC-derived and CERES observations, in terms of magnitudes and spatial correlations, when both ARI and ACI are turned on (Table 5). In July, the individual impacts of ARI and ACI on the simulated SWDOWN are comparable in magnitude but spatially different. Turning on ARI (Case ARIs) leads to 10 to 50 W m^{-2} ~~over the NCP, the Sichuan Basin and the Bohai Sea. Including both~~ reductions in the simulated SWDOWN over Northern and Northeastern China, relative to the simulation where ARI and ACI ~~improves the spatial correlation coefficients from 0.57~~ are both turned off (Case NO_~~ACR)~~ACRs). Turning on ACI (Case ACIs) leads to 10 to ~~0.73 (Case ACR)~~ 50 W m^{-2} increases in the simulated SWDOWN over Western and Northeastern China and the Yangtze River Delta (YRD) area, as well as 10 to 30 W m^{-2} decreases in the simulated SWDOWN over ~~China. We found that these changes mostly reflect the impacts of ACI (Figure 8f) . The exceptions are over~~ the NCP and ~~Northeastern China, where the high values of AOD lead to a significant decrease in the simulated SWDOWN (Figure 3d and Figure 8e) when ARI is turned on~~Southern China. In January, the inclusion of ARI reduces the simulated SWDOWN over Eastern China by 8 to 40 W m^{-2}, while the inclusion of ACI does not significantly affect the simulated SWDOWN.

~~The~~ ARI and ACI also significantly affect the simulated surface air temperature. ~~Figure 10 c compares the simulated July~~ Figures 10 and 11 compare the simulated mean surface air temperature from the ~~cases ACR and NO_ACR. The combined impact of ARI and ACI lead to higher surface temperatures over Northeastern China, the YRD area, and around the Gulf of Bohai. In contrast,~~ sensitivity experiments during July 2016 and January 2015, respectively. Again, the inclusion of both ARI and ACI ~~combine to reduce the~~ leads to best agreement between the observed and simulated surface air temperature ~~over Central China. Figure 10b shows the overestimation of surface air temperature over Central China when the ARI and ACI are both turned off. Our sensitivity simulations indicate that these simulated changes are due~~ in both seasons (Table 5). In July, the inclusion of either ARI or ACI each leads to complex and spatially-varied responses ~~to either ARI or ACI (Figure~~ in surface air temperature (Figures 10d and 10e). In ~~addition, the~~ January, the impacts of ARI on surface air temperature are much stronger than the impacts of ACI. Upon closer inspection, we find that the simulated responses of surface air temperature to ARI and ACI are ~~not always consistent with~~ spatially similar to the simulated responses of SWDOWN, but with some exception. For example, over the Tibetan Plateau, the combination of ARI and ACI drives large increases in ~~surface downward solar radiation~~ SWDOWN but do not lead to much higher surface air temperature. This may be because the inclusion of ACI reduced the simulated LCOD over the Tibetan Plateau, which may have increased the downward shortwave radiation while decreasing the downward longwave radiation, thus partially neutralizing the changes in ~~radiative fluxes~~the local net radiative balance.

5.2 ~~Impacts of ARI and ACI on summertime afternoon surface ozone concentrations over China~~

665 ~~Figure 14 shows~~ The simulated PBLH are also chemically-sensitive, especially in winter. Figure 12 compare the simulated mean PBLH at 20:00 local time (12:00 UTC) from the sensitivity experiments during January 8 to 28, 2015. The simulated PBLH from Case ACRw (462 ± 176 m) better agrees with the observations (448 ± 129 m), compared to the simulated PBLH from Case NO_ACRw (491 ± 195 m). We find that the inclusion of ARI reduces the simulated PBLH through-out Eastern China, particularly over the Sichuan Basin. This response is consistent with previous studies that showed the

670 strong aerosol extinction in winter has a positive feedback to surface $PM_{2.5}$ concentration via the compression of PBLH (Li et al., 2017b; Zhang et al., 2018; Miao and Liu, 2019).

5.2 Impacts of ARI and ACI on simulated surface $PM_{2.5}$ over China in January 2015

Figures 14d,e,f show the combined and individual impacts of ARI and ACI on the simulated surface $PM_{2.5}$ concentrations during January 8 to 28, 2015, relative to the simulation when both ARI and ACI are turned off. Table 6 summarizes the

675 assessment of the simulated surface $PM_{2.5}$ concentrations against surface measurements. The inclusion of ARI significantly increases the simulated surface $PM_{2.5}$ concentrations by 6 μg m^{-3} to 15 μg m^{-3} over parts of Northern and Southern China, and the Sichuan Basin, thereby improving the agreement with surface observations (Table 6, model versus observation slope = 0.97 in Case ACRw and 0.9 in Case NO_ACRw, respectively).

Figures 12c,d,e show the combined and individual impacts of ARI and ACI on the simulated PBLH during January 8 to 28,

680 2015, relative to the simulation when both ARI and ACI are turned off. We find that the simulated response of surface $PM_{2.5}$ to ARI is spatially consistent with the simulated responses of SWDOWN, surface air temperature, and PBLH to ARI. Over the Sichuan Basin and parts of Northern and Central China, the strong aerosol extinction decrease the SWDOWN and surface air temperature, resulting in lower PBLH and a possibly more stable conditions within the PBL. The shallower and more stable PBL suppresses the dispersion of air pollutants, thus increasing surface $PM_{2.5}$ concentrations. These findings are consistent

685 with previous studies (Wang et al., 2014a; Li et al., 2017b; Zhang et al., 2018), although other feedback mechanisms may also play a role.

5.3 Impacts of ARI and ACI on simulated afternoon surface ozone over China in July 2016

Figures 14a,b,c show the combined and individual effects of the ARI and ACI on the simulated ~~monthly~~ mean surface afternoon ozone concentrations in July 2016, relative to the Case NO_~~ACR experiment. By turning on~~ ACRs experiment. Overall, the

690 inclusion of ARI and ACI in WRF-GC slightly reduces the model's positive bias in simulated surface ozone concentration (Table 6; model versus observation slope is 1.33 in Case ACRs and 1.38 in Case NO_ACRs, respectively). By including **both** ARI and ACI, the ~~July mean~~ simulated July afternoon surface ozone ~~concentrations significantly~~ concentration decrease by 2 to 10 ppbv over Henan Province~~and~~, the Sichuan Basin, and parts of Northeastern China. Over the YRD area and Eastern Inner Mongolia, ~~however,~~ turning on ARI and ACI leads to ~~increases of~~ increased afternoon surface ozone concentrations by up to

695   10 ppbv. These ~~varied responses~~ results are due to the spatially-varied responses of surface ozone to ARI and ACI, respectively ~~, which are not additive.~~ (Figure 14).

    We further diagnose the net chemical mass tendency of the simulated ozone in the boundary layer over China during July 2016, to elucidate the mechanisms by which ARI and ACI affect boundary-layer ozone. The net chemical mass tendency (unit: $kg\,s^{-1}$) is the net rate of change of boundary-layer ozone mass due to chemical production and loss processes over

700   each model grid, and its responses to ARI and ACI are shown in Figure 15. We find that the spatial responses of the net chemical mass tendency of ozone to ARI and ACI are very similar to the simulated responses of surface afternoon ozone, SWDOWN, and surface air temperature to these chemical feedbacks (Figures 8, 10, and 14). This indicates that ARI and ACI affect surface ozone mainly by modulating SWDOWN and surface air temperature, which in turn affect the emissions of biogenic isoprene and the subsequent chemical production of ozone in the boundary layer. For example, ARI lead to increased

705   surface air temperature over the YRD area, while both ARI and ACI lead to increased SWDOWN over that area. These meteorological responses lead to enhanced local biogenic ~~VOC~~ isoprene emissions and increased surface ozone. Over the ~~Eastern Inner Mongolia area, ACI lead to increased surface temperature and shortwave radiation, which significantly enhances the surface ozone concentration. Over the~~ Beijing-Tianjin-Hebei (BTH) area of China, where summertime ozone pollution is most severe (Lu et al., 2018), the ~~impacts~~ effects of ARI and ACI are complex. ~~Their combined effect is to increase surface~~

710   ~~ozone in the northern parts while decreasing surface ozone in the southern parts.~~

    ~~We compare the simulated monthly mean afternoon ozone concentrations from Case ACR and Case NO_ACR against the surface ozone measurements in China and over three megacities. Figure ?? shows the scatter plots of the observed and simulated monthly mean surface afternoon ozone concentrations over China (581 sites), in the BTH area (32 sites),in the Pearl River Delta (PRD)area (20 sites), and in the YRD area (32 sites) during July 2016. The simulated monthly mean~~

715   ~~afternoon ozone concentrations from Case ACR and Case NO_ACR are 22 % and 28 % higher than the observations over China, respectively. The improvement in simulated surface ozone due to the overall effects of the ARI and ACI is more evident over the three megacities. Including both~~ ARI and ACI both reduce the local SWDOWN (Figures 8e,f), while ARI increases surface air temperature over southern BTH and ACI suppresses surface air temperature over the entire BTH (Figures 10d,e). The combined effect of chemical feedbacks is to increase surface ozone over northern BTH, while decreasing surface ozone

720   over southern BTH. ARI and ACI ~~in WRF-GC leads to smaller biases in the statistics between simulated and observed surface ozoneconcentrations in all three megacities. The slopes of simulated versus observed ozone concentrations improve from 1.58 to 1.39 in the BTH and from 1.43 to 1.24 in the PRD. The slope of simulated versus observed ozone concentrations in the YRD do not change, but the intercept is reduced from -7.3 to -2.5 .~~ may also modulate other meteorological variable to affect surface ozone, and such possibilities warrants further investigation.

6 Conclusions

725

We present ~~here version 2.0 of the~~ WRF-GC ~~model~~v2.0, an online two-way coupling of the WRF meteorological model and the GEOS-Chem chemical model~~with aerosol-radiation interactions and aerosol-cloud interactions, as well as the~~ , with aerosol

feedback to radiation and cloud microphysics and nested-domain capability. The coupling structure of WRF-GC v2.0 is abstracted and modular, which allows the two parent models to be updated independently and stay state-of-the-science. ~~The~~

730 ~~chemical module from GEOS-Chem is benchmarked, well-documented, evaluated, and actively developed by research groups worldwide. New developments in GEOS-Chem can be easily incorporated into WRF-GC under its modular architecture.~~ In addition, all WRF-GC v2.0 features can be parallelized using MPI, which allow the model to ~~scale~~ be computationally efficient and scalable to massively-parallel architectures. WRF-GC v2.0 enables GEOS-Chem users to investigate the interactions between meteorology and atmospheric chemistry for any region at a wide range of spatial resolutions. At the same time, WRF-GC

735 offers other regional modellers access to the GEOS-Chem chemical core.

We implement the ARI and ACI into WRF-GC v2.0 by adding three modules with the following functions: (1) diagnosing the size and number of the bulk aerosols simulated by GEOS-Chem, (2) computing aerosol optical properties, and (3) computing the number of aerosol particles activated into cloud droplets. The aerosol optical properties and cloud droplet number source are then passed to the WRF model for radiative transfer and cloud microphysics calculations. We develop WRF-GC'~~se~~s nested-

740 domain capability by improving the ~~state management module~~ State Management Module and the memory-management in GEOS-Chem (implemented as of GEOS-Chem version 12.4.0). The nested-domain capability enables WRF-GC simulations at higher spatial resolution~~simulations while being computationally efficient~~.

Our test simulations show that the WRF-GC model with the ~~full~~ aerosol-cloud-radiation interactions is able to reproduce the spatial distributions of wintertime surface PM$_{2.5}$ and summertime surface ozone with small biases compared with

745 the ~~surface measurements~~observations. WRF-GC v2.0 also generally reproduces the spatial distributions of ~~monthly mean AOD compared with the satellite-based retrievals by VIIRS. The day-to-day variation of AOD is in good agreement with the ground-based observations from AERONET over four sites in eastern China during January 2015. Coupling the cloud droplet activation to aerosol masses simulated by GEOS-Chem improves the simulated July mean liquid cloud optical depth and liquid cloud effective radii to better agree with VIIRS and aircraft observations. In China and in three Chinese megacities currently

750 experiencing severe surface ozone pollution (BTH, PRD,~~ regional AOD and ~~YRD)~~LCOD, SWDOWN, surface air temperature, and PBLH. Moreover, the inclusion of both ARI and ACI ~~also leads to improved simulated surface ozone concentrations~~ leads to best agreement of simulated regional meteorology and surface air pollutant concentrations against observations, relative to ~~the simulation without ARI and ACI~~sensitivity experiments where the chemical feedbacks are partially or completely excluded. We diagnose the response of wintertime surface PM$_{2.5}$ to ARI through modulation of surface air temperature and PBLH, as

755 well as the response of summertime surface afternoon ozone to through modulation of radiation and temperature. ARI and ACI may also affect other meteorological variables to alter air quality; such possibilities may be further investigated using WRF-GC.

WRF-GC (v2.0) is the first coupling of GEOS-Chem to an open-source meteorological model with chemical feedbacks. The modules developed for WRF-GC v2.0 can also facilitate future two-way couplings between GEOS-Chem and other dynamical

760 models. Supports for the size-resolved aerosol schemes (APM and TOMAS) in WRF-GC are currently under development, which will better represent aerosol microphysics. We envision WRF-GC to become a powerful tool for research, forecast, and regulatory applications of regional atmospheric chemistry and air quality.

References

Abdul-Razzak, H. and Ghan, S.: A parameterization of aerosol activation 2. Multiple aerosol types, J. Geophys. Res. Atmos., 105, 6837–6844, https://doi.org/10.1029/1999JD901161, 2000.

Abdul-Razzak, H. and Ghan, S.: A parameterization of aerosol activation 3. Sectional representation, J. Geophys. Res. Atmos., 107, https://doi.org/10.1029/2001JD000483, 2002.

Abel, D., Holloway, T., Kladar, R. M., Meier, P., Ahl, D., Harkey, M., and Patz, J.: Response of Power Plant Emissions to Ambient Temperature in the Eastern United States, Environ. Sci. Technol., 51, 5838–5846, https://doi.org/10.1021/acs.est.6b06201, 2017.

Archer-Nicholls, S., Lowe, D., Schultz, D. M., and McFiggans, G.: Aerosol-radiation-cloud interactions in a regional coupled model: the effects of convective parameterisation and resolution, Atmos. Chem. Phys., 16, 5573–5594, https://doi.org/10.5194/acp-16-5573-2016, 2016.

Baklanov, A., Schluenzen, K., Suppan, P., Baldasano, J., Brunner, D., Aksoyoglu, S., Carmichael, G., Douros, J., Flemming, J., Forkel, R., Galmarini, S., Gauss, M., Grell, G., Hirtl, M., Joffre, S., Jorba, O., Kaas, E., Kaasik, M., Kallos, G., Kong, X., Korsholm, U., Kurganskiy, A., Kushta, J., Lohmann, U., Mahura, A., Manders-Groot, A., Maurizi, A., Moussiopoulos, N., Rao, S. T., Savage, N., Seigneur, C., Sokhi, R. S., Solazzo, E., Solomos, S., Sorensen, B., Tsegas, G., Vignati, E., Vogel, B., and Zhang, Y.: Online coupled regional meteorology chemistry models in Europe: current status and prospects, Atmos. Chem. Phys., 14, 317–398, https://doi.org/10.5194/acp-14-317-2014, 2014.

Barnard, J. C., Fast, J. D., Paredes-Miranda, G., Arnott, W. P., and Laskin, A.: Technical Note: Evaluation of the WRF-Chem "Aerosol Chemical to Aerosol Optical Properties" Module using data from the MILAGRO campaign, Atmos. Chem. Phys., 10, 7325–7340, https://doi.org/10.5194/acp-10-7325-2010, 2010.

Bey, I., Jacob, D. J., Yantosca, R. M., Logan, J. A., Field, B. D., Fiore, A. M., Li, Q., Liu, H. Y., Mickley, L. J., and Schultz, M. G.: Global modeling of tropospheric chemistry with assimilated meteorology: Model description and evaluation, J. Geophys. Res. Atmos., 106, 23 073–23 095, https://doi.org/10.1029/2001JD000807, 2001.

Burt, J. and Smith, B.: Deep space climate observatory: The DSCOVR mission, 2012 IEEE Aerospace Conference, Big Sky, MT, USA, 3–10 March 2012, 2012.

Byun, D. and Schere, K. L.: Review of the governing equations, computational algorithms, and other components of the Models-3 Community Multiscale Air Quality (CMAQ) modeling system, Appl. Mech. Rev., 59, 51–77, https://doi.org/10.1115/1.2128636, 2006.

Chapman, E. G., Gustafson Jr., W. I., Easter, R. C., Barnard, J. C., Ghan, S. J., Pekour, M. S., and Fast, J. D.: Coupling aerosol-cloud-radiative processes in the WRF-Chem model: Investigating the radiative impact of elevated point sources, Atmos. Chem. Phys., 9, 945–964, https://doi.org/10.5194/acp-9-945-2009, 2009.

Chen, F. and Dudhia, J.: Coupling an advanced land surface-hydrology model with the Penn State-NCAR MM5 modeling system. Part I: Model implementation and sensitivity, Mon. Weather Rev., 129, 569–585, https://doi.org/10.1175/1520-0493(2001)129<0569:CAALSH>2.0.CO;2, 2001a.

Chen, F. and Dudhia, J.: Coupling an advanced land surface-hydrology model with the Penn State-NCAR MM5 modeling system. Part II: Preliminary model validation, Mon. Weather Rev., 129, 587–604, https://doi.org/10.1175/1520-0493(2001)129<0587:CAALSH>2.0.CO;2, 2001b.

Chen, S. and Sun, W.: A One-dimensional Time Dependent Cloud Model, J. Meteorol. Soc. Jap. Ser. II, 80, 99–118, https://doi.org/10.2151/jmsj.80.99, 2002.

Chin, M., Ginoux, P., Kinne, S., Torres, O., Holben, B., Duncan, B., Martin, R., Logan, J., Higurashi, A., and Nakajima, T.: Tropospheric aerosol optical thickness from the GOCART model and comparisons with satellite and Sun photometer measurements, J. Atmos. Sci., 59, 461–483, https://doi.org/10.1175/1520-0469(2002)059<0461:TAOTFT>2.0.CO;2, 2002.

Chou, M. D. and Suarez, M. J.: An efficient thermal infrared radiation parameterization for use in general circulation models, NASA Tech. Memo., 104506, 3, 85pp, 1994.

Curci, G., Hogrefe, C., Bianconi, R., Im, U., Balzarini, A., Baró, R., Brunner, D., Forkel, R., Giordano, L., Hirtl, M., Honzak, L., Jiménez-Guerrero, P., Knote, C., Langer, M., Makar, P., Pirovano, G., Pérez, J., San José, R., Syrakov, D., Tuccella, P., Werhahn, J., Wolke, R., Žabkar, R., Zhang, J., and Galmarini, S.: Uncertainties of simulated aerosol optical properties induced by assumptions on aerosol physical and chemical properties: An AQMEII-2 perspective, Atmos. Environ., 115, 541 – 552, https://doi.org/10.1016/j.atmosenv.2014.09.009, 2015.

Deng, Z., Zhao, C., Zhang, Q., Huang, M., and Ma, X.: Statistical analysis of microphysical properties and the parameterization of effective radius of warm clouds in Beijing area, Atmos. Res., 93, 888–896, https://doi.org/10.1016/j.atmosres.2009.04.011, 2009.

Ding, A. J., Fu, C. B., Yang, X. Q., Sun, J. N., Petäjä, T., Kerminen, V.-M., Wang, T., Xie, Y., Herrmann, E., Zheng, L. F., Nie, W., Liu, Q., Wei, X. L., and Kulmala, M.: Intense atmospheric pollution modifies weather: a case of mixed biomass burning with fossil fuel combustion pollution in eastern China, Atmos. Chem. Phys., 13, 10 545–10 554, https://doi.org/10.5194/acp-13-10545-2013, 2013.

Drury, E., Jacob, D. J., Spurr, R. J. D., Wang, J., Shinozuka, Y., Anderson, B. E., Clarke, A. D., Dibb, J., McNaughton, C., and Weber, R.: Synthesis of satellite (MODIS), aircraft (ICARTT), and surface (IMPROVE, EPA-AQS, AERONET) aerosol observations over eastern North America to improve MODIS aerosol retrievals and constrain surface aerosol concentrations and sources, J. Geophys. Res. Atmos., 115, https://doi.org/10.1029/2009JD012629, 2010.

Eastham, S. D., Weisenstein, D. K., and Barrett, S. R.: Development and evaluation of the unified tropospheric–stratospheric chemistry extension (UCX) for the global chemistry-transport model GEOS-Chem, Atmos. Environ., 89, 52–63, https://doi.org/10.1016/j.atmosenv.2014.02.001, 2014.

Eastham, S. D., Long, M. S., Keller, C. A., Lundgren, E., Yantosca, R. M., Zhuang, J., Li, C., Lee, C. J., Yannetti, M., Auer, B. M., Clune, T. L., Kouatchou, J., Putman, W. M., Thompson, M. A., Trayanov, A. L., Molod, A. M., Martin, R. V., and Jacob, D. J.: GEOS-Chem High Performance (GCHP v11-02c): a next-generation implementation of the GEOS-Chem chemical transport model for massively parallel applications, Geosci. Model. Dev., 11, 2941–2953, https://doi.org/10.5194/gmd-11-2941-2018, 2018.

Eck, T., Holben, B., Reid, J., Dubovik, O., Smirnov, A., O'Neill, N., Slutsker, I., and Kinne, S.: Wavelength dependence of the optical depth of biomass burning, urban, and desert dust aerosols, J. Geophys. Res. Atmos., 104, 31 333–31 349, https://doi.org/10.1029/1999JD900923, 1999.

Fairlie, T. D., Jacob, D. J., and Park, R. J.: The impact of transpacific transport of mineral dust in the United States, Atmos. Environ., 41, 1251–1266, https://doi.org/10.1016/j.atmosenv.2006.09.048, 2007.

Fassi-Fihri, A., Suhre, K., and Rosset, R.: Internal and external mixing in atmospheric aerosols by coagulation: Impact on the optical and hygroscopic properties of the sulphate-soot system, Atmos. Environ., 31, 1393 – 1402, https://doi.org/10.1016/S1352-2310(96)00341-X, 1997.

Fast, J. D., Gustafson Jr., W. I., Easter, R. C., Zaveri, R. A., Barnard, J. C., Chapman, E. G., Grell, G. A., and Peckham, S. E.: Evolution of ozone, particulates, and aerosol direct radiative forcing in the vicinity of Houston using a fully coupled meteorology-chemistry-aerosol model, J. Geophys. Res. Atmos., 111, https://doi.org/10.1029/2005JD006721, 2006.

860 Flemming, J., Inness, A., Flentje, H., Huijnen, V., Moinat, P., Schultz, M. G., and Stein, O.: Coupling global chemistry transport models to ECMWF's integrated forecast system, Geosci. Model. Dev., 2, 253–265, https://doi.org/10.5194/gmd-2-253-2009, 2009.

Forkel, R., Werhahn, J., Hansen, A. B., McKeen, S., Peckham, S., Grell, G., and Suppan, P.: Effect of aerosol-radiation feedback on regional air quality - A case study with WRF/Chem, Atmos. Environ., 53, 202–211, https://doi.org/10.1016/j.atmosenv.2011.10.009, 2012.

Fountoukis, C. and Nenes, A.: ISORROPIA II: a computationally efficient thermodynamic equilibrium model for K^+- Ca^{2+}- Mg^{2+}- NH_4^+-
865 Na^+- SO_4^{2-}- NO_3^-- Cl^-- H_2O aerosols, Atmos. Chem. Phys., 7, 4639–4659, https://doi.org/10.5194/acp-7-4639-2007, 2007.

Gan, C. M., Pleim, J., Mathur, R., Hogrefe, C., Long, C. N., Xing, J., Wong, D., Gilliam, R., and Wei, C.: Assessment of long-term WRF–CMAQ simulations for understanding direct aerosol effects on radiation "brightening" in the United States, Atmos. Chem. Phys., 15, 12 193–12 209, https://doi.org/10.5194/acp-15-12193-2015, 2015.

Gao, Y., Zhao, C., Liu, X., Zhang, M., and Leung, L. R.: WRF-Chem simulations of aerosols and anthropogenic aerosol radiative forcing in
870 East Asia, Atmos. Environ., 92, 250–266, https://doi.org/10.1016/j.atmosenv.2014.04.038, 2014.

Giles, D. M., Sinyuk, A., Sorokin, M. G., Schafer, J. S., Smirnov, A., Slutsker, I., Eck, T. F., Holben, B. N., Lewis, J. R., Campbell, J. R., Welton, E. J., Korkin, S. V., and Lyapustin, A. I.: Advancements in the Aerosol Robotic Network (AERONET) Version 3 database – automated near-real-time quality control algorithm with improved cloud screening for Sun photometer aerosol optical depth (AOD) measurements, Atmos. Meas. Tech., 12, 169–209, https://doi.org/10.5194/amt-12-169-2019, 2019.

875 Gong, S. L.: A parameterization of sea-salt aerosol source function for sub-and super-micron particles, Global Biogeochem. Cy., 17, https://doi.org/10.1029/2003GB002079, 2003.

Gong, W., Makar, P. A., Zhang, J., Milbrandt, J., Gravel, S., Hayden, K. L., Macdonald, A. M., and Leaitch, W. R.: Modelling aerosol-cloud-meteorology interaction: A case study with a fully coupled air quality model (GEM-MACH), Atmos. Environ., 115, 695–715, https://doi.org/10.1016/j.atmosenv.2015.05.062, 2015.

880 Grell, G. A. and Freitas, S. R.: A scale and aerosol aware stochastic convective parameterization for weather and air quality modeling, Atmos. Chem. Phys., 14, 5233–5250, https://doi.org/10.5194/acp-14-5233-2014, 2014.

Grell, G. A., Peckham, S. E., Schmitz, R., McKeen, S. A., Frost, G., Skamarock, W. C., and Eder, B.: Fully coupled "online" chemistry within the WRF model, Atmos. Environ., 39, 6957–6975, https://doi.org/10.1016/j.atmosenv.2005.04.027, 2005.

Guenther, A. B., Jiang, X., Heald, C. L., Sakulyanontvittaya, T., Duhl, T., Emmons, L. K., and Wang, X.: The Model of Emissions of Gases
885 and Aerosols from Nature version 2.1 (MEGAN2.1): an extended and upYeard framework for modeling biogenic emissions, Geosci. Model. Dev., 5, 1471–1492, https://doi.org/10.5194/gmd-5-1471-2012, 2012.

Guo, J., Miao, Y., Zhang, Y., Liu, H., Li, Z., Zhang, W., He, J., Lou, M., Yan, Y., Bian, L., and Zhai, P.: The climatology of planetary boundary layer height in China derived from radiosonde and reanalysis data, Atmos. Chem. Phys., 16, 13 309–13 319, https://doi.org/10.5194/acp-16-13309-2016, 2016.

890 Hansen, J., Sato, M., and Ruedy, R.: Radiative forcing and climate response, J. Geophys. Res., 102, 6831–6864, https://doi.org/10.1029/96JD03436, 1997.

Hao, D., Asrar, G. R., Zeng, Y., Zhu, Q., Wen, J., Xiao, Q., and Chen, M.: DSCOVR/EPIC-derived global hourly and daily downward shortwave and photosynthetically active radiation data at $0.1° \times 0.1°$ resolution, Earth Syst. Sci. Data, 12, 2209–2221, https://doi.org/10.5194/essd-12-2209-2020, 2020.

895 Hao, J., Yin, Y., Kuang, X., Chen, J., Yuan, L., Xiao, H., Li, Z., Pu, M., Wang, J., Zhou, X., Chen, Y., and Wu, Y.: Aircraft Measurements of the Aerosol Spatial Distribution and Relation with Clouds over Eastern China, Aerosol Air. Qual. Res., 17, 3230–3243, https://doi.org/10.4209/aaqr.2016.12.0576, 2017.

Haywood, J. and Boucher, O.: Estimates of the direct and indirect radiative forcing due to tropospheric aerosols: A review, Rev. Geophys., 38, 513–543, https://doi.org/10.1029/1999RG000078, 2000.

900 Holben, B., Eck, T., Slutsker, I., Tanre, D., Buis, J., Setzer, A., Vermote, E., Reagan, J., Kaufman, Y., Nakajima, T., Lavenu, F., Jankowiak, I., and Smirnov, A.: AERONET - A federated instrument network and data archive for aerosol characterization, Remote Sens. Environ., 66, 1–16, https://doi.org/10.1016/S0034-4257(98)00031-5, 1998.

Hong, S.-Y., Noh, Y., and Dudhia, J.: A New Vertical Diffusion Package with an Explicit Treatment of Entrainment Processes, Mon. Weather Rev., 134, 2318–2341, https://doi.org/10.1175/MWR3199.1, 2006.

905 Hu, L., Keller, C. A., Long, M. S., Sherwen, T., Auer, B., Da Silva, A., Nielsen, J. E., Pawson, S., Thompson, M. A., Trayanov, A. L., Travis, K. R., Grange, S. K., Evans, M. J., and Jacob, D. J.: Global simulation of tropospheric chemistry at 12.5 km resolution: performance and evaluation of the GEOS-Chem chemical module (v10-1) within the NASA GEOS Earth system model (GEOS-5 ESM), Geosci. Model Dev., 11, 4603–4620, https://doi.org/10.5194/gmd-11-4603-2018, 2018.

Huang, X., Ding, A., Liu, L., Liu, Q., Ding, K., Niu, X., Nie, W., Xu, Z., Chi, X., Wang, M., Sun, J., Guo, W., and Fu, C.: Effects of
910 aerosol-radiation interaction on precipitation during biomass-burning season in East China, Atmos. Chem. Phys., 16, 10 063–10 082, https://doi.org/10.5194/acp-16-10063-2016, 2016.

Hudman, R. C., Moore, N. E., Mebust, A. K., Martin, R. V., Russell, A. R., Valin, L. C., and Cohen, R. C.: Steps towards a mechanistic model of global soil nitric oxide emissions: implementation and space based-constraints, Atmos. Chem. Phys., 12, 7779–7795, https://doi.org/10.5194/acp-12-7779-2012, 2012.

915 Iacono, M. J., Delamere, J. S., Mlawer, E. J., Shephard, M. W., Clough, S. A., and Collins, W. D.: Radiative forcing by long-lived greenhouse gases: Calculations with the AER radiative transfer models, J. Geophys. Res. Atmos., 113, https://doi.org/10.1029/2008JD009944, 2008.

Jaeglé, L., Quinn, P. K., Bates, T. S., Alexander, B., and Lin, J.-T.: Global distribution of sea salt aerosols: new constraints from in situ and remote sensing observations, Atmos. Chem. Phys., 11, 3137–3157, https://doi.org/10.5194/acp-11-3137-2011, 2011.

Jaeglé, L., Shah, V., Thornton, J. A., Lopez-Hilfiker, F. D., Lee, B. H., McDuffie, E. E., Fibiger, D., Brown, S. S., Veres, P., Sparks, T. L.,
920 Ebben, C. J., Wooldridge, P. J., Kenagy, H. S., Cohen, R. C., Weinheimer, A. J., Campos, T. L., Montzka, D. D., Digangi, J. P., Wolfe, G. M., Hanisco, T., Schroder, J. C., Campuzano-Jost, P., Day, D. A., Jimenez, J. L., Sullivan, A. P., Guo, H., and Weber, R. J.: Nitrogen Oxides Emissions, Chemistry, Deposition, and Export Over the Northeast United States During the WINTER Aircraft Campaign, J. Geophys. Res. Atmos., 123, 12 368–12 393, https://doi.org/10.1029/2018JD029133, 2018.

Jiang, Z., Jolleys, M. D., Fu, T.-M., Palmer, P. I., Ma, Y. P., Tian, H., Li, J., and Yang, X.: Spatiotemporal and probability variations of surface
925 PM2.5 over China between 2013 and 2019 and the associated changes in health risks: An integrative observation and model analysis, Sci. Total. Environ., 723, 137 896, https://doi.org/10.1016/j.scitotenv.2020.137896, 2020.

Jimenez, P. A., Dudhia, J., Gonzalez-Rouco, J. F., Navarro, J., Montavez, J. P., and Garcia-Bustamante, E.: A Revised Scheme for the WRF Surface Layer Formulation, Mon. Weather Rev., 140, 898–918, https://doi.org/10.1175/MWR-D-11-00056.1, 2012.

Johnson, B., Shine, K., and Forster, P.: The semi-direct aerosol effect: Impact of absorbing aerosols on marine stratocumulus, Q. J. Roy.
930 Meteor. Soc., 130, 1407–1422, https://doi.org/10.1256/qj.03.61, 2004.

Kaminski, J. W., Neary, L., Struzewska, J., McConnell, J. C., Lupu, A., Jarosz, J., Toyota, K., Gong, S. L., Côté, J., Liu, X., Chance, K., and Richter, A.: GEM-AQ, an on-line global multiscale chemical weather modelling system: model description and evaluation of gas phase chemistry processes, Atmos. Chem. Phys., 8, 3255–3281, https://doi.org/10.5194/acp-8-3255-2008, 2008.

Keller, C. A., Long, M. S., Yantosca, R. M., Da Silva, A. M., Pawson, S., and Jacob, D. J.: HEMCO v1.0: a versatile, ESMF-compliant component for calculating emissions in atmospheric models, Geosci. Model Dev., 7, 1409–1417, https://doi.org/10.5194/gmd-7-1409-2014, 2014.

Kim, P. S., Jacob, D. J., Fisher, J. A., Travis, K., Yu, K., Zhu, L., Yantosca, R. M., Sulprizio, M. P., Jimenez, J. L., Campuzano-Jost, P., Froyd, K. D., Liao, J., Hair, J. W., Fenn, M. A., Butler, C. F., Wagner, N. L., Gordon, T. D., Welti, A., Wennberg, P. O., Crounse, J. D., St. Clair, J. M., Teng, A. P., Millet, D. B., Schwarz, J. P., Markovic, M. Z., and Perring, A. E.: Sources, seasonality, and trends of southeast US aerosol: an integrated analysis of surface, aircraft, and satellite observations with the GEOS-Chem chemical transport model, Atmos. Chem. Phys., 15, 10 411–10 433, https://doi.org/10.5194/acp-15-10411-2015, 2015.

Kodros, J. and Pierce, J.: Important global and regional differences in aerosol cloud-albedo effect estimates between simulations with and without prognostic aerosol microphysics, J. Geophys. Res. Atmos., 122, 4003–4018, https://doi.org/10.1002/2016JD025886, 2017.

Köpke, P., Hess, M., Schult, I., and Shettle, E. P.: Global aerosol data set, report, Max-Planck Inst. für Meteorol., Hamburg, Germany,, 1997.

Latimer, R. N. C. and Martin, R. V.: Interpretation of measured aerosol mass scattering efficiency over North America using a chemical transport model, Atmos. Chem. Phys., 19, 2635–2653, https://doi.org/10.5194/acp-19-2635-2019, 2019.

Li, M., Zhang, Q., Streets, D. G., He, K. B., Cheng, Y. F., Emmons, L. K., Huo, H., Kang, S. C., Lu, Z., Shao, M., Su, H., Yu, X., and Zhang, Y.: Mapping Asian anthropogenic emissions of non-methane volatile organic compounds to multiple chemical mechanisms, Atmos. Chem. Phys., 14, 5617–5638, https://doi.org/10.5194/acp-14-5617-2014, 2014.

Li, M., Zhang, Q., Kurokawa, J.-i., Woo, J.-H., He, K., Lu, Z., Ohara, T., Song, Y., Streets, D. G., Carmichael, G. R., Cheng, Y., Hong, C., Huo, H., Jiang, X., Kang, S., Liu, F., Su, H., and Zheng, B.: MIX: a mosaic Asian anthropogenic emission inventory under the international collaboration framework of the MICS-Asia and HTAP, Atmos. Chem. Phys., 17, 935–963, https://doi.org/10.5194/acp-17-935-2017, 2017a.

Li, Z., Xia, X., Cribb, M., Mi, W., Holben, B., Wang, P., Chen, H., Tsay, S.-C., Eck, T. F., Zhao, F., Dutton, E. G., and Dickerson, R. R.: Aerosol optical properties and their radiative effects in northern China, J. Geophys. Res., 112, https://doi.org/10.1029/2006JD007382, 2007.

Li, Z., Guo, J., Ding, A., Liao, H., Liu, J., Sun, Y., Wang, T., Xue, H., Zhang, H., and Zhu, B.: Aerosol and boundary-layer interactions and impact on air quality, Natl. Sci. Rev., 4, 810–833, https://doi.org/10.1093/nsr/nwx117, 2017b.

Lin, H., Feng, X., Fu, T.-M., Tian, H., Ma, Y., Zhang, L., Jacob, D. J., Yantosca, R. M., Sulprizio, M. P., Lundgren, E. W., Zhuang, J., Zhang, Q., Lu, X., Zhang, L., Shen, L., Guo, J., Eastham, S. D., and Keller, C. A.: WRF-GC (v1.0): online coupling of WRF (v3.9.1.1) and GEOS-Chem (v12.2.1) for regional atmospheric chemistry modeling – Part 1: Description of the one-way model, Geosci. Model Dev., 13, 3241–3265, https://doi.org/10.5194/gmd-13-3241-2020, 2020.

Lin, H., Jacob, D. J., Lundgren, E. W., Sulprizio, M. P., Keller, C. A., Fritz, T. M., Eastham, S. D., Emmons, L. K., Campbell, P. C., Baker, B., Saylor, R. D., and Montuoro, R.: Harmonized Emissions Component (HEMCO) 3.0 as a versatile emissions component for atmospheric models: application in the GEOS-Chem, NASA GEOS, WRF-GC, CESM2, NOAA GEFS-Aerosol, and NOAA UFS models, Geosci. Model Dev. Discuss., 2021, 1–26, https://doi.org/10.5194/gmd-2021-130, https://gmd.copernicus.org/preprints/gmd-2021-130/, 2021.

Lin, Y. L., Farley, R. D., and Orville, H. D.: Bulk Parameterization of The Snow Field in A Cloud Model, Journal of Climate and Applied Meteorology, 22, 1065–1092, https://doi.org/10.1175/1520-0450(1983)022<1065:BPOTSF>2.0.CO;2, 1983.

Lohmann, U. and Feichter, J.: Global indirect aerosol effects: a review, Atmos. Chem. Phys., 5, 715–737, https://doi.org/10.5194/acp-5-715-2005, 2005.

Long, M. S., Yantosca, R., Nielsen, J. E., Keller, C. A., da Silva, A., Sulprizio, M. P., Pawson, S., and Jacob, D. J.: Development of a grid-independent GEOS-Chem chemical transport model (v9-02) as an atmospheric chemistry module for Earth system models, Geosci. Model Dev., 8, 595–602, https://doi.org/10.5194/gmd-8-595-2015, 2015.

Lu, X., Hong, J., Zhang, L., Cooper, O. R., Schultz, M. G., Xu, X., Wang, T., Gao, M., Zhao, Y., and Zhang, Y.: Severe Surface Ozone Pollution in China: A Global Perspective, Environ. Sci. Technol. Lett., 5, 487–494, https://doi.org/10.1021/acs.estlett.8b00366, 2018.

Lu, X., Zhang, L., Wu, T., Long, M. S., Wang, J., Jacob, D. J., Zhang, F., Zhang, J., Eastham, S. D., Hu, L., Zhu, L., Liu, X., and Wei, M.: Development of the global atmospheric chemistry general circulation model BCC-GEOS-Chem v1.0: model description and evaluation, Geosci. Model Dev., 13, 3817–3838, https://doi.org/10.5194/gmd-13-3817-2020, 2020.

Ma, Y., Fu, T. M., Tian, H., Gao, J., Hu, M., Guo, J., Zhang, Y., Sun, Y., Zhang, L., Yang, X., and Wang, X.: Emergency Response Measures to Alleviate a Severe Haze Pollution Event in Northern China during December 2015: Assessment of Effectiveness, Aerosol Air Qual. Res., 20, https://doi.org/10.4209/aaqr.2019.09.0442, 2020.

Marais, E. A., Jacob, D. J., Jimenez, J. L., Campuzano-Jost, P., Day, D. A., Hu, W., Krechmer, J., Zhu, L., Kim, P. S., Miller, C. C., Fisher, J. A., Travis, K., Yu, K., Hanisco, T. F., Wolfe, G. M., Arkinson, H. L., Pye, H. O. T., Froyd, K. D., Liao, J., and McNeill, V. F.: Aqueous-phase mechanism for secondary organic aerosol formation from isoprene: application to the southeast United States and co-benefit of SO2 emission controls, Atmos. Chem. Phys., 16, 1603–1618, https://doi.org/10.5194/acp-16-1603-2016, 2016.

Martin, R. V., Jacob, D. J., Yantosca, R. M., Chin, M., and Ginoux, P.: Global and regional decreases in tropospheric oxidants from photochemical effects of aerosols, J. Geophys. Res. Atmos., 108, 4097, https://doi.org/10.1029/2002JD002622, 2003.

Miao, R., Chen, Q., Zheng, Y., Cheng, X., Sun, Y., Palmer, P. I., Shrivastava, M., Guo, J., Zhang, Q., Liu, Y., Tan, Z., Ma, X., Chen, S., Zeng, L., Lu, K., and Zhang, Y.: Model bias in simulating major chemical components of $PM_{2.5}$ in China, Atmos. Chem. Phys., 20, 12 265–12 284, https://doi.org/10.5194/acp-20-12265-2020, 2020.

Miao, Y. and Liu, S.: Linkages between aerosol pollution and planetary boundary layer structure in China, Sci. Total. Environ., 650, 288–296, https://doi.org/10.1016/j.scitotenv.2018.09.032, 2019.

Morrison, H., Thompson, G., and Tatarskii, V.: Impact of Cloud Microphysics on the Development of Trailing Stratiform Precipitation in a Simulated Squall Line: Comparison of One- and Two-Moment Schemes, Mon. Weather Rev., 137, 991–1007, https://doi.org/10.1175/2008MWR2556.1, 2009.

Murray, L. T., Jacob, D. J., Logan, J. A., Hudman, R. C., and Koshak, W. J.: Optimized regional and interannual variability of lightning in a global chemical transport model constrained by LIS/OTD satellite data, J. Geophys. Res. Atmos., 117, https://doi.org/10.1029/2012JD017934, 2012.

Nakajima, T., King, M. D., Spinhirne, J. D., and Radke, L. F.: Determination of the Optical Thickness and Effective Particle Radius of Clouds from Reflected Solar Radiation Measurements. Part I: Theory, Nature, 517, 41.e1–41.e21, 1991.

Nakanishi, M. and Niino, H.: An improved mellor-yamada level-3 model: Its numerical stability and application to a regional prediction of advection fog, Bound.-Lay. Meteorol., 119, 397–407, https://doi.org/10.1007/s10546-005-9030-8, 2006.

Ott, L. E., Pickering, K. E., Stenchikov, G. L., Allen, D. J., DeCaria, A. J., Ridley, B., Lin, R.-F., Lang, S., and Tao, W.-K.: Production of lightning NOx and its vertical distribution calculated from three-dimensional cloud-scale chemical transport model simulations, J. Geophys. Res. Atmos., 115, https://doi.org/10.1029/2009JD011880, 2010.

Pai, S. J., Heald, C. L., Pierce, J. R., Farina, S. C., Marais, E. A., Jimenez, J. L., Campuzano-Jost, P., Nault, B. A., Middlebrook, A. M., Coe, H., Shilling, J. E., Bahreini, R., Dingle, J. H., and Vu, K.: An evaluation of global organic aerosol schemes using airborne observations, Atmos. Chem. Phys., 20, 2637–2665, https://doi.org/10.5194/acp-20-2637-2020, 2020.

Petaja, T., Jarvi, L., Kerminen, V. M., Ding, A. J., Sun, J. N., Nie, W., Kujansuu, J., Virkkula, A., Yang, X. Q., Fu, C. B., Zilitinkevich, S., and Kulmala, M.: Enhanced air pollution via aerosol-boundary layer feedback in China, Sci. Rep., 6, https://doi.org/10.1038/srep18998, 2016.

Petters, M. D. and Kreidenweis, S. M.: A single parameter representation of hygroscopic growth and cloud condensation nucleus activity, Atmos. Chem. Phys., 7, 1961–1971, https://doi.org/10.5194/acp-7-1961-2007, 2007.

Petters, M. D. and Kreidenweis, S. M.: A single parameter representation of hygroscopic growth and cloud condensation nucleus activity - Part 3: Including surfactant partitioning, Atmos. Chem. Phys., 13, 1081–1091, https://doi.org/10.5194/acp-13-1081-2013, 2013.

Philip, S., Martin, R. V., Pierce, J. R., Jimenez, J. L., Zhang, Q., Canagaratna, M. R., Spracklen, D. V., Nowlan, C. R., Lamsal, L. N., Cooper, M. J., and Krotkov, N. A.: Spatially and seasonally resolved estimate of the ratio of organic mass to organic carbon, Atmos. Environ., 87, 34–40, https://doi.org/10.1016/j.atmosenv.2013.11.065, 2014.

Platnick, S., King, M., and Hubanks, P.: MODIS Atmosphere L3 Monthly Product. NASA MODIS Adaptive Processing System, Goddard Space Flight Center, USA, http://dx.doi.org/10.5067/MODIS/MOD08_M3.061;http://dx.doi.org/10.5067/MODIS/MYD08_M3.061, 2017.

Platnick, S., Meyer, K. G., Hubanks, P., Holz, R., Ackerman, S. A., and Heidinger, A. K.: VIIRS Atmosphere L3 Cloud Properties Product. Version-1.1. NASA Level-1 and Atmosphere Archive and Distribution System (LAADS) Distributed Active Archive Center (DAAC), Goddard Space Flight Center, USA, http://dx.doi.org/10.5067/VIIRS/CLDPROP_M3_VIIRS_SNPP.011, 2019.

Press, W. H., Teukolsky, S. A., and Flannery, B. P.: Numerical Recipes., Cambridge Univ. Press, New York, 1992.

Price, C. and Rind, D.: A Simple Lightning Parameterization for Calculating Global Lightning Distributions, J. Geophys. Res. Atmos., 97, 9919–9933, https://doi.org/10.1029/92JD00719, 1992.

Pye, H. O. T., Chan, A. W. H., Barkley, M. P., and Seinfeld, J. H.: Global modeling of organic aerosol: the importance of reactive nitrogen (NO_x and NO_3), Atmos. Chem. Phys., 10, 11 261–11 276, https://doi.org/10.5194/acp-10-11261-2010, 2010.

Randerson, J., G.R., v. d. W., L., G., G.J., C., and P.S., K.: Global Fire Emissions Database, Version 4, (GFEDv4). ORNL DAAC, Oak Ridge, Tennessee, USA., https://doi.org/10.3334/ORNLDAAC/1293, 2018.

Renner, E. and Wolke, R.: Modelling the formation and atmospheric transport of secondary inorganic aerosols with special attention to regions with high ammonia emissions, Atmos. Environ., 44, 1904 – 1912, https://doi.org/10.1016/j.atmosenv.2010.02.018, 2010.

Robinson, A. L., Donahue, N. M., Shrivastava, M. K., Weitkamp, E. A., Sage, A. M., Grieshop, A. P., Lane, T. E., Pierce, J. R., and Pandis, S. N.: Rethinking organic aerosols: Semivolatile emissions and photochemical aging, Science, 315, 1259–1262, https://doi.org/10.1126/science.1133061, 2007.

Rutan, D. A., Kato, S., Doelling, D. R., Rose, F. G., Nguyen, L. T., Caldwell, T. E., and Loeb, N. G.: CERES Synoptic Product: Methodology and Validation of Surface Radiant Flux, J Atmos. Ocean. Tech., 32, 1121–1143, https://doi.org/10.1175/JTECH-D-14-00165.1, 2015.

Sayer, A. M., Hsu, N. C., Lee, J., Bettenhausen, C., Kim, W. V., and Smirnov, A.: Satellite Ocean Aerosol Retrieval (SOAR) Algorithm Extension to S-NPP VIIRS as Part of the "Deep Blue" Aerosol Project, J. Geophys. Res. Atmos, 123, 380–400, https://doi.org/10.1002/2017JD027412, 2018.

Skamarock, W. C., Klemp, J. B., Dudhia, J., Gill, D. O., Liu, Z., Berner, J., and Huang, X.: NCAR Tech. Note NCAR/TN-556+STR: A Description of the Advanced Research WRF Model Version 4, https://doi.org/10.5065/1dfh-6p97, 2019.

Skamarock, W. C. et al.: NCAR Tech. Note NCAR/TN-475+STR: A Description of the Advanced Research WRF Model Version 3, https://doi.org/10.5065/D68S4MVH, 2008.

Stokes, R. H. and Robinson, R. A.: Interactions in Aqueous Nonelectrolyte Solutions. I. Solute-Solvent Equilibria, J. Phys. Chem., 70, 2126–2131, https://doi.org/10.1021/j100879a010, 1966.

Tao, Z., Yu, H., and Chin, M.: The Role of Aerosol-Cloud-Radiation Interactions in Regional Air Quality-A NU-WRF Study over the United States, Atmosphere, 6, 1045–1068, https://doi.org/10.3390/atmos6081045, 2015.

Tegen, I., Hollrig, P., Chin, M., Fung, I., Jacob, D., and Penner, J.: Contribution of different aerosol species to the global aerosol extinction optical thickness: Estimates from model results, J. Geophys. Res. Atmos., 102, 23 895–23 915, https://doi.org/10.1029/97JD01864, 1997.

Tiedtke, M.: A comprehensive mass flux scheme for cumulus parameterization in large-scale models, Mon. Weather. Rev., 117, 1779–1800, https://doi.org/10.1175/1520-0493(1989)117<1779:ACMFSF>2.0.CO;2, 1989.

Wang, J., Wang, S., Jiang, J., Ding, A., Zheng, M., Zhao, B., Wong, D. C., Zhou, W., Zheng, G., Wang, L., Pleim, J. E., and Hao, J.: Impact of aerosol-meteorology interactions on fine particle pollution during China's severe haze episode in January 2013, Environ. Res. Lett., 9, https://doi.org/10.1088/1748-9326/9/9/094002, 2014a.

Wang, Q., Jacob, D. J., Spackman, J. R., Perring, A. E., Schwarz, J. P., Moteki, N., Marais, E. A., Ge, C., Wang, J., and Barrett, S. R. H.: Global budget and radiative forcing of black carbon aerosol: Constraints from pole-to-pole (HIPPO) observations across the Pacific, J. Geophys. Res. Atmos., 119, 195–206, https://doi.org/10.1002/2013JD020824, 2014b.

Wang, Y., Yuan, Q., Shen, H., Zheng, L., and Zhang, L.: Investigating multiple aerosol optical depth products from MODIS and VIIRS over Asia: Evaluation, comparison, and merging, Atmos. Environ., 230, 117 548, https://doi.org/10.1016/j.atmosenv.2020.117548, 2020.

Wicker, L. J. and Skamarock, W. C.: Time-Splitting Methods for Elastic Models Using Forward Time Schemes, Mon. Weather Rev., 130, 2088 – 2097, https://doi.org/10.1175/1520-0493(2002)130<2088:TSMFEM>2.0.CO;2, 2002.

Wiscombe, W. J.: NCAR Tech. Note, TN-140+STR: Mie scattering calculations: Advances in technique and fast, vector-speed computer codes, 1979.

Witte, M. K., Yuan, T., Chuang, P. Y., Platnick, S., Meyer, K. G., Wind, G., and Jonsson, H. H.: MODIS Retrievals of Cloud Effective Radius in Marine Stratocumulus Exhibit No Significant Bias, Geophys. Res. Lett., 45, 10,656–10,664, https://doi.org/10.1029/2018GL079325, 2018.

Wolke, R., Knoth, O., Hellmuth, O., Schröder, W., and Renner, E.: The parallel model system LM-MUSCAT for chemistry-transport simulations: Coupling scheme, parallelization and applications, Adv. Par. Com., 13, 363–369, https://doi.org/10.1016/S0927-5452(04)80048-0, 2004.

Wong, D. C., Pleim, J., Mathur, R., Binkowski, F., Otte, T., Gilliam, R., Pouliot, G., Xiu, A., Young, J. O., and Kang, D.: WRF-CMAQ two-way coupled system with aerosol feedback: software development and preliminary results, Geosci. Model. Dev., 5, 299–312, https://doi.org/10.5194/gmd-5-299-2012, 2012.

Wong, J., Barth, M. C., and Noone, D.: Evaluating a lightning parameterization based on cloud-top height for mesoscale numerical model simulations, Geosci. Model Dev., 6, 429–443, https://doi.org/10.5194/gmd-6-429-2013, 2013.

Wu, L., Su, H., and Jiang, J. H.: Regional simulations of deep convection and biomass burning over South America: 2. Biomass burning aerosol effects on clouds and precipitation, J. Geophys. Res. Atmos., 116, https://doi.org/10.1029/2011JD016106, 2011.

Xing, J., Mathur, R., Pleim, J., Hogrefe, C., Gan, C.-M., Wong, D. C., Wei, C., and Wang, J.: Air pollution and climate response to aerosol direct radiative effects: A modeling study of decadal trends across the northern hemisphere, J. Geophys. Res. Atmos., 120, 12,221–12,236, https://doi.org/10.1002/2015JD023933, 2015.

Yan, H., Huang, J., Minnis, P., Yi, Y., Sun-Mack, S., Wang, T., and Nakajima, T. Y.: Comparison of CERES-MODIS cloud microphysical properties with surface observations over Loess Plateau, J. Quant. Spectrosc. Ra., 153, 65–76, https://doi.org/10.1016/j.jqsrt.2014.09.009, 2015.

1085 Yang, J., Li, J., Li, P., Sun, G., Cai, Z., Yang, X., Cui, C., Dong, X., Xi, B., Wan, R., Wang, B., and Zhou, Z.: Spatial Distribution and Impacts of Aerosols on Clouds Under Meiyu Frontal Weather Background Over Central China Based on Aircraft Observations, J. Geophys. Res. Atmos., 125, e2019JD031 915, https://doi.org/10.1029/2019JD031915, 2020.

Yu, F. and Luo, G.: Simulation of particle size distribution with a global aerosol model: contribution of nucleation to aerosol and CCN number concentrations, Atmos. Chem. Phys., 9, 7691–7710, https://doi.org/10.5194/acp-9-7691-2009, 2009.

1090 Yu, S., Mathur, R., Pleim, J., Wong, D., Gilliam, R., Alapaty, K., Zhao, C., and Liu, X.: Aerosol indirect effect on the grid-scale clouds in the two-way coupled WRF-CMAQ: model description, development, evaluation and regional analysis, Atmos. Chem. Phys., 14, 11 247–11 285, https://doi.org/10.5194/acp-14-11247-2014, 2014.

Zaveri, R. A., Easter, R. C., Fast, J. D., and Peters, L. K.: Model for Simulating Aerosol Interactions and Chemistry (MOSAIC), J. Geophys. Res. Atmos., 113, https://doi.org/10.1029/2007JD008782, 2008.

1095 Zender, C. S., Bian, H., and Newman, D.: Mineral Dust Entrainment and Deposition (DEAD) model: Description and 1990s dust climatology, J. Geophys. Res. Atmos., 108, https://doi.org/10.1029/2002JD002775, 2003.

Zhang, C. and Wang, Y.: Projected future changes of tropical cyclone activity over the western North and South Pacific in a 20-km-Mesh regional climate model, J. Climate, 30, 5923–5941, https://doi.org/10.1175/JCLI-D-16-0597.1, 2017.

Zhang, C., Wang, Y., and Hamilton, K.: Improved representation of boundary layer clouds over the southeast Pacific in ARW-WRF using a
1100 modified Tiedtke cumulus parameterization scheme, Mon. Weather Rev., 139, 3489–3513, https://doi.org/10.1175/MWR-D-10-05091.1, 2011a.

Zhang, Q., Quan, J., Tie, X., Huang, M., and Ma, X.: Impact of aerosol particles on cloud formation: Aircraft measurements in China, Atmos. Environ., 45, 665–672, https://doi.org/10.1016/j.atmosenv.2010.10.025, 2011b.

Zhang, X., Zhang, Q., Hong, C., Zheng, Y., Geng, G., Tong, D., Zhang, Y., and Zhang, X.: Enhancement of PM2.5 Concentrations by
1105 Aerosol-Meteorology Interactions Over China, J. Geophys. Res. Atmos., 123, 1179–1194, https://doi.org/10.1002/2017JD027524, 2018.

Zhang, Y.: Online-coupled meteorology and chemistry models: history, current status, and outlook, Atmos. Chem. Phys., 8, 2895–2932, https://doi.org/10.5194/acp-8-2895-2008, 2008.

Zhang, Y., Wen, X.-Y., and Jang, C.: Simulating chemistry–aerosol–cloud–radiation–climate feedbacks over the continental U.S. using the online-coupled Weather Research Forecasting Model with chemistry (WRF/Chem), Atmos. Environ., 44, 3568 – 3582,
1110 https://doi.org/10.1016/j.atmosenv.2010.05.056, 2010.

Zhang, Y., Mao, H., Ding, A., Zhou, D., and Fu, C.: Impact of synoptic weather patterns on spatio-temporal variation in surface O-3 levels in Hong Kong during 1999-2011, Atmos. Environ., 73, 41–50, https://doi.org/10.1016/j.atmosenv.2013.02.047, 2013.

Zhang, Y., Zhang, X., Wang, L., Zhang, Q., Duan, F., and He, K.: Application of WRF/Chem over East Asia: Part I. Model evaluation and intercomparison with MM5/CMAQ, Atmos. Environ., 124, 285–300, https://doi.org/10.1016/j.atmosenv.2015.07.022, 2016.

1115 Zhao, B., Liou, K.-N., Gu, Y., Li, Q., Jiang, J. H., Su, H., He, C., Tseng, H.-L. R., Wang, S., Liu, R., Qi, L., Lee, W.-L., and Hao, J.: Enhanced PM2.5 pollution in China due to aerosol-cloud interactions, Sci. Rep., 7, https://doi.org/10.1038/s41598-017-04096-8, 2017.

Zhao, C., Qiu, Y., Dong, X., Wang, Z., Peng, Y., Li, B., Wu, Z., and Wang, Y.: Negative Aerosol-Cloud r(e) Relationship From Aircraft Observations Over Hebei, China, Earth and Space Science, 5, 19–29, https://doi.org/10.1002/2017EA000346, 2018.

Zheng, G. J., Duan, F. K., Su, H., Ma, Y. L., Cheng, Y., Zheng, B., Zhang, Q., Huang, T., Kimoto, T., Chang, D., Poeschl, U., Cheng, Y. F.,
1120   and He, K. B.: Exploring the severe winter haze in Beijing: the impact of synoptic weather, regional transport and heterogeneous reactions,
Atmos. Chem. Phys., 15, 2969–2983, https://doi.org/10.5194/acp-15-2969-2015, 2015.
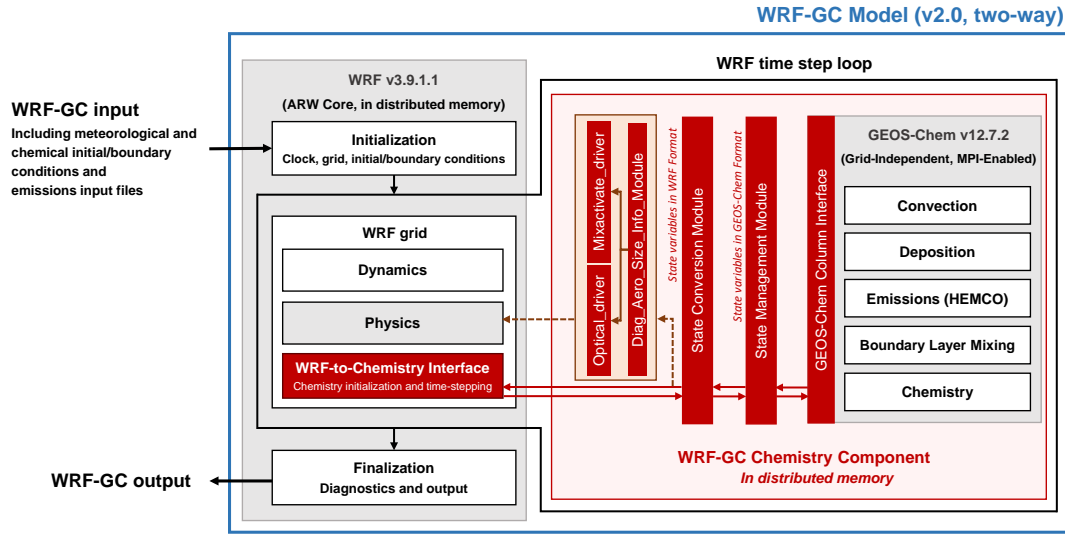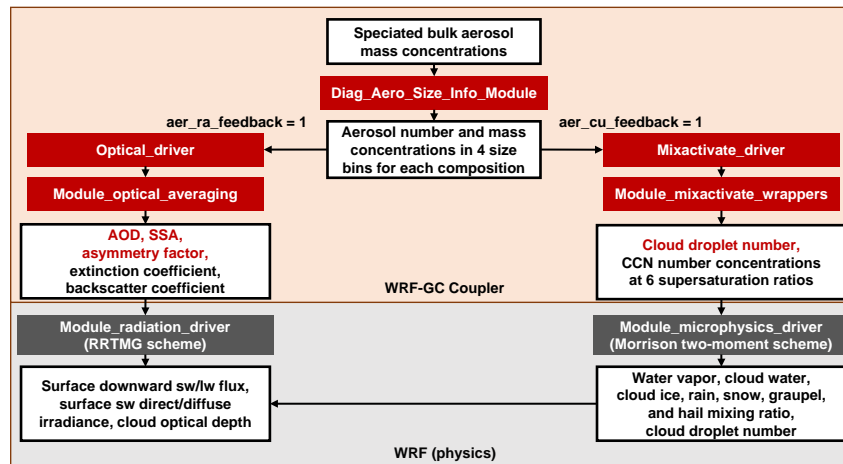
Figure 1. (a) Architectural overview of the WRF-GC coupled model (v2.0). The WRF-GC Coupler (all parts shown in red) includes interfaces to the two parent models, as well as the two-way coupling modules (shown in orange). The parent models (shown in grey) are standard codes downloaded from their sources, without any modifications. (b) Flow diagram of the aerosol-radiation and aerosol-cloud interactions in the WRF-GC coupled model (v2.0).
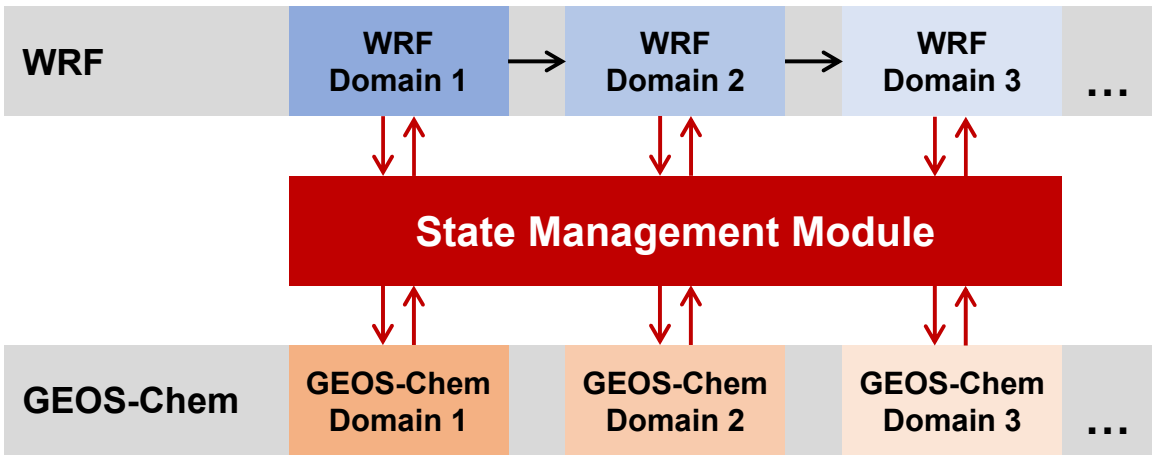
Figure 2. Illustration of the WRF-GC State Management Module operating in a nested-domain configuration.
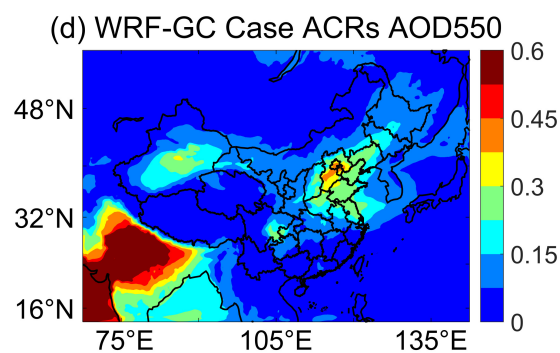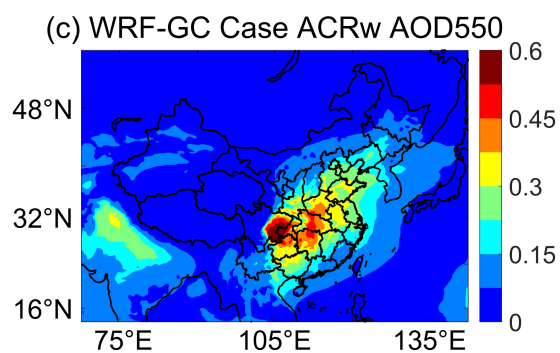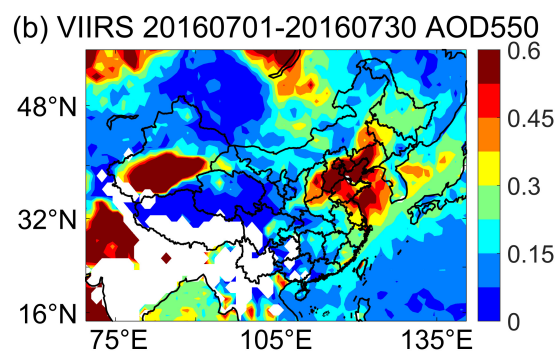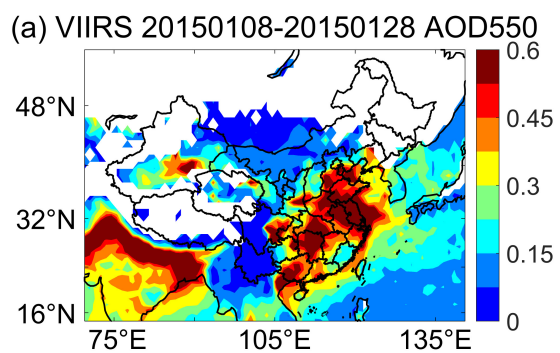
Figure 3. Spatial distributions of the observed and simulated time-averaged AOD at 550 nm (a, c) during January 8 to 28, 2015 and (b, d) during July 1 to 30, 2016. (a, b) VIIRS observations; (c) Case ACRw; (d) Case ACRs
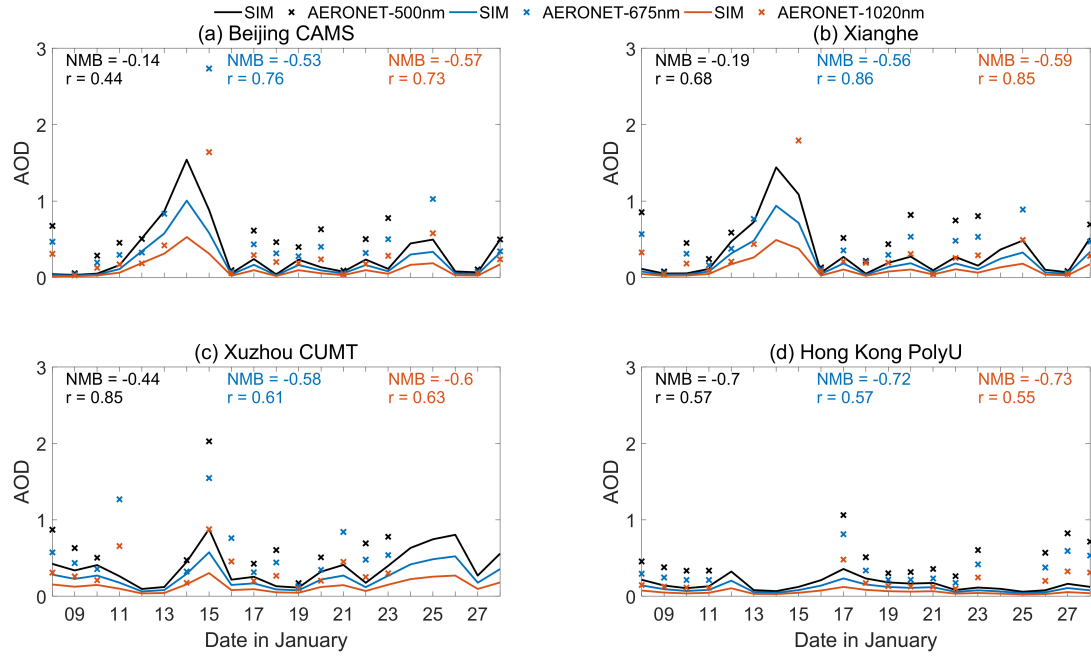
Figure 4. Comparison of simulated daily AOD (Case ACRw) against the AERONET daily AOD observations at 500 nm, 675 nm and 1020 nm at 4 sites during January 08 to January 28, 2015: (a) Beijing, (b) Xianghe, (c) Xuzhou, and (d) Hong Kong. Also shown are the normalized mean biases (NMBs) and the temporal correlation coefficients (r) between the simulated and observed spectral AODs.
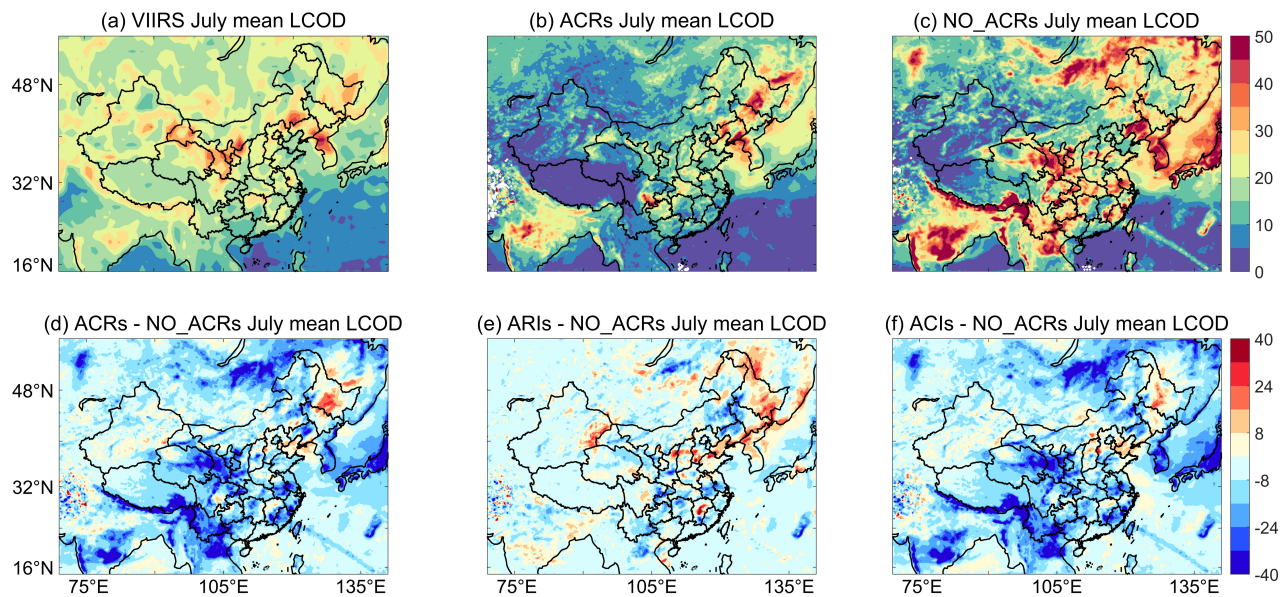
Figure 5. Monthly mean LCOD from (a) VIIRS observations, (b) the Case ACRs simulation, and (c) the Case NO_ACRs simulation during July 2016. Also shown are the differences in simulated LCOD between (d) Case ACRs and Case NO_ACRs, (e) Case ARIs and Case NO_ACRs, and (f) Case ACIs and Case NO_ACRs during July 2016.
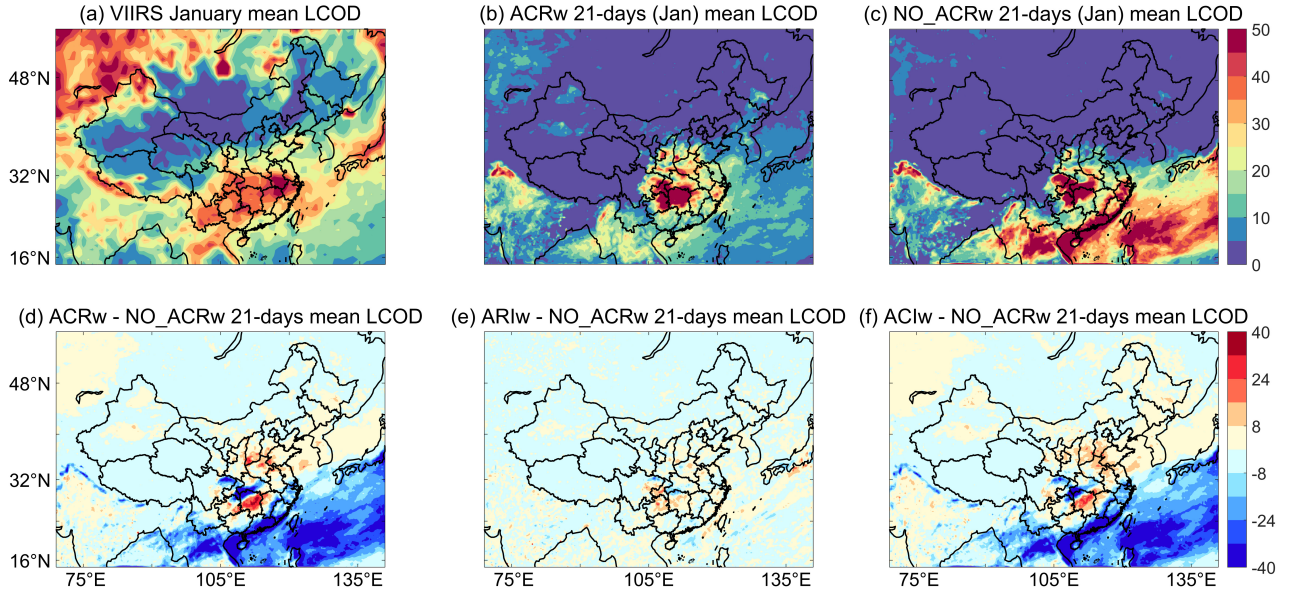
Figure 6. Mean LCOD from (a) VIIRS observations (monthly mean in during January 2015), (b) the Case ACRw simulation, and (c) the Case NO_ACRs simulation during January 8 to 28, 2015. Also shown are the differences in simulated LCOD between (d) Case ACRw and Case NO_ACRw, (e) Case ARIw and Case NO_ACRw, and (f) Case ACIw and Case NO_ACRw during January 8 to 28, 2015.
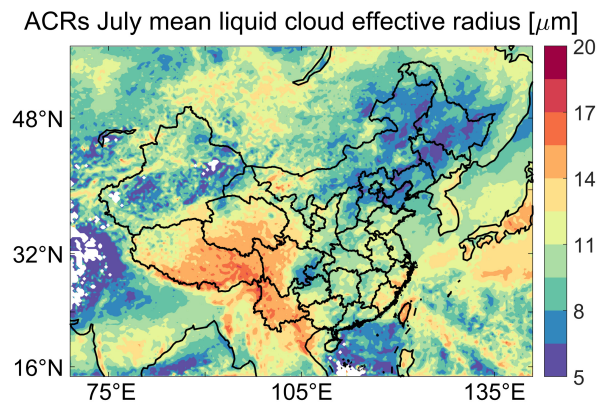

Figure 7. Monthly mean effective radii of liquid cloud droplets from the Case ACR simulation during July, 2016.
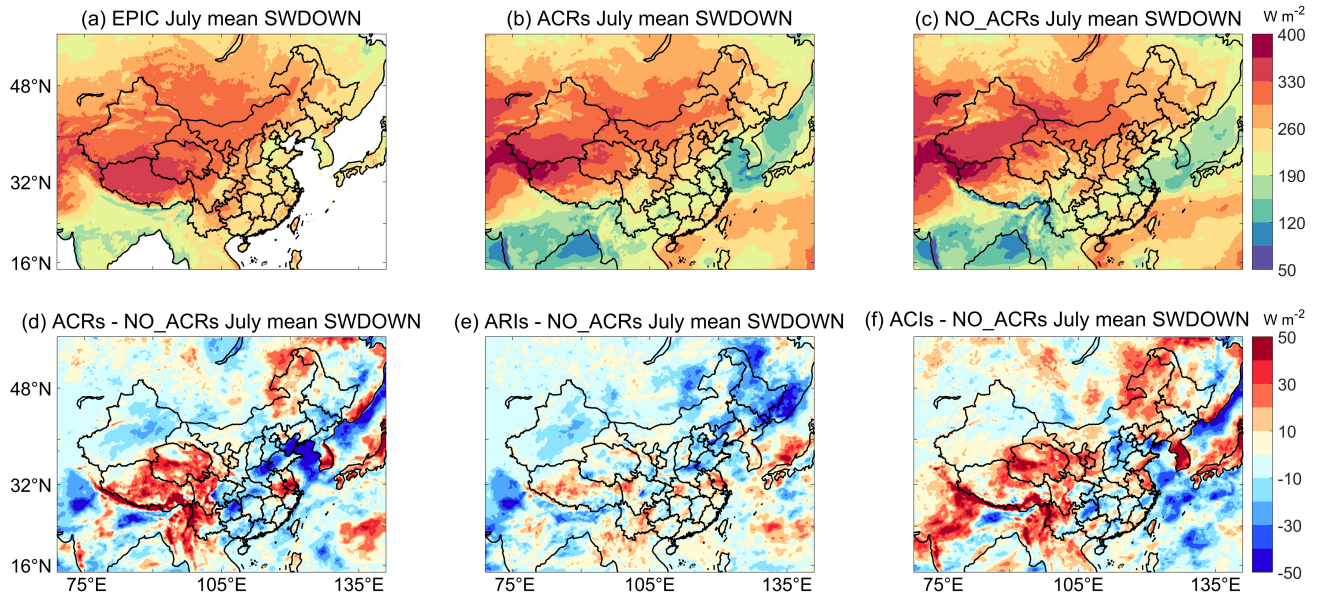
Figure 8. Monthly mean surface downward shortwave radiation (SWDOWN) from (a) EPIC-derived observations, (b) the Case ACRs simulation, and (c) the Case NO_ACRs simulation during July 2016. Also shown are the differences in simulated SWDOWN between (d) Case ACRs and Case NO_ACRs, (e) Case ARIs and Case NO_ACRs, and (f) Case ACIs and Case NO_ACRs during July 2016.
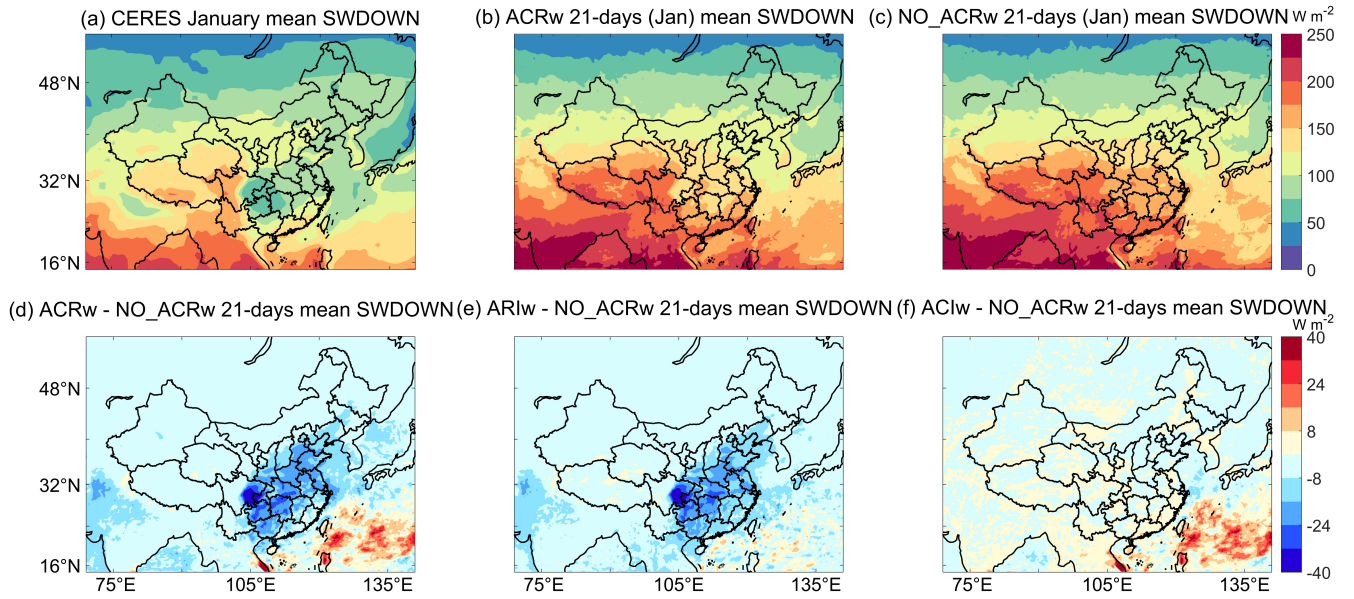
Figure 9. Mean surface downward shortwave radiation (SWDOWN) from (a) CERES observations (monthly mean in January), (b) the Case ACRw simulation, and (c) the Case NO_ACRw simulation during January 8 to 28, 2015. Also shown are the differences in simulated mean SWDOWN between (d) Case ACRw and Case NO_ACRw, (e) Case ARIw and Case NO_ACRw, and (f) Case ACIw and Case NO_ACRw during January 8 to 28, 2015.
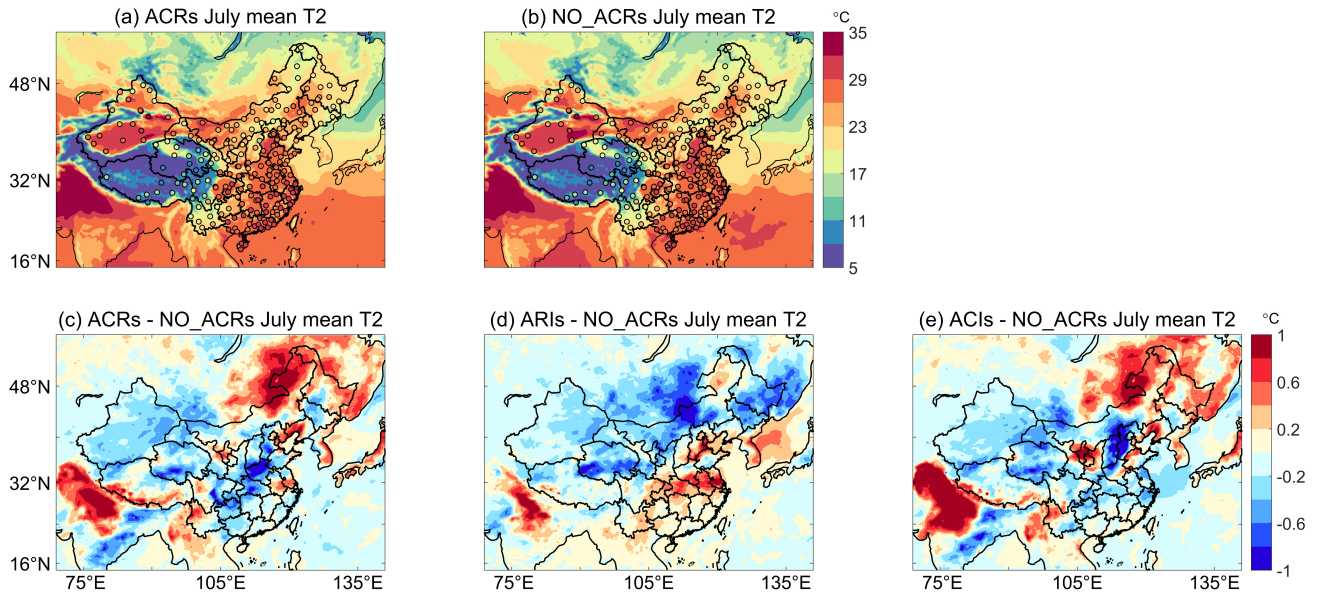
Figure 10. Comparison of the observed (filled symbols) and simulated (filled contours) monthly mean surface air temperature from (a) Case ACRs and (b) Case NO_ACRs during July 2016. Also shown are the differences in simulated monthly mean surface air temperature between (c) Case ACRs and Case NO_ACRs, (d) Case ARIs and Case NO_ACRs, and (e) Case ACIs and Case NO_ACRs during July 2016.

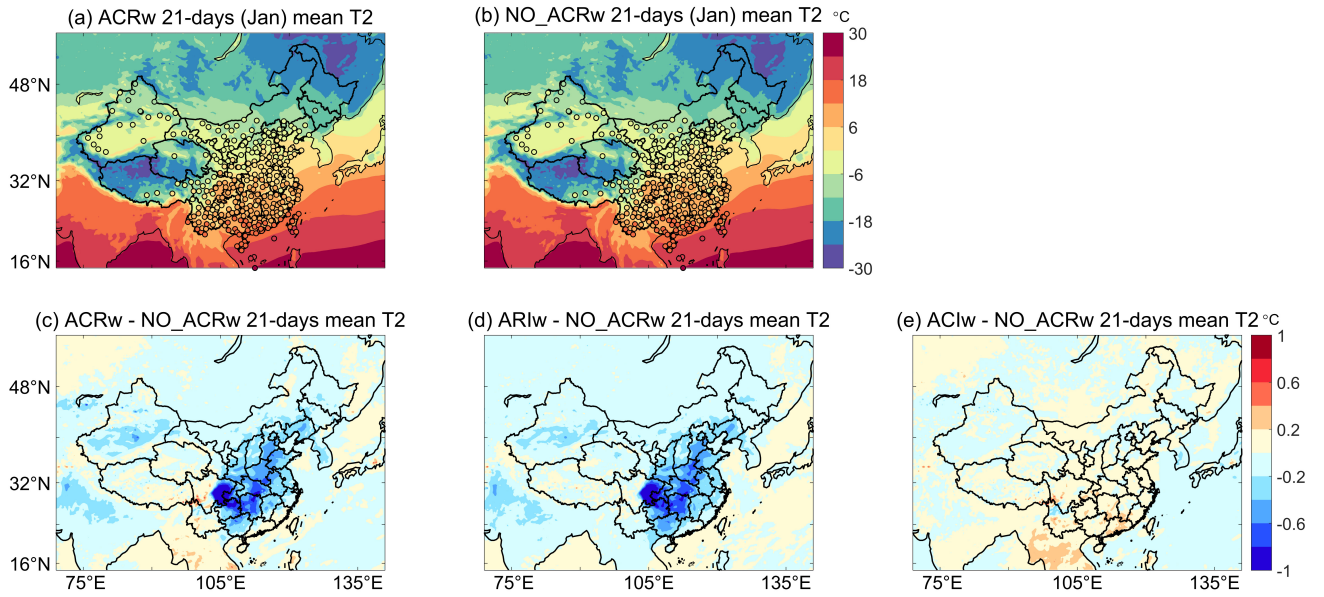**Figure 11.** Comparison of the observed (filled symbols) and simulated (filled contours) mean surface air temperature from (a) Case ACRw and (b) Case NO_ACRw during January 8 to 28, 2015. Also shown are the differences in simulated mean surface air temperature between (c) Case ACRw and Case NO_ACRw, (d) Case ARIw and Case NO_ACRw, and (e) Case ACIw and Case NO_ACRw during January 8 to 28, 2015.

Figure 12. Comparison of the observed (filled symbols) and simulated (filled contours) mean planetary boundary layer heights (PBLH) at 20:00 local time (12:00 UTC) from (a) Case ACRw and (b) Case NO_ACRw during January 8 to 28, 2015. Also shown are the differences in simulated PBLH at 20:00 local time (12:00 UTC) between (c) Case ACRw and Case NO_ACRw, (d) Case ARIw and Case NO_ACRw, and (e) Case ACIw and Case NO_ACRw during January 8 to 28, 2015.

Figure 13. (a) Mean observed (symbols) and simulated (Case ACRw, filled contours) PM$_{2.5}$ concentrations during January 8 to 28, 2015; (b) mean observed (symbols) and simulated (Case ACRs, filled contours) afternoon surface ozone concentrations (13:00 to 17:00 local time) during July 2016.

Figure 14. Differences in simulated monthly mean afternoon (13:00 to 17:00 local sun time) surface ozone concentrations during July 2016 (a) between Case ACRs and Case NO_ACRs, (b) between Case ARIs and Case NO_ACRs, and (c) between Case ACIs and Case NO_ACRs. Differences of simulated mean $PM_{2.5}$ concentrations during January 8 to 28, 2015 (d) between Case ACRw and Case NO_ACRw, (e) between Case ARIw and Case NO_ACRw , and (f) between Case ACIw and Case NO_ACRw. Stippled grids represent significant differences (two-tail t-test at 5% significance level).

Figure 15. Mean simulated chemical mass tendency (unit: $\mathrm{kg\ s^{-1}}$) for afternoon boundary-layer ozone from (a) Case ACRs, (b) Case ARIs, and (c) Case ACIs during July 2016. Also shown are the differences in simulated chemical mass tendencies for afternoon boundary-layer ozone between (d) Case ACRs and Case NO_ACRs, (e) Case ARIs and Case NO_ACRs, and (f) Case ACIs and Case the NO_ACRs in July 2016.

Table 1. Aerosol types in WRF-GC and their prescribed properties and size distributions
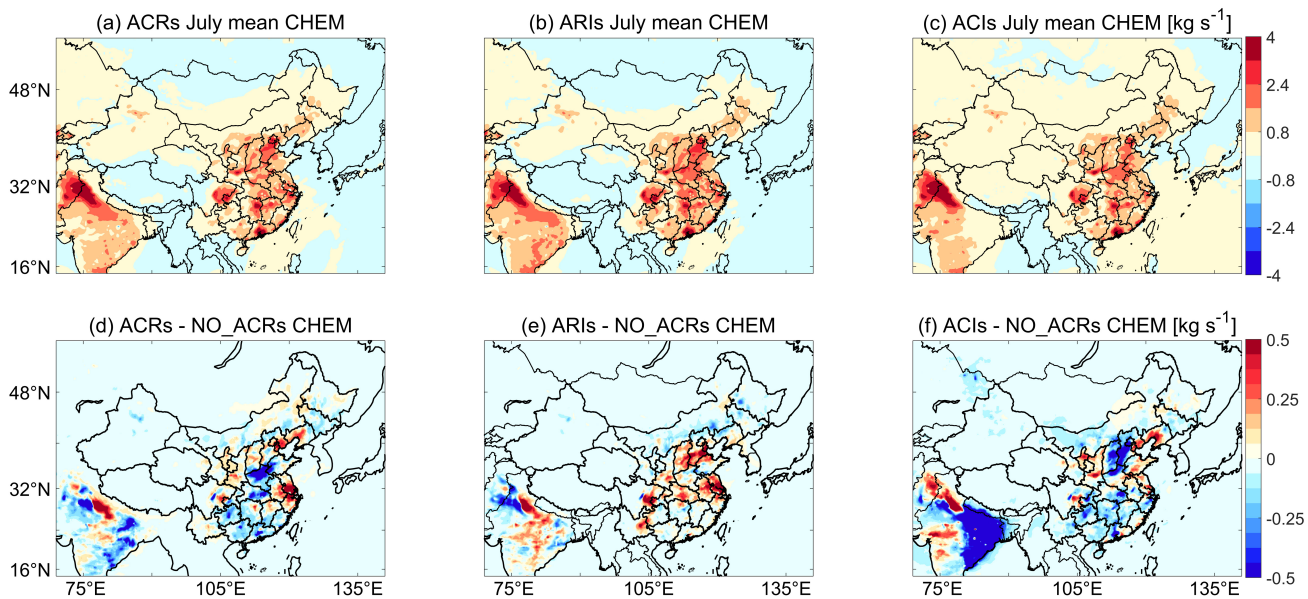
Name	Species	Molecular weight ($g \cdot mol^{-1}$)	Density ($g \cdot cm^{-3}$)	Hygroscopicity (unitless)	Log-normal distribution (Geometric mean dry diameter, µm)	Log-normal distribution (Geometric standard deviation, unitless)
SO4	sulfate	96	1.7	0.5	0.14	1.6
NIT	nitrate	62	1.8	0.5	0.14	1.6
NH4	ammonium	18	1.8	0.5	0.14	1.6
OCPI	hydrophilic primary OC	12	1.3	0.2	0.14	1.6
OCPO	hydrophobic primary OC	12	1.3	0.2	0.14	1.6
BCPI	hydrophilic BC	12	1.8	1.00E-06	0.04	1.6
BCPO	hydrophobic BC	12	1.8	1.00E-06	0.04	1.6
SALA	accumulation-mode sea salt (radius 0.1 - 0.5 µm)	31.4	2.2	1.16	0.18	1.5
SALC	coarse-mode sea salt (radius 0.5 - 4.0 µm)	31.4	2.2	1.16	0.8	1.8
DST1	dust bin 1 (radius 0.1 - 1.0 µm)	29	2.5	0.14	–	–
DST2	dust bin 2 (radius 1.0 - 1.8 µm)	29	2.65	0.14	–	–
DST3	dust bin 3 (radius 1.8 - 3.0 µm)	29	2.65	0.14	–	–
DST4	dust bin 4 (radius 3.0 - 6.0 µm)	29	2.65	0.14	–	–
SOAS	SOA (simple)	150	1.5	0.14	0.14	1.6

Table 2. Upper and lower bounds of particle dry diameter for the 4 aerosol size bins used by WRF-GC

Bin	Lower bound (μm)	Upper bound (μm)
1	0.0390625	0.15625
2	0.15625	0.625
3	0.625	2.5
4	2.5	10.0

Table 3. Wall times of simulations conducted with the WRF-GC v2.0 model and the GEOS-Chem Classic nested-grid model (unit: s).

Model	**WRF-GC v2.0**				**GEOS-Chem Classic nested grid**
Experiment	One-way	ARI only	ACI only	ARI and ACI	v12.7.2
Total wall time	15378	17002	15283	16153	33601
Breakdown: WRF	7766	8374	7274	7511	-
Breakdown: GEOS-Chem	7242	7242	7591	7206	-
Breakdown: WRF-GC Coupler	370	1391	417	1436	-

Table 4. Configurations of WRF-GC v2.0 experiments in this study

Experiment	Case ACRs	Case ARIs	Case ACIs	Case NO_ACRs
Simulation time	2016-06-27 00Z to 2016-07-31 00Z			
Microphysics	Morrison two-moment (Morrison et al., 2009)			
Shortwave radiation	RRTMG (Iacono et al., 2008)			
Longwave radiation	RRTMG (Iacono et al., 2008)			
Planetary boundary Layer	MYNN2 (Nakanishi and Niino, 2006)			
Land surface	Noah (Chen and Dudhia, 2001a, b)			
Surface layer	MM5 Monin-Obukhov (Jimenez et al., 2012)			
Cumulus parameterization	New Tiedtke (Tiedtke, 1989; Zhang et al., 2011a; Zhang and Wang, 2017)			
Aerosol-radiation interaction	On	On	Off	Off
Aerosol-cloud interaction	On	Off	On	Off
Experiment	Case ACRw	Case ARIw	Case ACIw	Case NO_ACRw
Simulation time	2015-01-04 00Z to 2015-01-29 00Z			
Microphysics	Morrison two-moment (Morrison et al., 2009)			
Shortwave radiation	RRTMG (Iacono et al., 2008)			
Longwave radiation	RRTMG (Iacono et al., 2008)			
Planetary boundary Layer	YSU (Hong et al., 2006)			
Land surface	Noah (Chen and Dudhia, 2001a, b)			
Surface layer	MM5 Monin-Obukhov (Jimenez et al., 2012)			
Cumulus parameterization	New Tiedtke (Tiedtke, 1989; Zhang et al., 2011a; Zhang and Wang, 2017)			
Aerosol-radiation interaction	On	On	Off	Off
Aerosol-cloud interaction	On	Off	On	Off

Table 5. Comparison of the simulated liquid cloud optical depth (LCOD), surface downward shortwave radiation (SWDOWN), and surface temperature (T2) from sensitivity experiments against satellite and surface observations during July 2016 and January 2015

	Case ACRs	Case ARIs	Case ACIs	Case NO_ACRs	Case ACRw	Case ARIw	Case ACIw	Case NO_ACRw
LCOD over Eastern China (eastward of 100 °E) against VIIRS observations								
Mean ± stdev	13.0 ± 8.6	22.1 ± 13.0	12.5 ± 8.1	21.8 ± 12.4	9.8 ± 10.4	17.3 ± 18.7	9.6 ± 10.4	17.1 ± 18.6
R	0.64	0.65	0.60	0.62	0.48	0.34	0.46	0.33
RMSE	8.4	10.9	8.7	10.7	15.2	18.4	15.4	18.5
SWDOWN [W m^{-2}] over China against EPIC-derived observations (July) and CERES observations (January)								
Mean ± stdev	281 ± 48	274 ± 49	287 ± 49	278 ± 51	140 ± 55	139 ± 55	144 ± 57	143 ± 56
R	0.73	0.65	0.65	0.57	0.93	0.92	0.91	0.9
RMSE	33.7	40.4	37.5	43.5	36.3	35.4	41.2	40.4
T2 [°C] over China against surface measurements (215 sites in July, 150 sites in January)								
Mean ± stdev	23.7 ± 5.9	23.7 ± 6.1	23.8 ± 6.0	23.8 ± 6.0	7.2 ± 6.7	7.1 ± 6.7	7.4 ± 6.7	7.3 ± 6.6
R	0.92	0.93	0.92	0.92	0.93	0.93	0.93	0.93
RMSE	2.52	2.57	2.56	2.57	2.7	2.8	2.6	2.7

Table 6. Comparison between the PM$_{2.5}$ and afternoon ozone concentrations simulated by sensitivity experiments against the surface observations during July 2016 and January 2015

PM$_{2.5}$: 388 sites over Eastern China [μg m^{-2}]			
	Mean ± stdev	R	Slope
Case ACRw	80.8 ± 32.6	0.77	0.97
Case ARIw	81.6 ± 32.6	0.77	0.97
Case ACIw	77.9 ± 30.4	0.78	0.9
Case NO_ACRw	78.8 ± 30.4	0.78	0.9
Afternoon ozone: 426 sites over Eastern China [ppbv]			
	Mean ± stdev	R	Slope
Case ACRs	64.2 ± 16.9	0.56	1.33
Case ARIs	64.7 ± 17.1	0.57	1.34
Case ACIs	65.0 ± 17.6	0.54	1.38
Case NO_ACRs	63.6 ± 17.6	0.52	1.38